Controlling Electromagnetic Fields with Tensor Transmission-Line Metamaterials

by

Gurkan Gok

A dissertation submitted in partial fulfillment
of the requirements for the degree of
Doctor of Philosophy
(Electrical Engineering)
in The University of Michigan
2014

Doctoral Committee:

Associate Professor Anthony Grbic, Chair
Assistant Professor Julie S. Biteen
Professor Eric Michielssen
Professor Kamal Sarabandi

To my family

ACKNOWLEDGEMENTS

I would like to gratefully and sincerely thank my advisor, Professor Anthony Grbic, for his continuous encouragement, friendship and invaluable guidance during my studies. His passion and profound knowledge has always been a source of inspiration during my work that forms this thesis.

I extend my gratitude to my thesis committee, Professor Eric Michielssen, Professor Kamal Sarabandi, and Professor Julie Biteen, for serving on my committee, and providing valuable suggestions towards the completion of this work

I would like to thank Professor H. Özlem Çivi and Professor A. Aydın Alatan for their mentorship and support during my undergraduate years at Middle East Technical University. Their inspiration and encouragement helped me to start my research work early in undergraduate years, and pursue a graduate degree.

I also thank all my current and former research group members. I extend my gratitude to my colleagues, staff members at Radiation Laboratory, and friends in Ann Arbor. I appreciate their camaraderie and support all these years.

Finally, and most importantly, I would like to give my greatest gratitude to my family: my parents Nilgün and Mehmet Gök, my sister Gülçin Gök, and my wife Işıl Gök. Without their endless love and support, I would not be at the point where I am today. I would like to thank my wife Işıl for her encouragement, quiet patience and unwavering love. Her presence and support made this moment possible.

TABLE OF CONTENTS

LIST OF FIGURES

Figure

LIST OF TABLES

Table

LIST OF APPENDICES

Appendix

ABSTRACT

Controlling Electromagnetic Fields with Tensor Transmission-Line Metamaterials

by

Gurkan Gok

Chair: Anthony Grbic

The advent of metamaterials and transformation electromagnetics have revolutionized the use of materials in the control of electromagnetic fields. Metamaterials enabled the control of material properties, and transformation electromagnetics provided a systematic procedure for designing these materials to achieve a specified electromagnetic field distribution. Greater control over the material parameters amounts to greater control over electromagnetic fields. In particular, the ability to design anisotropic materials with spatially varying material parameters is crucial to the development of countless novel guided-wave and radiating structures.

This thesis shows how to develop electromagnetically anisotropic, inhomogeneous materials using circuit networks: tensor transmission-line metamaterials. Tensor transmission line metamaterials are circuit-based metamaterials possessing tensorial effective material parameters. They are magnetically anisotropic, and their anisotropic material parameters consist of a 2×2 permeability tensor and scalar permittivity. A theoretical basis for analyzing, synthesizing and homogenizing tensor transmission-line metamaterials is developed. Their propagation characteristics are

verified through full-wave simulation and experiment.

In addition, a distinct method for arbitrarily controlling the phase progression and power flow of electromagnetic fields within a region of space is proposed. The method provides an alternative design approach to transformation electromagnetics, and it exploits an anisotropic medium's ability to support power flow and phase progression in different directions. The proposed method has proven useful in establishing aperture field profiles with arbitrary phase and amplitude distributions. Illustrative examples are introduced. Beam-formers, which can create arbitrary aperture field distributions (phase and amplitude) are reported.

CHAPTER I

Introduction

1.1 Background

Vacuum is the most elementary medium in electromagnetics. From a classical perspective, it represents a space deprived of materials. In such a medium, electromagnetic waves can exist as first postulated by James Clerk Maxwell [1]. In other words, electromagnetics waves do not require a material to propagate within. The presence of a material and its interaction with electromagnetic waves, however, can be used to harness electromagnetic fields. This fact has been exploited for centuries to design optical lenses by appropriately crafting glasses to collimate or divert optical waves. Such a basic interaction between electromagnetic waves and material has been a source of technological advancements such as microscopes and cameras. This has intrigued scientists and engineers over the years and enticed them to study the interaction between materials and electromagnetic waves: analyzing different phenomena and finding ways to tailor waves for desired purposes.

The interaction between materials and electromagnetic waves originates from the atomic/molecular structure of materials. According to the Bohr atomic model, atoms consist of charged and neutral particles, where a negatively charged electron cloud surrounds a positively charged nucleus, and can exhibit spin and rotational motion. Maxwell's equations dictate that an applied electromagnetic field exerts forces on

these charged particles, subsequently effecting their position and motion. This interaction results in the polarization and magnetization of the atoms/molecules. Upon interaction, the polarized and magnetized atoms/molecules also become sources of electromagnetic fields. It is the combined electromagnetic field that results in observed phenomena such as the collimated or diverted fields emitted from a glass lens. Given that a material consists of a multitude of atoms/molecules, the overall response of the material to electromagnetic fields can be accounted for material parameters, known as permittivity (ϵ) and permeability (μ), as long as the wavelength of operation is much larger than the atomic or molecular scales. For such scales, the material definitions are more tractable and useful than considering assemblies of atoms and molecules. The permittivity and permeability define the electromagnetic response of material to electric and magnetic fields, respectively.

If it were possible to arrange atoms and molecules individually, precise control over the permittivity and permeability could be achieved. This sounds like a daunting task, yet earlier antenna engineers were able to engineer material parameters [2, 3]. Inserting small (compared to wavelength of interest) inclusions into a host medium, the overall response of the composite medium could be tailored. Such an approach was used to design composite materials consisting of shaped metallic inclusions such as spheres [2] and wires [3] to engineer the material parameters of the host medium. By varying the permittivity values, this approach was used to design lenses for antenna applications. The lenses collimated waves much like homogeneous glass lenses, but at much lower frequencies.

In the early 2000s, interest in designing materials with various permittivity and permeability values, including those not readily available in nature, reignited. Separate demonstrations of negative permittivity [4] and negative permeability [5] media using appropriately shaped subwavelength metallic inclusions paved the way to designing a negative index medium [6] possessing simultaneously negative permit-

tivity and permeability values. Demonstration of counter-intuitive electromagnetic phenomena such as negative refraction [7], subwavelength resolution [8, 9], reversed Cherenkov radiation [10, 11] followed. In 2001, the first negative refractive index medium was implemented and tested at microwave frequencies [7]. This groundbreaking work, along with introduction of the "perfect lens" [12], initiated great interest in subwavelength-structured composite materials possessing tailored electromagnetic properties, known today simply as "metamaterials". Metamaterials are defined as artificial, subwavelength-structured materials designed to have tailored electromagnetic properties. In these structures, subwavelength inclusions arranged with subwavelength spacings play the role of atoms/molecules in a conventional material. The overall properties of the metamaterial are determined by the structure and arrangement of the inclusions. Carefully engineered metamaterials are able to establish prescribed electric and magnetic properties defined by its effective permittivity and permeability. Initial metamaterials were designed using metallic shapes such as wires [4] and split ring resonators [5] for electric and magnetic responses, respectively. A transmission-line approach to metamaterial synthesis [13, 14, 15, 16] soon followed the initial volumetric negative index metamaterial consisting of wires and split-ring resonators. In the transmission-line approach, a host transmission-line is periodically loaded with reactive elements. Two dimensional isotropic and anisotropic transmission-line metamaterials were introduced exhibiting both negative and positive effective material parameters [17, 18, 19, 20, 21, 22, 23, 24].

Metamaterials have been utilized in a wide range of applications since their invention. Super-lenses [8, 9], antennas [10, 25, 26], novel microwave circuits [27], absorbers [28, 29] are only a few examples. Although the first metamaterial design and applications started at microwave frequencies, interest in these artificial materials has spread to all frequency range from DC to optical frequencies. The advent of the nanofabrication techniques and a deeper theoretical understanding has allowed this proliferation.

More recently, the 2D equivalent of metamaterials, known as metasurfaces, has gained significant attention. Metasurfaces have enabled the control of electromagnetic fields across very thin surfaces, and expanded the use of metamaterials [30, 31, 32]. Apart from the electromagnetic regime, metamaterials have also found application in the control of acoustic, thermal, and seismic wave phenomena [33, 34, 35].

1.2 Motivation

Control over material parameters has brought with it enhanced control over the electromagnetic fields. Specifically, control over anisotropy and inhomogeneity has opened an enormous design space. In 2006, Pendry, Schurig and Smith proposed a radically new electromagnetic design approach that takes advantage of the ability to synthesize arbitrary material parameters using metamaterials [36]. This seminal work outlined how a coordinate transformation could be used to control electromagnetic waves and establish desired field distributions within a region of space. In this method, referred to as transformation optics/electromagnetics, the change from an initial electromagnetic field distribution (illumination) to a desired one is expressed as a coordinate transformation. Then, the form invariance of Maxwell's equations under coordinate transformations is exploited to calculate the transformed medium parameters that support the desired field distribution. The medium with transformed medium parameters is inherently reflectionless and precisely establishes the desired field transformation. This method was used to demonstrate a device which has been the subject of numerous science-fiction novels: an invisibility cloak [37]. In the proposed cloak, a medium made of spatially-varying, anisotropic material parameters is designed with metamaterials. It guides electromagnetic waves around a hidden object, preventing scattering from the object and rendering it invisible.

Subsequently, numerous other devices such as field concentrators [38], collimators [39, 40], rotators [41], polarizers [42], bent waveguides [43, 44], antennas [45, 46, 47],

lenses [48] and optical illusion devices [49] have been proposed using the transformation optics method [50, 51, 52, 53, 54, 55]. They have all demonstrated unprecedented control over electromagnetic fields using spatially varying material parameters within a region of space. Unfortunately, the implementation of these structures has not kept pace with the theoretical proposals. The reason is that electromagnetic devices designed using transformational electromagnetics often consist of material parameters (permittivity and permeability) with full tensors that spatially vary in space. To ease the physical realization of transformation electromagnetics devices, methods of simplifying material parameters have been proposed [37, 56, 57]. Transformation electromagnetic devices with reduced and diagonal material parameters which only preserve the index variation has been demonstrated [37]. On the other hand, conformal and quasi-conformal coordinate transformations [56, 57] leading to reduced/eliminated anisotropy and less spatial variation of the material parameters have been utilized. However, material simplification procedures have been applied to transformation electromagnetics devices whose operation only depends on the field distribution at the periphery of the device, such as cloaks and lenses. In order to obtain a full control over the electromagnetic fields, the fields are required to be controlled within the device as well as at its periphery. In its most general form, this requires the synthesize of the full material parameter tensors.

A need for control over the full material parameter tensors to implement transformation electromagnetics devices arose. Transmission-line based metamaterials are favorable type of metamaterials for this need, because they typically exhibit a lower loss and wider bandwidths of operation than resonant metamaterials structures [17, 27]. Furthermore, transmission-line based metamaterials can be tailored for both planar and volumetric applications. However, earlier transmission-line metamaterials were limited to having diagonal tensors in the Cartesian basis, whereas the transformation electromagnetics often requires materials with full tensor. Creating arbitrary material

parameters was needed to implement various transformation electromagnetics devices using transmission-line based metamaterials.

The objective of this work is to propose transmission-line metamaterials with arbitrary full material tensors, and show their utility in the design of transformation electromagnetic devices. Furthermore, this thesis presents a distinct method for designing reflectionless, inhomogeneous, anisotropic media that can support prescribed spatial distributions of phase progression and power flow direction. The proposed method provides an intuitive approach to electromagnetic field control using anisotropic inhomogeneous medium, and can be utilized as an alternative design approach to transformation electromagnetics. Finally, the tensor transmission-line metamaterials and the proposed method are combined to control electromagnetic waves, and design novel electromagnetic devices.

1.3 Outline

This thesis presents tensor transmission-line metamaterials and their use in the control of electromagnetics waves. Tensor transmission-line metamaterials are circuit-based metamaterials which possess tensorial effective material parameters. This work details the theory behind the proposed metamaterials and outlines a general method for controlling electromagnetic waves.

The thesis is organized into six chapters. In Chapter 2, the idea of synthesizing anisotropic media with transmission-line based metamaterials is introduced. The proposed structures are referred to as tensor transmission-line metamaterials [58]. They are 2D electrical circuit networks that behave as magnetically anisotropic media. The propagation characteristics of a generalized 2D periodic tensor transmission-line network is investigated. The anisotropic properties of the metamaterial are verified through full-wave simulations [59]. Transformation electromagnetic devices simulated using tensor transmission-line metamaterials are presented. Chapter 3 presents

a homogenization method to compute the effective material parameters of tensor transmission-line metamaterials [60]. The homogenization method, which employs a local field averaging procedure, is described in detail. Both metamaterials with dispersive and non-dispersive effective material parameters are considered. Simulation results are provided to verify the proposed homogenization method. Chapter 4 experimentally verifies the theory presented in earlier chapters, and demonstrates the utility of tensor transmission-line metamaterials in the design of transformation electromagnetics devices. The design and implementation of a transformation electromagnetics device, a beam shifting-slab, using tensor transmission-line metamaterials is presented [61]. The design procedure as well as simulated and measured results are reported. In Chapter 5, an approach to arbitrarily controlling the phase progression and power flow of electromagnetic fields within a 2D region of space is proposed [62]. Specifically, the design of a 2D inhomogeneous, anisotropic media that support prescribed distributions of wave vector and Poynting vector directions is outlined. Specific examples are reported which show how the proposed method can be used to tailor the field radiated by a cylindrical source into desired amplitude and phase profiles. Moreover, the relationship between the proposed method and transformation electromagnetics is drawn. The proposed method is used to find alternative material parameters for 2D transformation electromagnetics devices. The alternative material parameters support exactly the same field pattern as the original ones of the transformation electromagnetics device for a give illumination. The method is further extended to design dual functional transformation electromagnetics devices that combine the characteristics of two separate transformation devices under different illuminations into one [63]. Finally, Chapter 6 summarizes the research findings and outlines the contributions of this work. It also suggests future directions.

CHAPTER II

Tensor Transmission-Line Metamaterials

In this chapter, the idea of synthesizing anisotropic media with transmission-line based metamaterials is introduced. The proposed structures are referred to as tensor transmission-line metamaterials. They are 2D electrical circuit networks that behave as magnetically anisotropic media represented by a 2×2 permeability tensor and permittivity scalar. These metamaterials are crucial to the development of numerous transformation electromagnetic devices, which often consists of materials with full tensors that vary arbitrarily in space. Using a novel circuit approach, it is shown that the material parameter distributions of transformation-designed electromagnetic devices can be directly mapped to two-dimensional transmission-line networks. In essence, the work draws a link between microwave network theory (circuits) and transformation electromagnetics. As a result, tensor transmission-line metamaterials can also be referred to as "transformation circuits" [64].

The chapter starts with a brief review of earlier transmission-line based metamaterials. Then, an approximate tensor analysis to analyze transmission-line metamaterials is developed. This analysis will provide key insight into the development of tensor transmission-line metamaterials. The proposed analysis is first applied to earlier transmission-line structures, and then used to analyze tensor transmission-line topologies. A rigorous Bloch analysis is then performed to verify approximate

tensor analysis. Exact dispersion equations for tensor transmission-line metamaterials are derived using Bloch analysis, and the impedances needed to terminate Bloch waves in finite structures are found. Subsequently, the use of tensor transmission-line metamaterials is investigated. A reflectionless interface and two transformation electromagnetic devices (an electromagnetic cloak and electromagnetic field rotator) are designed using circuit networks of tensor transmission-line metamaterials. Their simulated performances are presented. In order to realize the proposed metamaterials at microwave frequencies, a microstrip implementation is proposed. Towards the end of the chapter, the anisotropic properties of the implemented tensor transmission-line metamaterials are verified through full-wave simulation. The full-wave simulations are used to compute the dispersion curves of the realized metamaterials. The computed dispersion curves are compared to those predicted analytically. Circuit and full-wave simulations presented in this chapter validate the analysis of tensor transmission-line metamaterials and show the ability of the tensor transmission-line metamaterials to manipulate electromagnetic waves in extreme and unprecedented ways.

2.1 Transmission-line Metamaterials

The transmission-line approach to metamaterial synthesis was extensively studied in the early 2000s [13, 14, 15, 16, 17]. In this approach, a host transmission-line is periodically loaded with reactive elements. The effective material parameters of the synthesized medium are derived using the analogy between TEM wave propagation on transmission-lines and plane-wave propagation in a homogeneous isotropic medium. Fig. 2.1(a) shows the lumped element equivalent of a 1D transmission line of length d. In this configuration, L_o and C_o represent the per unit length inductance and capacitance of the transmission-line segment, respectively. Fig. 2.1(b) depicts plane wave propagation, with vertical electric field polarization, in an isotropic, homogeneous medium with permittivity (ϵ) and permeability (μ). The differential equations

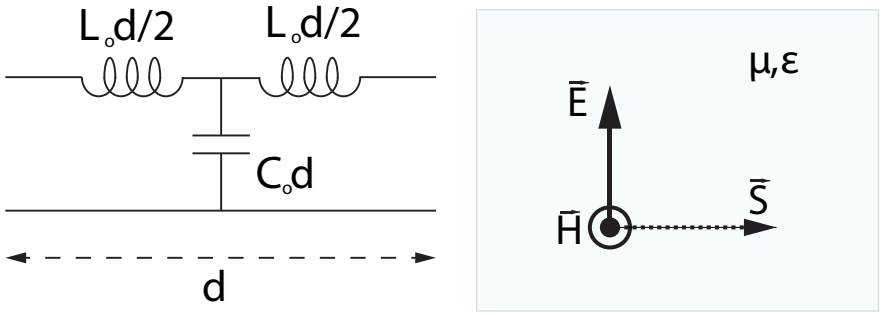

(a) (b)

Figure 2.1: (a) Lumped element equivalent of a 1D transmission line unit cell. (b) Plane wave propagation in an isotropic, homogeneous medium.

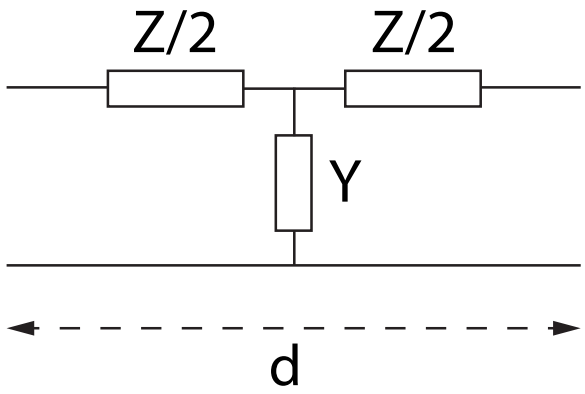

Figure 2.2: Lumped element equivalent of a 1D transmission-line unit cell in general form.

governing wave propagation in the transmission line medium (Telegrapher's equations) and in an isotropic, homogeneous medium (Maxwell's equations) reveal the relationship between the circuit components and the medium parameters. The per-unit length inductance L_o and capacitance C_o of the transmission line in Fig. 2.1(a) is found to be equivalent to the permeability (μ) and permittivity (ϵ) of the homogeneous medium supporting plane-wave propagation, respectively.

A more general representation of the transmission-line model in Fig. 2.1(a) can be obtained if the series inductance and shunt capacitance are replaced with a series impedance Z and a shunt admittance Y. Using this general form, a relationship between the circuit components and material parameters can be written as follows

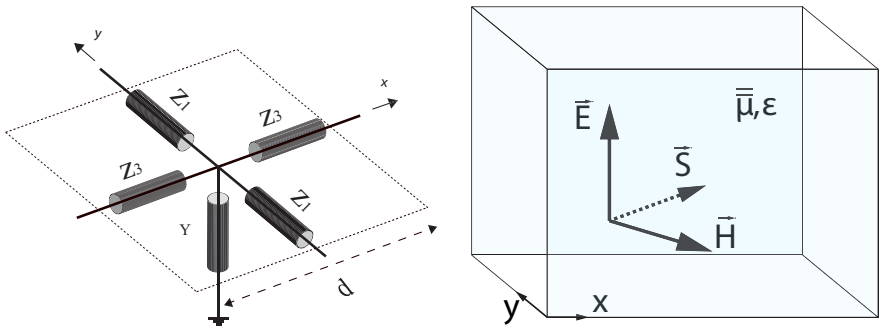

(a) (b)

Figure 2.3: (a) Lumped element equivalent of a 2D transmission-line unit cell. (b) Wave propagation with vertical electric field polarization in an anisotropic homogeneous medium.

[17, 27]:

$$j\omega\mu(\omega)d = Z, \qquad j\omega\epsilon(\omega)d = Y. \tag{2.1}$$

Equation (2.1) provides additional insight into synthesizing material parameters by selecting various combination of Z and Y. Well-known dual transmission-line or composite right/left-handed (CRLH) topologies are obtained when Z and Y are chosen to be negative reactance and negative susceptance, respectively [27, 65, 66].

A similar approach can be applied to the design of 2D transmission-line based metamaterials. The circuit topology used in 2D is shown in Fig. 2.3(a). The analogous wave propagation in a homogenous medium is shown in Fig. 2.3(b). The series impedances of the circuit relate to the permeability tensor ($\bar{\bar{\mu}}$), and the shunt admittance relates to the permittivity (ϵ_z) of the homogeneous medium. Two dimensional isotropic and anisotropic transmission-line metamaterials have been reported in the past that both negative and positive effective material parameters [17, 18, 19, 20, 21, 22, 23, 24]. These transmission-line metamaterials, however, were limited to having diagonal tensors in the Cartesian basis. A transmission-line metamaterial with a full permeability tensor and a scalar permittivity value can be obtained using a more general unit cell that will be introduced in the next sections.

2.2 The Z Tensor Approach to Transmission-line Metamaterial Analysis

In this section, an approximate tensor analysis is developed to analyze transmission-line based metamaterials. The analysis provides a key insight into the development of tensor transmission-line metamaterials. Using the tensor analysis, it is shown how the transmission-line metamaterials reported earlier can be represented by diagonal tensors. Then, new transmission-line metamaterial topologies that can realize full 2×2 material tensors are presented. Metamaterials based on the shunt node transmission-line geometry [67] for S-polarization are considered throughout the chapter. The results can be easily extended to the series node configuration [67] for P-polarization.

A transmission-line metamaterial with two series branches along x and y direction is shown in Fig. 2.4. This configuration will be referred to as 2-branch structure. This 2-branch structure is in general anisotropic since Z_1 and Z_3 may be different. Two different choices of unit cell for this metamaterial are shown in Fig. 2.5. Let us consider the square unit cell of Fig. 2.5(b). Through the proposed analysis, it will be shown that this unit can be represented by an impedance tensor $\bar{\bar{Z}}$ and a scalar admittance Y. The impedance tensor represents the series branches of the network, and the shunt admittance represents the shunt branch of the network. The impedance tensor can be found by removing the shunt admittance Y and applying voltages ΔV_x and ΔV_y across the unit cell, and then solving for the net currents, I_x and I_y, in the x and y directions, as shown in Fig. 2.6. Following this procedure, the following set of equations can be written for the net currents,

$$\begin{aligned} I_x &= I_3 a + I_3 b = \frac{\Delta V_x}{2Z_3}, \\ I_y &= I_1 a + I_1 b = \frac{\Delta V_y}{2Z_1}. \end{aligned} \tag{2.2}$$

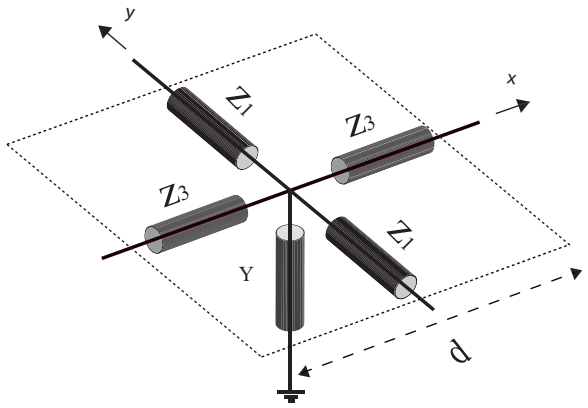

Figure 2.4: Perspective view of the 2-branch transmission-line metamaterial unit cell.

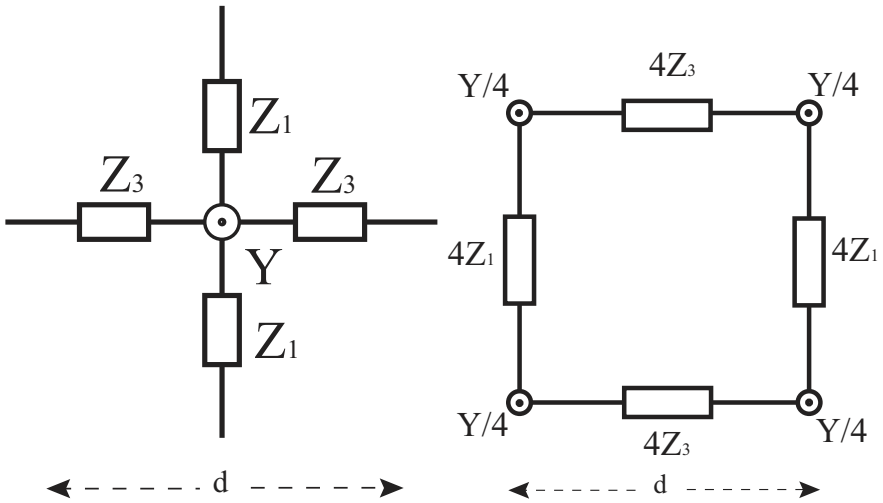

(a) Cross unit cell of the 2-branch transmission-line metamaterial.

(b) Square unit cell of the 2-branch transmission-line metamaterial.

Figure 2.5: Top views of two different unit cell choices for the 2-branch transmission-line metamaterial shown in Fig. 2.4.

These equations can be recast in terms of an admittance tensor $\bar{\bar{Y}}$,

$$\overline{I} = \bar{\bar{Y}}\overline{V} = \begin{bmatrix} y_{xx} & y_{xy} \\ y_{yx} & y_{yy} \end{bmatrix} \begin{bmatrix} \Delta V_x \\ \Delta V_y \end{bmatrix} = \begin{bmatrix} \frac{1}{2Z_3} & 0 \\ 0 & \frac{1}{2Z_1} \end{bmatrix} \begin{bmatrix} \Delta V_x \\ \Delta V_y \end{bmatrix}. \tag{2.3}$$

By taking the inverse of $\bar{\bar{Y}}$, the matrix equation can be expressed in terms of an impedance tensor $\bar{\bar{Z}}$ representing the series branches of the unit cell depicted in Fig.

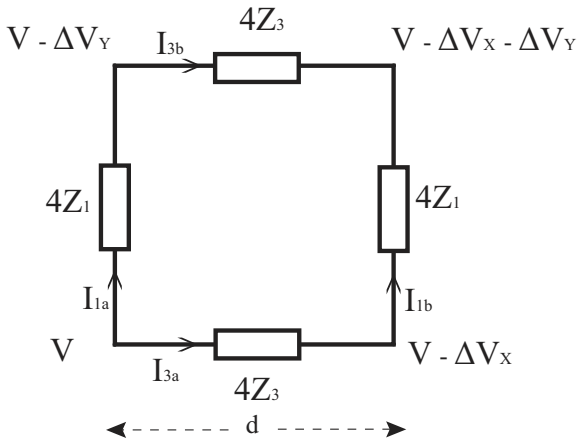

Figure 2.6: The configuration used to extract the impedance tensor of the 2-branch transmission-line metamaterial unit cell.

2.5(b),

$$\bar{V} = \bar{\bar{Z}}\bar{I} = \begin{bmatrix} z_{xx} & z_{xy} \\ z_{yx} & z_{yy} \end{bmatrix} \begin{bmatrix} I_x \\ I_y \end{bmatrix} = \begin{bmatrix} 2Z_3 & 0 \\ 0 & 2Z_1 \end{bmatrix} \begin{bmatrix} I_x \\ I_y \end{bmatrix}. \tag{2.4}$$

The tensor $\bar{\bar{Z}}$ and shunt admittance Y completely characterize the propagation characteristics along the transmission-line metamaterial when the phase delay/advance across the unit cell is small: $k_x d \ll 1$, $k_y d \ll 1$. Here, k_x and k_y are the wavenumbers in the x and y directions, and d is the metamaterial's unit cell dimension. By deriving the two dimensional Telegrapher's equations and corresponding wave equations, the dispersion relation of the transmission-line metamaterial shown in Fig. 2.4 can be found [18, 68],

$$\frac{(k_x d)^2}{-2Z_3 Y} + \frac{(k_y d)^2}{-2Z_1 Y} = 1. \tag{2.5}$$

It can be reexpressed in terms of the $\bar{\bar{Z}}$ tensor entries defined in (2.4),

$$\frac{(k_x d)^2}{-z_{xx} Y} + \frac{(k_y d)^2}{-z_{yy} Y} = 1. \tag{2.6}$$

The propagation characteristics of this network are analogous to those for an S-polarized wave (electric field polarized in the z direction) in a medium with the permeability tensor

$$\bar{\bar{\mu}} = \begin{bmatrix} \mu_{xx} & 0 \\ 0 & \mu_{yy} \end{bmatrix} \tag{2.7}$$

and permittivity ϵ_z in the z direction. Such a medium yields the following dispersion equation,

$$\frac{(k_x)^2}{\omega^2 \mu_{yy} \epsilon_z} + \frac{(k_y)^2}{\omega^2 \mu_{xx} \epsilon_z} = 1, \tag{2.8}$$

which can be written as,

$$\frac{(k_x d)^2}{\omega^2 \mu_{yy} d \epsilon_z d} + \frac{(k_y d)^2}{\omega^2 \mu_{xx} d \epsilon_z d} = 1. \tag{2.9}$$

Comparing (2.6) and (2.9), one notices that there is a one-to-one relationship between a medium with material parameters $(\bar{\bar{\mu}}, \epsilon_z)$ and the electrical network shown in Fig. 2.5(b) with parameters $(\bar{\bar{Z}}, Y)$. The following substitutions simply need to be made to go from the material to the electrical network,

$$\begin{aligned} j\omega\epsilon_z d &\longrightarrow Y, \\ j\omega\mu_{yy} d &\longrightarrow z_{xx}, \\ j\omega\mu_{xx} d &\longrightarrow z_{yy}. \end{aligned} \tag{2.10}$$

Both the anisotropic medium and it's analogous electrical network possess diagonal tensors. They exhibit dispersion curves that are ellipses or hyperbolas, depending on the signs of the permeabilities (impedances). The principal axes of the ellipses/hyperbolas are aligned with those of the Cartesian coordinate system, since the tensor $\bar{\bar{Z}}$ is diagonal. In order to move the principal axes of the dispersion curves off the coordinate system's axes, a full permeability (impedance) tensor is required.

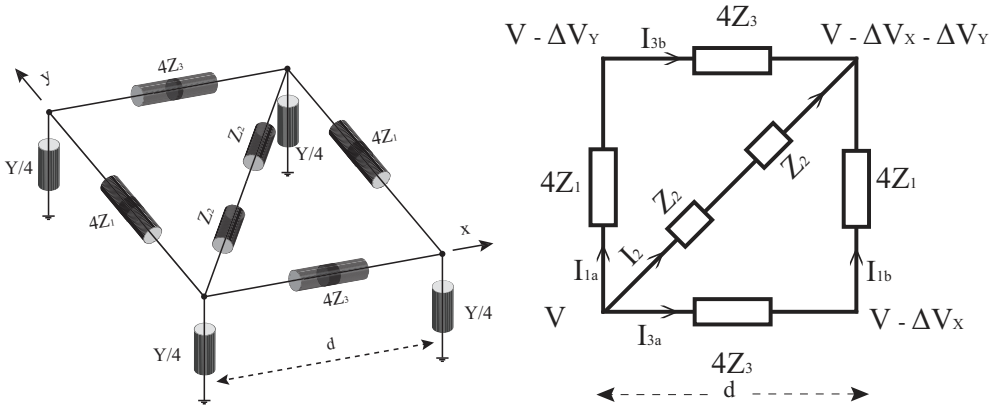

(a) Perspective view of the 3-branch transmission-line metamaterial unit cell.

(b) The configuration used to extract the impedance tensor of the 3-branch transmission-line metamaterial unit cell.

Figure 2.7: The 3-branch tensor transmission-line metamaterial unit cell.

As will be shown in the next section, this goal can be achieved by using a more general unit cell topology.

2.3 Tensor Transmission-line Metamaterials

To design a transmission-line metamaterial with a full 2x2 $\bar{\bar{Z}}$ tensor, let us consider the circuit shown in Fig. 2.7(a). This configuration will be referred to as 3-branch structure. In addition to having series impedances in the x and y directions, it has impedances along the $x-y$ diagonal. These diagonal impedances give rise to off-diagonal terms in the impedance tensor. The developed tensor analysis can be applied to this circuit to derive its impedance tensor.

Considering the Fig. 2.7(b), net currents in the x and y directions can be written as,

$$\begin{aligned} I_x &= I_{3a} + I_{3b} + I_2, \\ I_y &= I_{1a} + I_{1b} + I_2. \end{aligned} \tag{2.11}$$

Applying the same procedure as before, the admittance tensor $\bar{\bar{Y}}$ can be derived using

Fig. 2.7(b),

$$\bar{\bar{Y}} = \begin{bmatrix} y_{xx} & y_{xy} \\ y_{yx} & y_{yy} \end{bmatrix} = \begin{bmatrix} \frac{1}{2Z_2} + \frac{1}{2Z_3} & \frac{1}{2Z_2} \\ \frac{1}{2Z_2} & \frac{1}{2Z_1} + \frac{1}{2Z_2} \end{bmatrix}. \tag{2.12}$$

The impedance tensor $\bar{\bar{Z}} = \bar{\bar{Y}}^{-1}$, representing the series branches of the network shown in Fig. 2.7(a), can then be found,

$$\bar{\bar{Z}} = \begin{bmatrix} z_{xx} & z_{xy} \\ z_{yx} & z_{yy} \end{bmatrix} = \begin{bmatrix} \frac{2Z_3(Z_1+Z_2)}{Z_1+Z_2+Z_3} & \frac{-2Z_1Z_3}{Z_1+Z_2+Z_3} \\ \frac{-2Z_1Z_3}{Z_1+Z_2+Z_3} & \frac{2Z_1(Z_2+Z_3)}{Z_1+Z_2+Z_3} \end{bmatrix}. \tag{2.13}$$

The dispersion equation for the network becomes,

$$(k_x d)^2 \left(\frac{z_{yy}}{z_{xx}z_{yy} - z_{xy}z_{yx}} \right) - (k_x d)(k_y d) \left(\frac{z_{xy} + z_{yx}}{z_{xx}z_{yy} - z_{xy}z_{yx}} \right) + (k_y d)^2 \left(\frac{z_{xx}}{z_{xx}z_{yy} - z_{xy}z_{yx}} \right) = -Y. \tag{2.14}$$

Substituting (2.13) into (2.14) yields,

$$(k_x d)^2 \left(\frac{1}{2Z_3} + \frac{1}{2Z_2} \right) + (k_x d)(k_y d) \left(\frac{1}{Z_2} \right) + (k_y d)^2 \left(\frac{1}{2Z_1} + \frac{1}{2Z_2} \right) = -Y. \tag{2.15}$$

Propagation along the network depicted in Fig. 2.7(a) can be related to S-polarized (z-directed electric field polarization) propagation within an anisotropic medium with a full 2x2 permeability tensor,

$$\bar{\bar{\mu}} = \begin{bmatrix} \mu_{xx} & \mu_{xy} \\ \mu_{yx} & \mu_{yy} \end{bmatrix} \tag{2.16}$$

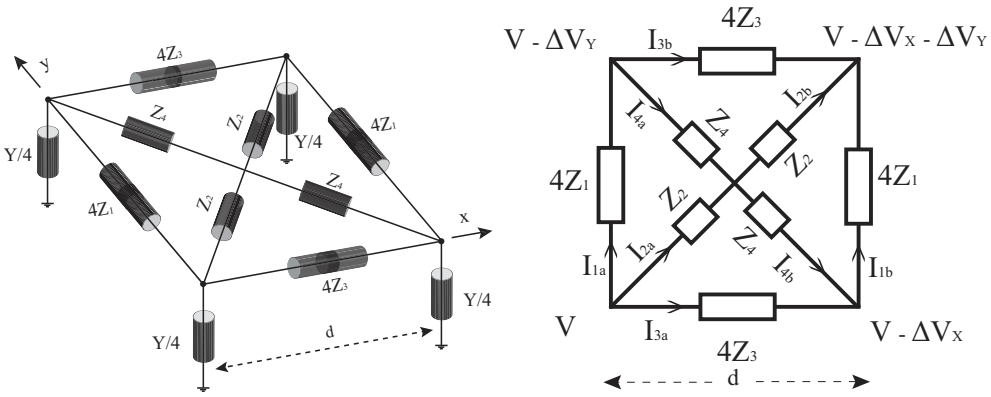

(a) Perspective view of the 4-branch transmission-line metamaterial unit cell.

(b) The configuration used to extract the impedance tensor of the 4-branch transmission-line metamaterial unit cell.

Figure 2.8: The 4-branch tensor transmission-line metamaterial unit cell.

and permittivity ϵ_z in the z direction. The dispersion equation of such a medium is,

$$\frac{(k_x)^2}{\omega^2}\left(\frac{\mu_{xx}}{\mu_{xx}\mu_{yy}-\mu_{xy}\mu_{yx}}\right)+\frac{(k_x)(k_y)}{\omega^2}\left(\frac{\mu_{xy}+\mu_{yx}}{\mu_{xx}\mu_{yy}-\mu_{xy}\mu_{yx}}\right)+ \frac{(k_y)^2}{\omega^2}\left(\frac{\mu_{yy}}{\mu_{xx}\mu_{yy}-\mu_{xy}\mu_{yx}}\right)=\epsilon_z. \quad (2.17)$$

In order to go from the effective medium (2.17) to the electrical network (2.14), the following substitutions are required,

$$\begin{aligned} j\omega\mu_{xy}d &\longrightarrow -z_{xy}, \\ j\omega\mu_{yx}d &\longrightarrow -z_{yx}, \end{aligned} \quad (2.18)$$

in addition to those given by (2.9).

For even greater design flexibility, let us consider the network shown in Fig. 2.8(a), which has impedances along both diagonals of the unit cell. This configuration will be referred to as 4-branch structure. To derive the $\bar{\bar{Y}}$ tensor, the following system of equations can be written for the net currents in the x and y directions (see Fig.

2.8(b)),

$$\begin{aligned} I_x &= I_{3a} + I_{3b} + I_{2a} + I_{4a} \\ &= I_{3a} + I_{3b} + I_{2b} + I_{4b}, \\ I_y &= I_{1a} + I_{1b} + I_{2a} - I_{4b} \\ &= I_{1a} + I_{1b} + I_{2b} - I_{4a}. \end{aligned} \tag{2.19}$$

From these equations, the following admittance tensor $\bar{\bar{Y}}$ can be written for the transmission-line metamaterial shown in Fig. 2.8(a),

$$\bar{\bar{Y}} = \begin{bmatrix} \frac{1}{2Z_2} + \frac{1}{2Z_3} + \frac{1}{2Z_4} & \frac{1}{2Z_2} - \frac{1}{2Z4} \\ \frac{1}{2Z_2} - \frac{1}{2Z_4} & \frac{1}{2Z_1} + \frac{1}{2Z_2} + \frac{1}{2Z_4} \end{bmatrix}. \tag{2.20}$$

The corresponding impedance tensor $\bar{\bar{Z}} = \bar{\bar{Y}}^{-1}$ is,

$$\bar{\bar{Z}} = \begin{bmatrix} z_{xx} & z_{xy} \\ z_{yx} & z_{yy} \end{bmatrix} = \begin{bmatrix} \frac{2Z_3(Z_1Z_2+Z_1Z_4+Z_2Z_4)}{Z_D} & \frac{2Z_1Z_3(Z_2-Z_4)}{Z_D} \\ \frac{2Z_1Z_3(Z_2-Z_4)}{Z_D} & \frac{2Z_1(Z_2Z_3+Z_2Z_4+Z_3Z_4)}{Z_D} \end{bmatrix} \tag{2.21}$$

where,

$$Z_D = Z_1Z_2 + 4Z_1Z_3 + Z_1Z_4 + Z_2Z_3 + Z_2Z_4 + Z_3Z_4. \tag{2.22}$$

The dispersion equation of the transmission-line metamaterial shown in Fig. 2.8(a) can be found by substituting the $\bar{\bar{Z}}$ tensor entries from (2.21) into (2.14),

$$(k_xd)^2\left(\frac{1}{2Z_3} + \frac{1}{2Z_2} + \frac{1}{2Z_4}\right) + (k_xd)(k_yd)\left(\frac{1}{Z_2} - \frac{1}{Z_4}\right) + (k_yd)^2\left(\frac{1}{2Z_1} + \frac{1}{2Z_2} + \frac{1}{2Z_4}\right) = -Y. \tag{2.23}$$

It should be mentioned that impedances on the $y = x$ diagonal appear as positive entries in the Z tensor, while those on the $y = -x$ diagonal appear as negative entries.

Therefore, depending on the desired frequency dependence of the parameters, one may want to choose an impedance on one diagonal as opposed to the other. For example, at a certain frequency of operation, an inductance on the $y = x$ diagonal can be chosen to give the same z_{xy} entry as capacitance on the $y = -x$ diagonal. The resulting frequency variation of the two choices, however, would be quite different: ω vs. $\frac{1}{\omega}$.

In summary, the unit cell of Fig. 2.8(a) provides a general circuit topology that can be related to a homogeneous, anisotropic medium with 2×2 permeability tensor and a permittivity scalar. The relationship between the material properties of a homogenous medium $(\bar{\bar{\mu}}, \epsilon_z)$ and the circuit elements $(\bar{\bar{Z}}, Y)$ are provided by (2.10, 2.18):

$$\begin{bmatrix} j\omega\mu_{yy}d & -j\omega\mu_{xy}d \\ -j\omega\mu_{yx}d & j\omega\mu_{xx}d \end{bmatrix} \Longrightarrow \begin{bmatrix} Z_{xx} & Z_{xy} \\ Z_{yx} & Z_{yy} \end{bmatrix}$$
$$j\omega\epsilon_z d \Longrightarrow Y \tag{2.24}$$

The diagonal impedances (Z_2 and Z_4) lead to off-diagonal tensor impedance elements (Z_{xy} and Z_{yx}). These diagonal impedances allow a net current in one direction (for example I_x, which is representative of magnetic field intensity component H_y) to give rise to series voltage drops in both the x and y directions (V_x and V_y, which are proportional to the magnetic flux density components B_y and B_x). Therefore, by properly selecting the values of Z_1, Z_2, Z_3 and Z_4 one can design a metamaterial with arbitrary magnetic anisotropy $(\bar{\bar{\mu}})$ and permittivity constant (ϵ_z).

In addition to the tensor transmission-line metamaterial unit cell shown in Fig. 2.8(a), the unit cell topology shown in Fig. 2.9 can also be used to synthesize anisotropic material parameters [69]. Through the proposed tensor analysis, it can be shown that the impedance tensor $\bar{\bar{Z}}$ and admittance scalar Y of the unit cells in Fig.

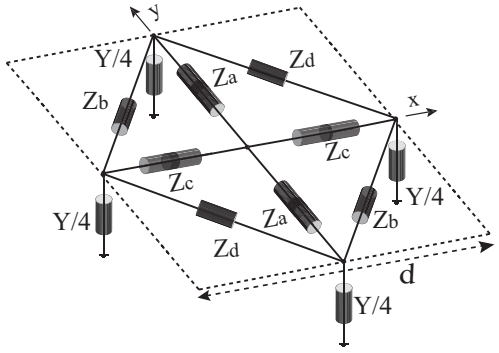

Figure 2.9: Alternative tensor transmission-line metamaterial topology in general form.

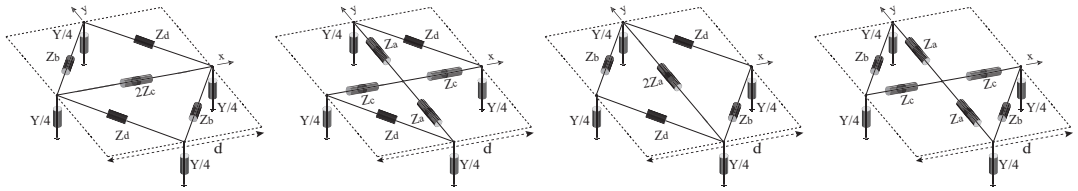

Figure 2.10: Variations of the unit cell in Fig. 2.9. Only one of the impedances (Z_a, Z_b, Z_c, Z_d) is open-circuited in each topology.

2.8(a) and Fig. 2.9 are of the same form. They can be designed to be the identical by simply setting $Z_1 = Z_a$, $Z_2 = Z_b$, $Z_3 = Z_c$ and $Z_4 = Z_d$. Furthermore, variations of the unit cell in Fig. 2.9 which utilize only three of four impedances (Z_a, Z_b, Z_c, Z_d), can also be shown to realize full material tensors. These topologies are shown in Fig. 2.10, where only one of the impedances (Z_a, Z_b, Z_c, Z_d) is open-circuited in each topology.

The unit cell topologies in Fig. 2.8(a) and Fig. 2.9 provide an alternative to the designer. One topology may have advantages over the other for a given application. For example, when implementing an anisotropic, inhomogeneous medium using unit cells in Fig. 2.8(a), one needs to combine the impedances of the adjacent unit cells. This, however, is not the case for the unit cell in Fig. 2.9. In this topology, the series impedances do not run along the sides of a unit cell, but are rather confined within the cell itself.

2.4 Bloch Analysis and Terminations

The approximate tensor analysis shown in the previous section did not consider spatial dispersion. It inherently assumed that the phase delays across the unit cell in the x and y directions were small. Here, we perform a Bloch analysis of the TL metamaterial shown in Fig. 2.8(a), in order to derive accurate dispersion equations that take into account spatial dispersion. Bloch analysis is only performed on the TL metamaterial in Fig. 2.8(a), since those shown in Figs. 2.5(b) and 2.7(a) can be derived from it.

An infinite structure consisting of unit cells depicted in Fig. 2.8(a) can be analyzed by applying Bloch boundary conditions to the voltages at the edges of the unit cell. As shown in Fig. 2.11, the voltages across the unit cell can be related to each other by the Bloch wavenumbers k_x and k_y. Once the voltages are assigned in this manner, the currents on the branches of the unit cell can be written in terms of Z_1, Z_2, Z_3, Z_4, $k_x d$ and $k_y d$:

$$I_{1a} = \frac{V(1-e^{-jk_y d})}{4Z_1}, \qquad I_{1b} = \frac{Ve^{-jk_x d}(1-e^{-jk_y d})}{4Z_1},$$
$$I_{3a} = \frac{V(1-e^{-jk_x d})}{4Z_3}, \qquad I_{3b} = \frac{Ve^{-jk_y d}(1-e^{-jk_x d})}{4Z_3},$$

$$\begin{aligned}
I_{2a} &= \frac{V(Z_4 - Z_2(e^{-jk_x d} + e^{-jk_y d}) + 2Z_2 - Z_4 e^{-j\gamma})}{2Z_2(Z_2+Z_4)}, \\
I_{2b} &= \frac{V(Z_4 + Z_2(e^{-jk_x d} + e^{-jk_y d}) - 2Z_2 e^{-j\gamma} - Z_4 e^{-j\gamma})}{2Z_2(Z_2+Z_4)}, \\
I_{4a} &= \frac{V(-Z_4 - Z_2(e^{-jk_x d} - e^{-jk_y d}) + 2Z_4 e^{-jk_y d} - Z_4 e^{-j\gamma})}{2Z_4(Z_2+Z_4)}, \\
I_{4b} &= \frac{V(Z_4 - Z_2(e^{-jk_x d} - e^{-jk_y d}) - 2Z_4 e^{-jk_x d} + Z_4 e^{-j\gamma})}{2Z_4(Z_2+Z_4)},
\end{aligned} \tag{2.25}$$

where

$$\gamma = k_x d + k_y d.$$

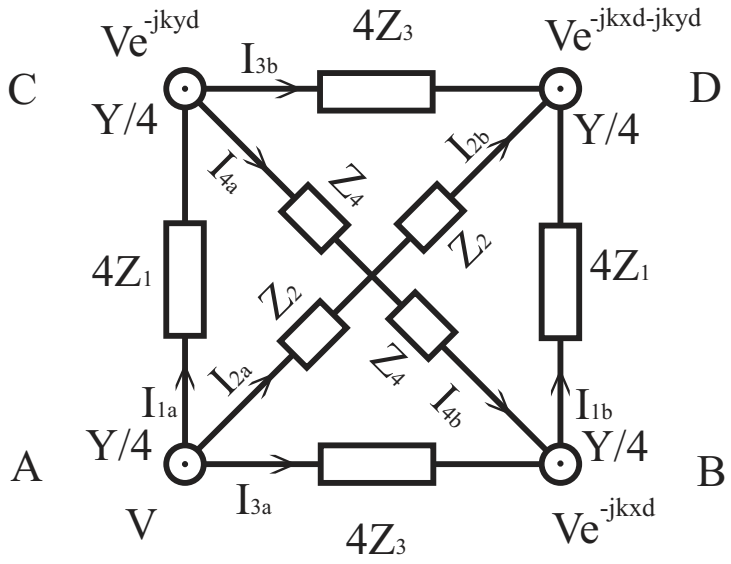

Figure 2.11: Top view of the 4-branch tensor transmission-line metamaterial unit cell of Fig. 2.8(a) under a Bloch wave excitation.

Applying Kirchhoff's Current Law (KCL) to a node where four neighboring unit cells intersect yields the following equation,

$$I_{1a}e^{-jk_xd} + I_{1b} + I_{3a}e^{-jk_yd} + I_{3b} + I_{2b} + I_{4b}e^{-jk_yd} -$$
$$(I_{1b}e^{-jk_yd} + I_{1a}e^{-j\gamma} + I_{2a}e^{-j\gamma} + I_{3a}e^{-j\gamma} + I_{3b}e^{-jk_xd} + I_{4a}e^{-jk_xd} + 4I_Ye^{-j\gamma}) = 0, \tag{2.26}$$

where

$$I_Y = \frac{VY}{4}. \tag{2.27}$$

By substituting the current expressions from (2.25) into the expression (2.26), the exact dispersion equation is obtained,

$$\left(\frac{4}{Z_2+Z_4} + \frac{2}{Z_3}\right)\sin^2(\frac{k_xd}{2}) + \left(\frac{2Z_4}{Z_2(Z_2+Z_4)}\right)\sin^2(\frac{\gamma}{2}) +$$
$$\left(\frac{2Z_2}{Z_4(Z_2+Z_4)}\right)\sin^2(\frac{\zeta}{2}) + \left(\frac{4}{Z_2+Z_4} + \frac{2}{Z_1}\right)\sin^2(\frac{k_yd}{2}) = -Y \tag{2.28}$$

where,

$$\gamma = k_x d + k_y d, \qquad \zeta = k_x d - k_y d. \tag{2.29}$$

For the frequency range where the per-unit-cell phase delays are small ($k_x d \ll 1$, $k_y d \ll 1$), the periodic network can be considered as an effective medium. Under these conditions, the dispersion equation above simplifies to (2.23) obtained using the approximate tensor analysis.

The developed Bloch analysis of tensor transmission-line metamaterials can be used to find the Bloch wave impedances. These impedances are needed to terminate Bloch waves on finite transmission-line metamaterial devices and are used to eliminate reflections (reflected Bloch waves) at the terminals of the unit cells. The terminations are derived for a Bloch wave defined by a specific wavevector: (k_x, k_y). The four nodes (corners) of the unit cell shown in Fig. 2.11 have been labeled A, B, C and D. The currents out of the nodes are named I_A, I_B, I_C, I_D, respectively. The current out of each node can be expressed in terms of the currents defined by (2.25) as follows,

$$\begin{aligned} I_A &= -(I_{1a} + I_{2a} + I_{3a} + I_Y), & I_B &= -(I_{1b} - I_{3a} - I_{4b} + I_Y e^{-jk_x d}), \\ I_C &= -(-I_{1a} + I_{3b} + I_{4a} + I_Y e^{-jk_y d}), & I_D &= -(-I_{1b} - I_{2b} - I_{3b} + I_Y e^{-jk_x d - jk_y d}). \end{aligned} \tag{2.30}$$

The Bloch impedances Z_A, Z_B, Z_C, Z_D seen out of these nodes can then be computed by taking the ratio of the node voltage to the current out of the node,

$$\begin{aligned} Z_A &= \frac{V}{I_A}, & Z_B &= \frac{V}{I_B} e^{-jk_x d}, \\ Z_C &= \frac{V}{I_C} e^{-jk_y d}, & Z_D &= \frac{V}{I_D} e^{-jk_x d - jk_y d}. \end{aligned} \tag{2.31}$$

Since the currents I_A, I_B, I_C and I_D are defined out of the nodes for a specific Bloch

wave characterized by the wavevector (k_x, k_y), some of the Bloch impedances may have negative real parts. This simply implies that the actual current flows in the opposite direction. In the design and analysis of a finite structure consisting of tensor transmission-line metamaterials, the nodes of the unit cells at the edge of the finite device must be terminated to eliminate reflections. The positive Bloch impedance can be realized using passive circuit components. To realize the negative impedance, one may simply attach a voltage source with twice the voltage of the node itself and a source impedance equal to the negative of the Bloch impedance found.

2.5 Examples

In this section, the utility of transmission-line metamaterials and the presented analysis are demonstrated through three separate design examples. In these designs, the required isotropic and anisotropic medium parameters are implemented using tensor transmission-line metamaterials. The first example considers reflectionless refraction from an isotropic medium to an anisotropic medium. The earlier analysis and the equivalence between electrical networks and anisotropic materials will allow the design of two media that are impedance matched to each other. The second and third examples consider the design of well-known transformation electromagnetic devices requiring an anisotropic and inhomogeneous medium: a cylindrical invisibility cloak [37] and a field rotator [70] embedded within an isotropic medium. These three examples will verify the dispersion equations and termination expressions presented in the previous sections, as well as the equivalence between effective media theory and network theory. Furthermore, these examples will demonstrate the ability of tensor transmission-line metamaterials to model anisotropic media and manipulate electromagnetic waves in unusual ways.

2.5.1 Reflectionless Refraction

The first example considers reflectionless refraction from an isotropic to an anisotropic medium. In this example, the material parameters of the isotropic and anisotropic medium are selected to eliminate reflection for a specific angle of incidence. The isotropic and anisotropic media will be referred as medium 1 and medium 2, respectively.

Medium 1 is implemented using the unit cell shown in Fig. 2.5(b), whereas medium 2 is realized using the cell depicted in Fig. 2.7(a). The operating frequency is chosen to be 1.0 GHz. The unit cells of the media are assumed to have a cell dimension of $d = 8.4$ mm ($\lambda_0/36$ at the frequency of operation). In this example, we will also assume that the wave in medium 1 is incident at an angle of $\theta = 30^\circ$ with respect to the normal.

Medium 1 is an isotropic medium with material parameters,

$$\mu = 2\mu_o, \qquad \epsilon = \epsilon_o. \tag{2.32}$$

The second medium is chosen to be anisotropic with the following permeability tensor,

$$\bar{\bar{\mu}} = \begin{bmatrix} \mu_{xx} & \mu_{xy} \\ \mu_{yx} & \mu_{yy} \end{bmatrix} = \begin{bmatrix} 1.500 & -1.354 \\ -1.354 & 3.000 \end{bmatrix} \mu_o \tag{2.33}$$

and permittivity $\epsilon = \epsilon_o$. This particular anisotropic medium was chosen since it is impedance matched to medium 1, for the particular angle of incidence considered. It should be noted that this medium is only one of an infinite number of possibilities. According to anisotropic media theory, the refracted angle in medium 2 should be 22.27°. Given the unit cell dimension d, frequency of operation and the network equivalence stipulated by (2.10), medium 1 corresponds to the transmission-line

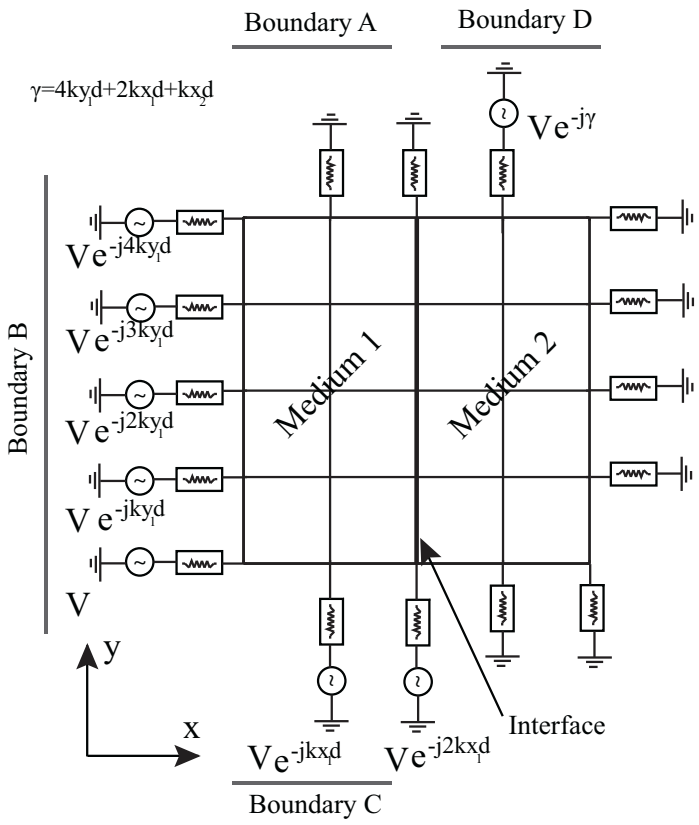

Figure 2.12: Set up for simulating reflectionless refraction between isotropic and anisotropic transmission-line metamaterials.

metamaterial shown in Fig. 2.5(b) with lumped element values,

$$L_1 = 10.556\ nH, \quad L_3 = 10.556\ nH, \quad C = 0.074\ pF, \tag{2.34}$$

where,

$$Z_1 = j\omega L_1, \;\; Z_3 = j\omega L_3, \;\; Y = j\omega C. \tag{2.35}$$

Once again, applying the substitutions given by (2.10) and (2.18), medium 2 corresponds to the transmission-line metamaterial shown in Fig. 2.7(a) with the following

electrical parameters,

$$L_1 = 3.233\ nH, \quad L_2 = -10.395\ nH, \quad L_3 = 4.931\ nH, \quad C\ = 0.074\ pF, \quad (2.36)$$

where

$$Z_1 = j\omega L_1,\ \ Z_2 = j\omega L_2,\ \ Z_3 = j\omega L_3,\ \ Y = j\omega C. \quad (2.37)$$

The angle of incidence and the phase matching condition along the interface between the two TL metamaterials stipulate per-unit-cell phase delays (in radians) in medium 1 and medium 2 to be $k_{x1}d = 0.216,\ k_{y1}d = 0.124$ and $k_{x2}d = 0.304,\ k_{y2}d = 0.124$, respectively.

Refraction at the interface between these two transmission-line metamaterials was simulated using Agilent's Advanced Design System (ADS) circuit simulator. Each metamaterial extended two unit cells in the x direction and four unit cells in the y direction. Therefore, the overall simulated structure was four by four unit cells, as shown in Fig. 2.12. The plane wave incident from medium 1 was generated using an array of linearly phased voltage sources along boundaries B and C, as shown in Fig. 2.12. A phased voltage source was also needed along boundary D, in order to eliminate the shadow along boundary D due to the finite interface [18]. The source impedances (boundaries B, C and D) and termination impedances (remaining boundaries) were found using the procedure outlined in the previous section. In other words, the edges of the overall structure were terminated to emulate refraction between two semi-infinite media.

A contour plot of the simulated voltage phases at the corners of the unit cells in both transmission-line metamaterials is shown in Fig. 2.13. The plot clearly shows an incident wave and refracted wave at the predicted angles.

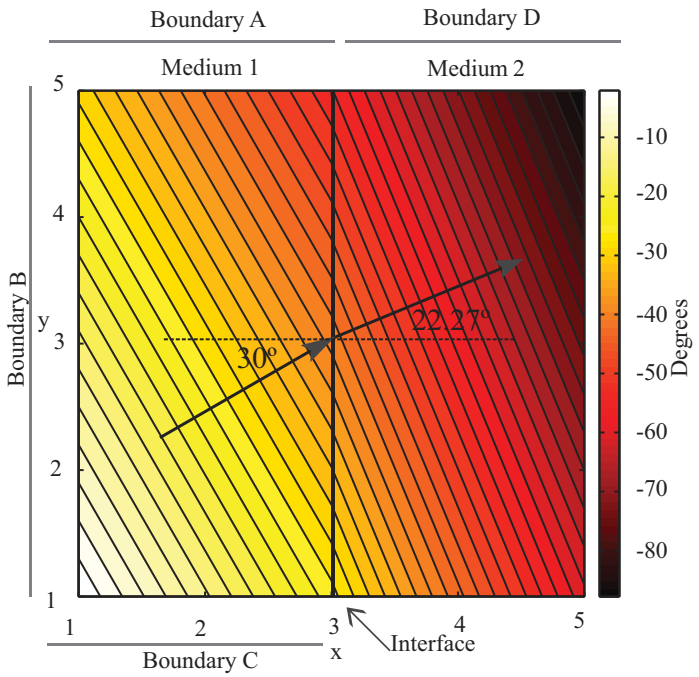

Figure 2.13: Contour plot of the voltage phase of a Bloch wave obliquely incident from an isotropic, homogenous transmission-line metamaterial onto a tensor transmission-line metamaterial.

2.5.2 Cylindrical Invisibility Cloak

The second example considers the implementation of a cylindrical invisibility cloak [37] using tensor transmission-line metamaterials. A cylindrical invisibility cloak is a transformation electromagnetic device that guides incident electromagnetic waves around a circle without perturbing the outside field distribution. An anisotropic, inhomogeneous annulus around the inner circle eliminates scattering, thus rendering the circle, together with any object hidden within, invisible.

The inner and outer radius of the cloak (annulus) are denoted by R_1 and R_2, respectively. The material parameters of the cylindrical cloak are taken from [37] for the specific case of S-polarized radiation (z-directed electric field),

$$\mu_r = \frac{r - R_1}{r}, \quad \mu_\phi = \frac{r}{r - R_1}, \quad \epsilon_z = (\frac{R_2}{R_2 - R_1})^2 \frac{r - R_1}{r}. \tag{2.38}$$

In the Cartesian system, this translates to,

$$\begin{aligned}
\mu_{xx} &= \mu_r \cos^2\phi + \mu_\phi \sin^2\phi, \\
\mu_{xy} &= \mu_{yx} = (\mu_r - \mu_\phi)\cos\phi\sin\phi, \\
\mu_{yy} &= \mu_r \sin^2\phi + \mu_\phi \cos^2\phi, \\
\epsilon_z &= (\frac{R_2}{R_2 - R_1})^2 \frac{r - R_1}{r}.
\end{aligned} \tag{2.39}$$

The medium surrounding the cloak is assumed to be isotropic and homogeneous: $\epsilon = \epsilon_0$ and $\mu = \mu_0$. An operating frequency of 3.57 GHz is selected and radii of $R_1 = 0.7\lambda_0$ and $R_2 = 1.4\lambda_0$ are chosen. To implement the cloak using tensor transmission-line metamaterials, the substitutions given by (2.10) and (2.18) are applied to the material parameters of the cloak and surrounding medium. The unit cell depicted in Fig. 2.7(a) is used to implement the cloak, while the surrounding medium is implemented using the unit cell of Fig. 2.5(b). The dimensions of each unit cell are assumed to be 8.4 mm ($\lambda_0/10$ at the operating frequency). The cloak and surrounding space are discretized according to Fig. 2.14(a), and the material parameters are defined with respect to the center of each unit cell. Each square in Fig. 2.14(a) represents a unit cell. The 460 unit cells that constitute the cloak are identified with dots in order to distinguish them from the surrounding medium.

In simulation, the left-most side of the structure was excited with in-phase voltage sources, in order to generate a plane wave incident from left to right. The voltage sources, as well as the right-most side of the structure, were terminated in accordance with Section 2.4: to emulate an infinite medium. The top and bottom edges of the simulated structure were open-circuited, as would be the case for a plane wave incident from left to right. As in the previous example, the voltages at the corners of each unit cell were computed using the ADS circuit simulator. A time snapshot of the steady-state voltages is plotted in Fig. 2.14(b). Some reflections to the left of the

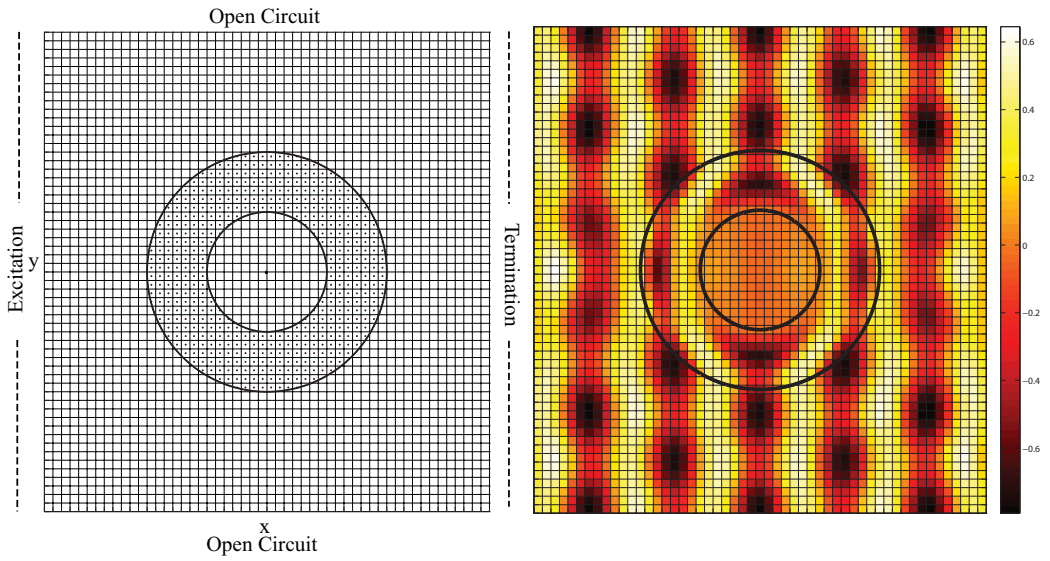

(a) (b)

Figure 2.14: (a) Simulation set up for a transmission-line based cylindrical invisibility cloak embedded within isotropic, homogeneous transmission-line medium.The discretization of the cloak and surrounding medium is shown. (b) Time snapshot of the simulated, steady-state voltages within and surrounding the invisibility cloak implemented using tensor transmission-line metamaterials.

cloak and a slight shadow to the right of the cloak are observed, which result from the cloak's discretization. Nevertheless, the field patterns characteristic of a cloak are quite prominent.

2.5.3 Cylindrical Field Rotator

The third and final example considers the field rotator device presented in [70]. The device rotates an incident electromagnetic field within a defined annulus by a prescribed angle. In this example, a 90 degree rotation of the incident field is considered. The material properties of the anisotropic and inhomogeneous annulus, and full-wave simulation results of an idealized field rotator are depicted in Fig. 2.15. The medium surrounding the field rotator is assumed to be isotropic and homogenous with relative permittivity of ϵ_r=1 and relative permeability of μ_r=1. An operating frequency of 2.0 GHz is selected for the simulation. The inner and outer radii of the

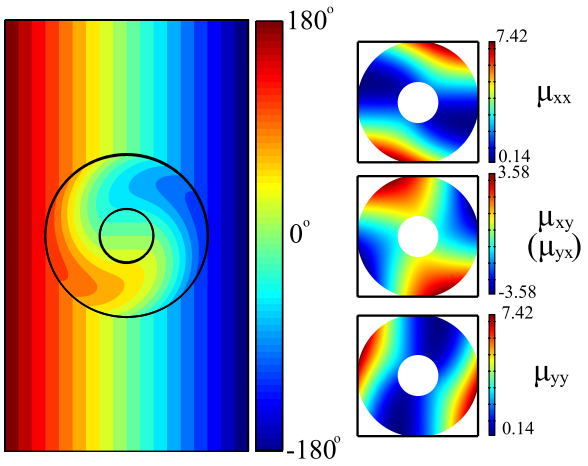

Figure 2.15: Simulated phase of the electric field within and surrounding the idealized electromagnetic field rotator, computed using a commercial finite element electromagnetic solver. Permeability values of the annulus are shown in the insets. The permeability of the surrounding medium is μ_r=1, and the permittivity of the entire structure is ϵ_r=1.

annulus are chosen to be 0.11 λ_0 and 0.33λ_0, respectively.

The circuit simulation set up for a field rotator device implemented using tensor transmission-line metamaterials is shown in Fig. 2.16(a). Each unit cell within the annulus is marked with a dot and represents an appropriately loaded tensor transmission-line unit cell (see Fig. 2.7(a)). The unit cells in the region surrounding the annulus model an isotropic medium. The unit cell depicted in Fig. 2.5(b) is used to implement the isotropic medium. In the simulation, the left-most side of the structure is excited with in-phase voltage sources which illuminate the field rotator with a plane wave. The right-most side of the structure is terminated with the Bloch impedance of the isotropic medium, in order to emulate an infinite medium. The top and bottom edges of the simulated structure are left open circuited. Voltage phases at the corners of each unit cell are computed using the ADS circuit simulator. The simulated voltage phase within and surrounding the field rotator implemented using tensor transmission-line metamaterials is shown in Fig. 2.16(b). As can be seen, the circuit simulation results closely match those of the idealized field rotator shown in Fig. 2.15.

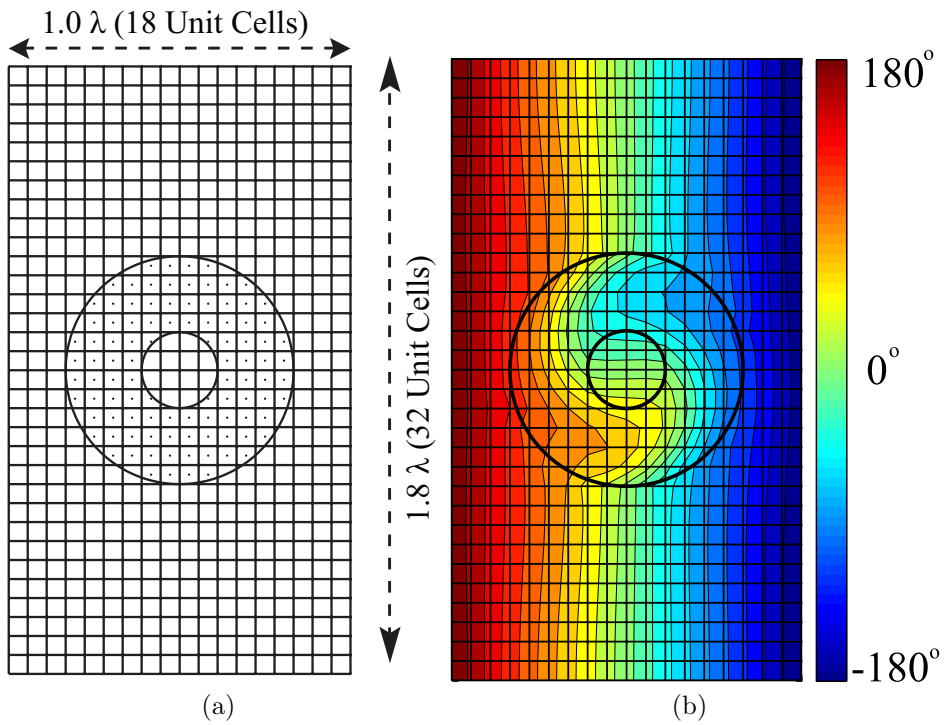

Figure 2.16: (a) Simulation set up for a transmission-line field rotator embedded within isotropic, homogeneous transmission-line medium. The discretization of the field rotator and surrounding medium is shown. (b) Simulated voltage phase within and surrounding the electromagnetic field rotator, implemented using tensor transmission-line metamaterials. The results were computed using Agilent's ADS circuit simulator.

These three examples verify the theoretical analysis of tensor transmission-line metamaterials presented in the previous sections. They also demonstrate the ability of tensor transmission-line metamaterials to realize anisotropic media and manipulate electromagnetic waves in unusual ways. The next section considers the implementation of tensor transmission-line circuit network at microwave frequencies.

2.6 Metamaterial Realization

Tensor transmission-line metamaterials directly relate material tensors to simple circuit networks. These circuit networks can then be implemented using either distributed or lumped circuit elements. This new approach to the design of tensor meta-

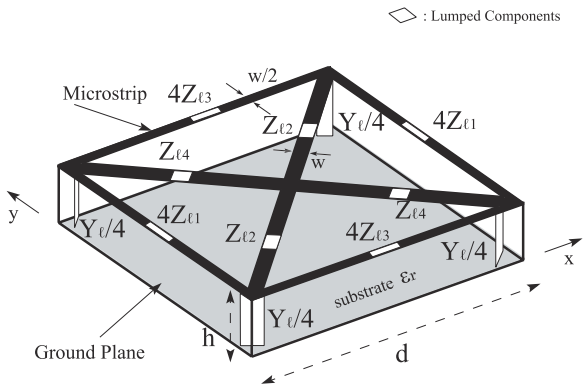

Figure 2.17: Microstrip implementation of the tensor transmission-line metamaterial depicted in Fig 2.8(a).

materials can be readily applied at RF, microwave and millimeter-wave frequencies, and possibly extended to higher frequencies by employing the concept of nano-circuit elements [71].

In this section, the implementation of tensor transmission-line metamaterials at microwave frequencies is considered. These metamaterials are first implemented as loaded 2D transmission-line networks in microstrip technology. Then, an equivalent circuit model of the implemented tensor transmission-line metamaterial is derived. It will be used to relate the material parameters of the implemented metamaterials to their homogeneous equivalent in the next section.

Fig. 2.17 depicts a practical realization of the tensor transmission-line metamaterial shown in Fig. 2.8(a). As shown in Fig. 2.17, printed microstrip lines are loaded with both series and shunt elements. Throughout this and following sections, the substrate is assumed to be lossless and have a relative permittivity of $\epsilon_r = 3$, and height $h = 1.524$ mm. The width, w, of the lossless metallic microstrip lines is 0.4 mm and the unit cell dimension is $d = 8.4$ mm.

A lumped element representation of the metamaterial depicted in Fig. 2.17 is shown in Fig. 2.18. The representation takes into account the transmission-line inductance and capacitance in addition to the loading elements. Such a representation is possible as the tensor transmission-line metamaterial unit cell and interconnecting

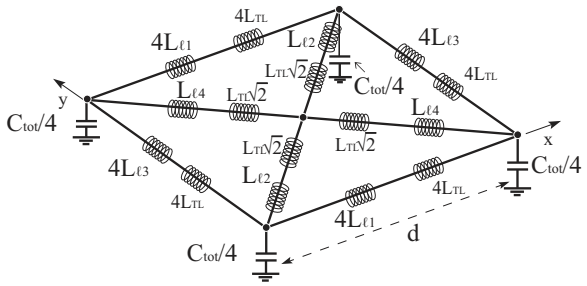

Figure 2.18: Lumped element representation of the tensor transmission-line metamaterial shown in Fig. 2.17. L_{TL}=$L_0 d/2$, C_{tot}=C_{TL} + C_ℓ, and C_{TL}=$2C_0 d(1+\sqrt{2})$.

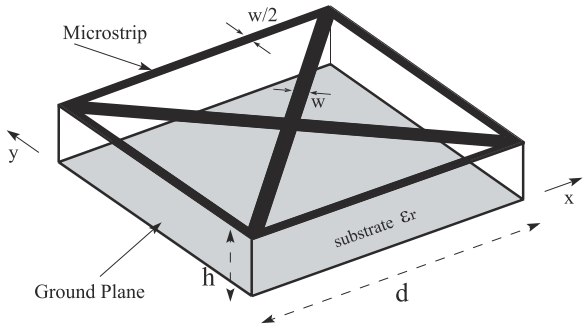

Figure 2.19: A unit cell of the unloaded microstrip transmission-line grid.

transmission-lines are assumed to be electrically small. In the figure, the series loading elements are assumed to be inductors and the shunt loading element a capacitor. The variables, $L_{\ell 1}$, $L_{\ell 2}$, $L_{\ell 3}$ and $L_{\ell 4}$, represent the series loading elements, whereas L_{TL} denotes the inductance of the interconnecting microstrip lines. The capacitance, C_{tot}, represents the sum of the transmission-line capacitance, C_{TL}, and the additional loading capacitance, C_ℓ. The caption of Fig. 2.18 provides expressions for C_{TL} and L_{TL} in terms of L_0 and C_0: the per-unit-length inductance and capacitance of the interconnecting transmission lines.

The values of L_0 and C_0 can be extracted from the unloaded microstrip grid's Bloch impedance and per-unit-cell phase delay. A unit cell of the unloaded transmission-line grid is depicted in Fig. 2.19, while its lumped element circuit model is shown in Fig. 2.20. Expressions for the Bloch impedance, Z_B, and Bloch wave number, k_B, of the unit cell shown in Fig. 2.20 can be easily derived for on-axis propagation. For

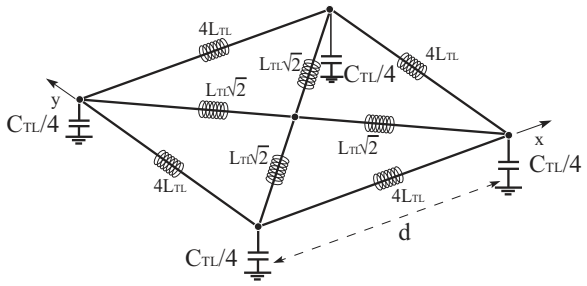

Figure 2.20: Lumped element representation of the unloaded microstrip transmission-line grid shown in Fig. 2.19. L_{TL}=$L_0 d/2$ and C_{TL}=$2C_0 d(1+\sqrt{2})$.

frequencies of operation where the cell's dimensions are electrically short, they can be expressed as

$$k_B = \omega\sqrt{2L_0C_0} \quad Z_B = \sqrt{\frac{L_0}{C_0}}(\frac{1}{2+\sqrt{2}}). \tag{2.40}$$

The Bloch wavenumber and impedance for on-axis propagation can also be expressed in terms of the unit cell's Z parameters obtained from on-axis scattering simulations on one unit cell [72]:

$$k_B d = \arccos(\frac{Z_{11}}{Z_{12}}) \quad Z_B = \sqrt{Z_{11}Z_{22} - Z_{12}Z_{21}}. \tag{2.41}$$

From full-wave simulation, the Z parameters of the unloaded transmission-line grid shown in Fig. 2.19 were found to be,

$$\begin{bmatrix} Z_{11} & Z_{12} \\ Z_{21} & Z_{22} \end{bmatrix} = -j \begin{bmatrix} 171.03 & 181.66 \\ 181.66 & 171.02 \end{bmatrix}. \tag{2.42}$$

Using these Z parameters and (2.41), Z_B and $k_B d$ for the unloaded grid were calculated to be

$$k_B d = 0.344\ rad \qquad Z_B = 61.244\ \Omega. \tag{2.43}$$

The Bloch wavenumber, Bloch impedance, and (2.40) were then used to extract the

following circuit parameters:

$$L_0 d = 8.090\ nH \qquad C_0 d = 0.185\ pF. \tag{2.44}$$

2.7 Full-wave Verification of Tensor TL Metamaterials

In this section, the analytical dispersion equation (2.23) for tensor transmission-line metamaterials is verified through three separate full-wave simulations. The three examples consider the proposed metamaterial unit cell (shown in Figure 2.17) with different sets of loading elements.

In the dispersion simulations (see Fig. 2.21), periodic (Bloch) boundary conditions were defined on the unit cell faces with normal unit vectors $\hat{x}$ and $\hat{y}$. A perfectly matched layer was placed at a distance seven times the substrate height above the microstrip lines, in order to represent the unbounded free space above. The full-wave eigenmode solver (Ansys HFSS) was then used to compute the isofrequency contours of the structure. First, let us consider the simulation of the unloaded unit cell shown in Fig. 2.19. At low frequencies, the infinite medium consisting of these unit cells is expected to be isotropic and homogeneous with isofrequency contours that are concentric circles. The analogous isotropic medium has the following material parameters: $\epsilon_z = 2.18\epsilon_0$ and

$$\begin{bmatrix} \mu_{yy} & \mu_{xy} \\ \mu_{yx} & \mu_{xx} \end{bmatrix} = \begin{bmatrix} 1.70 & 0 \\ 0 & 1.70 \end{bmatrix} \mu_0.$$

Fig. 2.22(a) shows the isofrequency contours computed using the full-wave eigenmode solver, and Fig. 2.22(b) compares them with those obtained analytically using 2.23. The analytical isofrequency contours are calculated by substituting the following

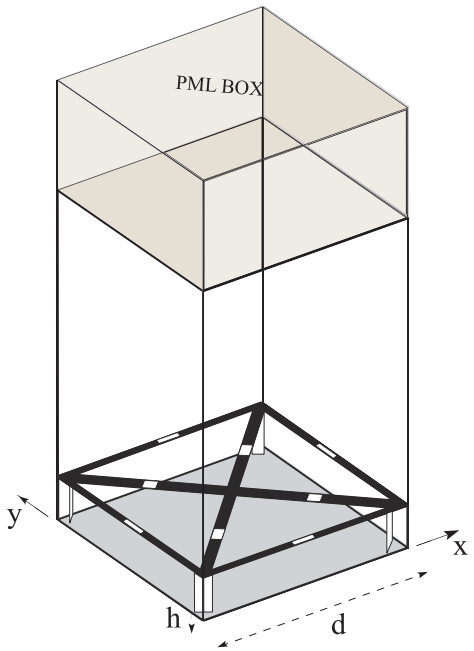

Figure 2.21: Eigenmode simulation set up. Periodic (Bloch) boundary conditions were defined on the unit cell faces with normal unit vectors $\hat{x}$ and $\hat{y}$. A perfectly matched layer was placed above microstrip lines to represent unbounded free space above.

values

$$Z_1 = j\omega L_{TL}, \qquad Z_2 = j\omega L_{TL}\sqrt{2}, \qquad Z_3 = j\omega L_{TL}, \qquad Z_4 = j\omega L_{TL}\sqrt{2},$$
$$Y = j\omega C_{tot} = j\omega C_{TL}. \tag{2.45}$$

into (2.23).

In the second example, the microstrip transmission-line grid is loaded with the following series inductive elements (see Fig. 2.18):

$$L_{\ell 1} = 4nH, \qquad L_{\ell 2} = 2nH, \qquad L_{\ell 3} = 16nH, \qquad L_{\ell 4} = 12nH. \tag{2.46}$$

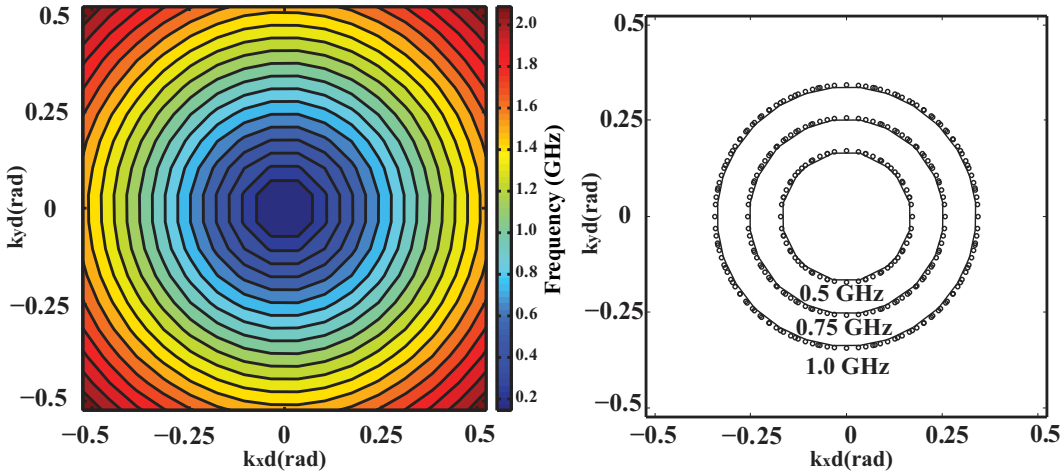

(a) Full-wave simulation results

(b) Analytical vs. full-wave simulation results

Figure 2.22: (a) Isofrequency dispersion contours of the unloaded microstrip grid depicted in Fig. 2.21. (b) The solid lines and dots show the simulated and analytical isofrequency contours, respectively.

The impedances and admittance of this metamaterial are

$$Z_1 = j\omega(L_{TL} + L_{\ell 1}),\ Z_2 = j\omega(L_{TL}\sqrt{2} + L_{\ell 2}),\ Z_3 = j\omega(L_{TL} + L_{\ell 3}),\ Z_4 = j\omega(L_{TL}\sqrt{2} + L_{\ell 4}),$$
$$Y = j\omega C_{tot} = j\omega C_{TL}. \tag{2.47}$$

The analogous magnetically anisotropic medium has the following material parameters: $\epsilon_z = 2.18\epsilon_0$ and

$$\begin{bmatrix} \mu_{yy} & \mu_{xy} \\ \mu_{yx} & \mu_{xx} \end{bmatrix} = \begin{bmatrix} 3.64 & 1.16 \\ 1.16 & 4.80 \end{bmatrix} \mu_0.$$

The metamaterial and its analogous medium are anisotropic and have elliptical isofrequency contours with a negative tilt angle of approximately -32^o from the x axis. The isofrequency contours obtained through full-wave simulations and those derived analytically using (2.23) are compared in Fig. 2.23.

The final example considers adding shunt, capacitive loading elements in addition

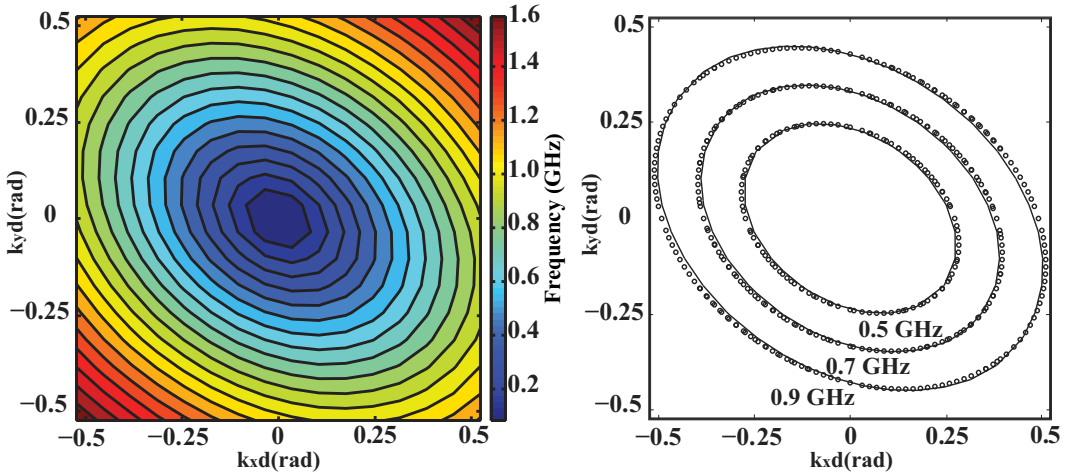

(a) Full-wave simulation results

(b) Analytical vs. full-wave simulation results

Figure 2.23: (a) Isofrequency dispersion contours of the tensor transmission-line metamaterial depicted in Fig. 2.18 with loading elements given by (2.46). (b) The solid lines and dots show the simulated and analytical isofrequency contours, respectively.

to series, inductive elements. By loading the structure with a shunt capacitance, the effective permittivity of the medium is increased over that of the unloaded grid. A shunt capacitance, $C_\ell = 0.4$ pF is added to the intrinsic capacitance of the microstrip transmission lines, C_{TL}, to yield

$$Y = j\omega C_{tot} = j\omega(C_{TL} + C_\ell). \tag{2.48}$$

The series inductive elements are chosen to be:

$$L_{\ell 1} = 4nH, \qquad L_{\ell 2} = 12nH, \qquad L_{\ell 3} = 16nH, \qquad L_{\ell 4} = 2nH. \tag{2.49}$$

This set of series inductive elements is slightly different from that given by (2.46). The values of $L_{\ell 2}$ and $L_{\ell 4}$ have been swapped in order to produce a positive tilt angle in the isofrequency contours. This sign change in tilt angle can be easily predicted from (2.23). The analogous magnetically anisotropic medium has the following material

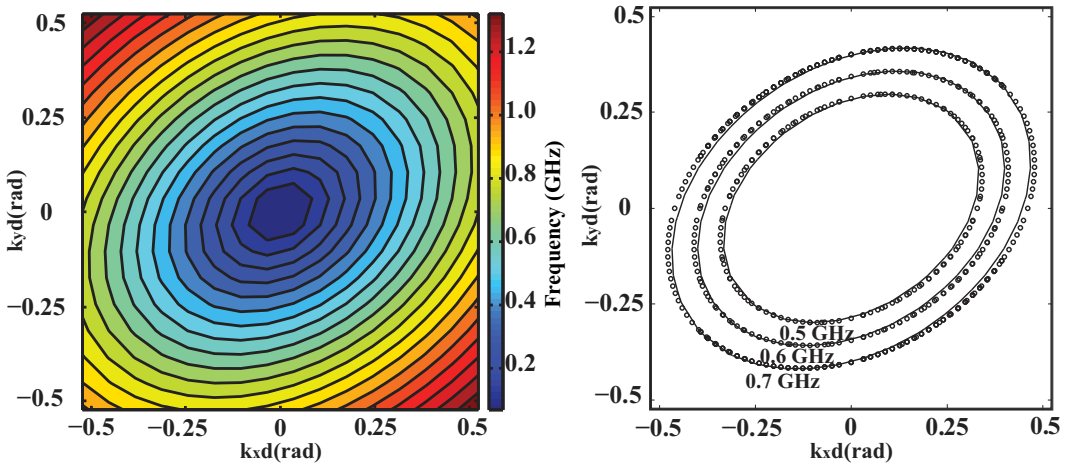

(a) Full-wave simulation results

(b) Analytical vs full-wave simulation results

Figure 2.24: (a) Isofrequency dispersion contours of the tensor transmission-line metamaterial depicted in Fig. 2.18 with loading elements given by (2.49) and (2.48). (b) the solid lines and dots show the simulated and analytical isofrequency contours, respectively.

parameters: $\epsilon_z = 3.15\epsilon_0$ and

$$\begin{bmatrix} \mu_{yy} & \mu_{xy} \\ \mu_{yx} & \mu_{xx} \end{bmatrix} = \begin{bmatrix} 3.64 & -1.16 \\ -1.16 & 4.80 \end{bmatrix} \mu_0.$$

The simulated and analytical isofrequency contours are compared in Fig. 2.22. Once again, close agreement is observed between the simulated and analytically derived isofrequency contours. It should be noted that elliptical isofrequency contours are wider in Fig. 2.24(b) than in Fig. 2.23(b) due to the increase in effective permittivity of the medium. This final example shows that not only can the magnetic 2×2 tensor of the metamaterial be manipulated with series loading elements, but its effective permittivity can also be tailored using shunt loading elements.

2.8 Conclusion

In this chapter, a new class of transmission-line based metamaterials referred to as "tensor transmission-line metamaterials" was introduced. These new metamaterials can possess effective material parameters with arbitrary full tensors. This is in contrast to earlier transmission-line metamaterials which could only implement effective material parameters with diagonal tensors in the Cartesian basis. An approximate tensor approach to transmission-line metamaterial analysis was developed to characterize the proposed metamaterials. Such an analysis provided insight into their development. This approximate analysis was subsequently validated through rigorous Bloch analysis, and accurate dispersion equations and Bloch impedance expressions were derived. Simulation results of a reflectionless interface between an isotropic and anisotropic metamaterial, an invisibility cloak and a field rotator validated the analytical findings, and demonstrated the ability of tensor transmission-line metamaterials to manipulate electromagnetic waves in extreme ways. It was shown that these metamaterials could be realized by loading a microstrip grid with reactive elements. Finally, the propagation characteristics of tensor transmission-line metamaterials realized in microstrip technology have been verified through full-wave simulations.

Tensor transmission-line metamaterials allow arbitrary control of electromagnetic fields along a surface, and therefore will find application in antenna design. These metamaterials will allow designers to synthesize arbitrary surface current distributions, and as a result arbitrary antenna aperture illuminations. This technology will also find use in the design of antenna feeds, beam-forming networks, multiplexers, power dividers and couplers. A tensor transmission-line metamaterial inspired beamformer application has already been realized by Gandini et al. [73]. A variation of the tensor transmission-line unit cell was redesigned as a planar directional coupler with arbitrary output phase and power distributions. These couplers were then used

to design a compact butler matrix for beam-forming applications. Furthermore, tensor transmission-line metamaterials were used by Liu et al. experimental design of a field rotator and field concentrator [74, 75]. The idea of synthesizing anisotropic medium with transmission-line metamaterials was also pursued by other research groups [76, 77, 78]. These works created the anisotropy with transmission-line structures possessing skewed/non-orthogonal transmission-line grids [76, 77] and inductively coupled transmission-lines [78]. An issue with utilizing skewed transmission-lines unit cells to achieve an inhomogeneous, anisotropic medium that can arise is the crystal misalignment at the interface between two transmission-line metamaterials with different skewed angles. With tensor transmission-line metamaterials, we introduced a uniform, rectangular unit cell that can be used to implement arbitrary tensor materials. Such a scheme allows metamaterial discretization over a uniform grid, while permitting arbitrary material tensors with spatial gradients. The misalignment of unit cells can also be remedied by using non-uniform transmission-line discretization as proposed in [79].

The analytical derivations and the understanding of tensor transmission-line metamaterials developed in this chapter will be used in the subsequent chapters to further develop and design devices for guided and radiated fields.

CHAPTER III

Homogenization of Tensor TL Metamaterials

In the previous chapter, tensor transmission-line metamaterials have been proposed and shown to exhibit the properties of magnetically anisotropic media. The equivalence between tensor transmission-line metamaterials and magnetically anisotropic media was established by comparing the analytic dispersion equation of the metamaterial with that of a homogenous, anisotropic medium. Subsequently, this analytical equivalence was backed up by full-wave simulations that compared the dispersion data of a realized metamaterial with those of a anisotropic homogeneous medium.

In this chapter, the magnetic anisotropy of tensor metamaterials are further verified by retrieving their effective material parameters through a homogenization method. The proposed homogenization method employs a local field averaging procedure over a realized metamaterial unit cell to compute its effective material parameters. It is shown that the effective material parameters can be dispersive or non-dispersive. For the tensor metamaterials possessing dispersive effective material parameters, the homogenization method also takes advantage of the circuit topology of tensor transmission-line metamaterials to predict material parameters over a frequency range.

Although the material parameters of a tensor transmission-line metamaterials can be computed from its equivalent circuit model as shown in previous chapter, the pro-

posed homogenization method directly relates the realized metamaterial structure to its effective material parameters. In addition, the homogenization method can account for couplings inside the realized tensor transmission-line unit cell, which cannot be captured by the proposed circuit model. The method also provides an accurate and rapid characterization of tensor transmission-line metamaterials, promoting their use in the design of larger metamaterial structures.

The following section presents a brief background on metamaterial homogenization methods. Subsequently, the proposed homogenization method is detailed and applied to the microstrip implementation of tensor transmission-line metamaterials. Tensor transmission-line metamaterial configurations possessing dispersive and non-dispersive material parameters are considered. Finally, homogenization method is verified through full-wave simulation results.

3.1 Homogenization of Metamaterials

Metamaterials are artificially structured materials providing tailored electromagnetic properties. These materials are made up of subwavelength unit cells arranged with subwavelength spacings. Despite a metamaterial's discretized structure, they can be modelled as homogeneous materials as long as the unit cell dimension and the spacing between scatterers remain much smaller than the wavelength of operation. Under this condition, the metamaterials' electromagnetic properties can be expressed in terms of material parameters such as permittivity and permeability, as is done for conventional materials. The process of relating a metamaterial's electromagnetic characteristics to homogeneous material properties is known as homogenization. The computed parameters of metamaterials are referred to as "homogenized" or "effective" material parameters. They describe the "averaged" response of the metamaterials' unit cells to the electromagnetic fields. Since the material parameters of metamaterials are fundamental to their design and analysis, several homogenization methods

have been proposed to date. In general, an equivalence is drawn between a metamaterial structure and a homogeneous structure using the measured, simulated or calculated quantities. In the simplest homogenization method, scattering (reflection/transmission) coefficients of a finite length metamaterial slab are compared with to those of a homogeneous dielectric slab with the same thickness [80, 81, 82]. Further improvements to this homogenization method have been reported in [83, 84, 85, 86]. Another well-known homogenization method involves field averaging to convert microscopic fields within the metamaterial unit cells to averaged macroscopic fields [5, 87]. As compared to the scattering parameters method, where only the reflection and transmitted fields are considered, this method considers the field distribution on the unit cell boundaries. The field averaging method has proven effective in calculating the material parameters from eigenmode simulations of a single unit cell. Additional numerical algorithms incorporating external field sources with field averaging [88, 89] have also been put forth. Homogenization methods have been applied to well-known volumetric metamaterials such as wire media [4], split-ring resonator media [5], their combination [7], and numerous others ranging from DC to optical frequencies. Various material properties such as isotropy, anisotropy and bi-anisotropy have been extracted using homogenization methods.

Analytical homogenization methods for 1D [90] and 2D transmission-line metamaterials [18, 65] as well as related 2D mushroom structures [91] have also been studied in the past. However, field-averaging homogenization methods have not been applied to full-wave simulation data of transmission-line metamaterials. In this chapter, we present a method for calculating the effective medium parameters of tensor transmission-line metamaterials. The proposed homogenization method draws a one-to-one equivalence between a tensor transmission-line metamaterial and a parallel-plate waveguide filled with an anisotropic, homogeneous medium, as shown in Fig. 3.1. The method employs a local field averaging over the faces of the realized metama-

terial's unit cell to compute its effective material parameters. These effective material parameters can be dispersive or non-dispersive. To predict the frequency dispersion of the effective material parameters, circuit representations of tensor transmission-line metamaterial unit cells are used. Dispersive and non-dispersive material parameter extraction are considered and verified through full-wave simulation. The method allows an accurate and rapid calculation of the effective material parameters of a tensor transmission-line metamaterial unit cell. The described homogenization technique is applicable to isotropic and anisotropic transmission-line metamaterials that possess both diagonal material parameters [17, 18, 20, 21, 23, 22] and off diagonal material parameters [76, 77] in the Cartesian basis.

3.2 Homogenization Method for Tensor Transmission-line Metamaterials

The proposed homogenization method computes the effective material parameters of tensor transmission-line metamaterials by drawing a one-to-one equivalence between wave propagation on a tensor transmission-line metamaterial and parallel-plate waveguide medium shown in Fig. 3.1. Fig. 3.1(a) shows a microstrip implementation of a tensor transmission-line metamaterial unit cell considered in this chapter. The unit cell length and height are shown with d and h, respectively. The equivalent a parallel-plate waveguide medium consists of a magneto-dielectric medium sandwiched between two perfect electric conductors from top and bottom. The parallel plate waveguide is shown in Fig. 3.1(b). The unit cell shown has the same physical dimensions as the tensor transmission-line unit cell shown in Fig. 3.1(a). It is filled with a homogeneous magneto-dielectric with a relative permeability tensor $\bar{\bar{\mu}}$ and a

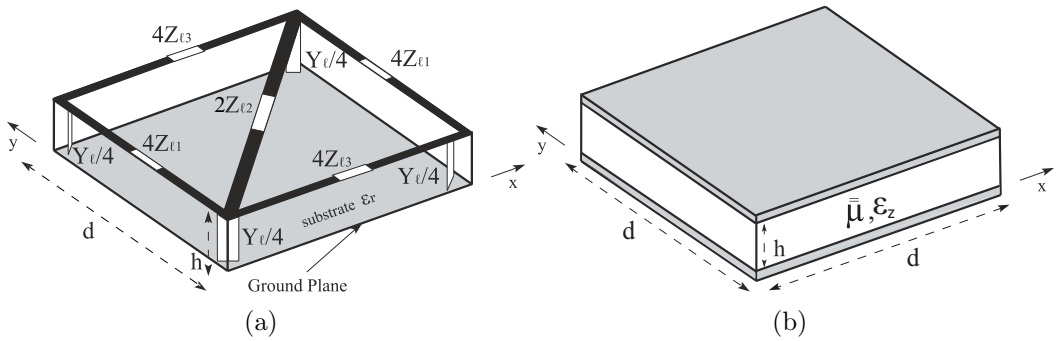

Figure 3.1: (a) Microstrip implementation of a tensor transmission-line metamaterial unit cell with series and shunt loading elements. (b) A parallel-plate waveguide equivalent to the tensor transmission-line metamaterial depicted in Fig. 3.1(a).

relative scalar permittivity ϵ

$$\bar{\bar{\mu}} = \begin{bmatrix} \mu_{xx} & \mu_{xy} \\ \mu_{yx} & \mu_{yy} \end{bmatrix}, \qquad \epsilon = \epsilon_z. \tag{3.1}$$

The homogenization method describes how to compute the permeability tensor and permittivity scalar of the equivalent parallel-plate waveguide (Eq. (3.1)) representing the tensor TL metamaterial. It draws an equivalence between the structures shown in Fig. 3.1(a) and Fig. 3.1(b) in terms of their (i) dispersion curves and (ii) effective impedances for all angles of wave propagation at a given frequency.

A full-wave solver is used to solve for the electromagnetic field distribution within a transmission-line metamaterial. The homogenization procedure then employs a field averaging technique over the faces of the metamaterial's unit cell, in addition to well-known analytical expressions for plane wave propagation in a homogeneous, anisotropic medium to compute the effective material parameters. The following subsections present a detailed analysis of tensor transmission-line and parallel plate waveguide media, and subsequently draw equivalence between them.

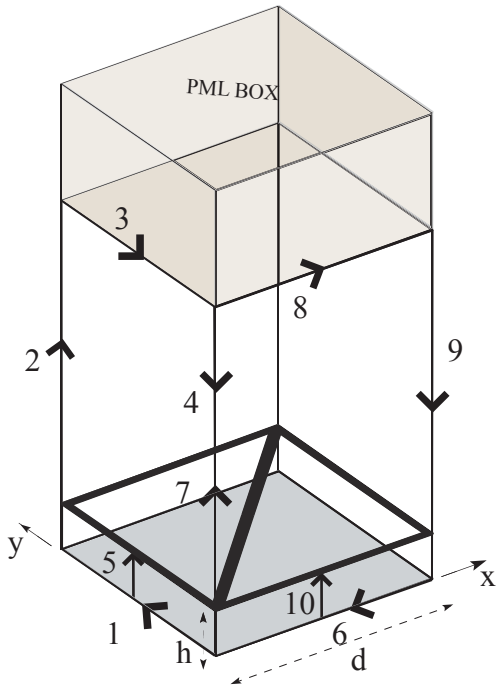

Figure 3.2: The eigenmode simulation setup. The integration paths used in the homogenization procedure are shown.

3.2.1 The Tensor TL Metamaterial as a Homogeneous Medium

The proposed homogenization procedure will be applied to a microstrip implementation of a tensor transmission-line metamaterial with the unit cell shown in Fig. 3.1(a). Fig. 3.2 depicts the set up that will be used to perform full-wave (eigenvalue/periodic) simulations of the tensor transmission-line metamaterial shown, from which material parameters will be extracted. The set up includes periodic boundaries on the sidewalls of the unit cell, and a perfectly matched layer (PML) on top to emulate unbounded free space. The integration paths shown on the faces of the unit cell will be used in the homogenization procedure. The eigenvalue problem is solved numerically using a commercial full-wave electromagnetic solver, Ansys HFSS. The local $\bar{E}$ and $\bar{H}$ field distributions within the unit cell are computed numerically for a given set of phase delays (periodic conditions) in the x and y directions. These phase delays across the unit cells must be chosen to be small for proper homogenization

of the metamaterial. By integrating the local fields on the faces of the unit cell, the following voltages V_x, V_y and currents I_x, I_y can be defined

$$V_x = -\int_{\ell 1} \overline{E} \cdot \overline{d_\ell}, \qquad V_y = -\int_{\ell 2} \overline{E} \cdot \overline{d_\ell},$$
$$I_x = \oint_{C_1} \overline{H} \cdot \overline{d_\ell}, \qquad I_y = \oint_{C_2} \overline{H} \cdot \overline{d_\ell}, \tag{3.2}$$

where paths C_1 and C_2 represent the closed contours consisting of the lines $1-2-3-4$ and $6-7-8-9$, respectively. Although the integration paths C_1 and C_2 extend to the perfectly matched layer (PML) in the z direction (see Fig. 3.2), this is not necessary. One may simply ensure that the closed path integrals enclose the net current flowing along the microstrip lines in the respective directions. The lines along which the $\bar{E}$ field is integrated, ℓ_1 and ℓ_2, are shown as line 5 and line 10 in Fig. 3.2, respectively. Using the voltage and current expressions of (3.2), impedances Z_x, Z_y in x and y directions can be defined

$$Z_x = \frac{V_x}{I_x}, \qquad Z_y = \frac{V_y}{I_y}. \tag{3.3}$$

3.2.2 Parallel Plate Waveguide

The circuit parameters defined by (3.2) and (3.3) have a one-to-one correspondence to the field quantities of a TEM wave propagating in the parallel-plate waveguide of Fig. 3.1(b) that is filled by a dielectric with material parameters in (3.1). For the polarization of interest, the non-zero field quantities within the parallel-plate region are the z component of electric field E_z and the x and y components of magnetic field: H_x and H_y. Using these field components, wave impedances along the x and y directions can be written for the parallel-plate waveguide

$$\eta_x = -\frac{E_z}{H_y} \qquad \eta_y = \frac{E_z}{H_x}. \tag{3.4}$$

Using the electric and magnetic field components, voltages and currents for the TEM mode of the parallel-plate waveguide shown in Fig. 3.1(b) can be defined

$$\begin{aligned} V_x &= -E_z h \qquad & V_y &= -E_z h \\ I_x &= \ H_y d \qquad & I_y &= -H_x d. \end{aligned} \tag{3.5}$$

3.2.3 Drawing an Equivalence

Using (3.4) and (3.5), the wave impedances of the parallel-plate waveguide can be related to the x and y directed circuit impedances by the following relation

$$\begin{bmatrix} Z_x \\ Z_y \end{bmatrix} = g\eta_0 \begin{bmatrix} \overline{\eta}_x \\ \overline{\eta}_y \end{bmatrix}, \tag{3.6}$$

where $g = \frac{h}{d}$, $\overline{\eta}_x$ and $\overline{\eta}_y$ are the wave impedances normalized with respect to their free space value, $\eta_0 = \sqrt{\frac{\mu_0}{\epsilon_0}}$.

In order for the tensor transmission-line metamaterial shown in Fig. 3.1(a) to be equivalent to the parallel-plate waveguide shown in Fig. 3.1(b), the dispersion curve and circuit impedances (Z_x, Z_y) for both structures must be the same. It is in fact this process of equating the circuit parameters of both structures that will allow us to compute the effective material parameters of tensor transmission-line metamaterials.

To understand the homogenization procedure, the plane-wave relations in the parallel plate waveguide filled with an anisotropic, homogeneous dielectric medium (3.1) are reviewed. For the polarization of interest, Maxwell's time-harmonic equations for plane waves are:

$$-j\vec{k} \times \vec{E} = -j\omega\bar{\bar{\mu}}\mu_o\vec{H}, \tag{3.7}$$

$$-j\vec{k} \times \vec{H} = j\omega\epsilon_z\epsilon_o\vec{E}. \tag{3.8}$$

Considering only the non-zero field quantities, these two vector equations can be rewritten as:

$$\begin{bmatrix} \overline{k}_y \\ \overline{k}_x \end{bmatrix} = \begin{bmatrix} \mu_{xx} & -\mu_{xy} \\ -\mu_{yx} & \mu_{yy} \end{bmatrix} \begin{bmatrix} \overline{\eta}_y{}^{-1} \\ \overline{\eta}_x{}^{-1} \end{bmatrix}, \tag{3.9}$$

$$\epsilon_z = \begin{bmatrix} \overline{k}_x & \overline{k}_y \end{bmatrix} \begin{bmatrix} \overline{\eta}_x{}^{-1} \\ \overline{\eta}_y{}^{-1} \end{bmatrix}. \tag{3.10}$$

where $\overline{\eta}_x = -\frac{1}{\eta_o}\frac{E_z}{H_y}$, $\overline{\eta}_y = \frac{1}{\eta_o}\frac{E_z}{H_x}$ are the wave impedances and $\overline{k}_x = \frac{k_x}{k_o}$, $\overline{k}_y = \frac{k_y}{k_o}$ are the wave numbers in the x and y directions, normalized with respect to their free space values. Note that the frequency of operation (f) can be deduced from the expression for the free space wave number, $k_o = \omega\sqrt{\mu_o\epsilon_o}$ where $\omega = 2\pi f$.

Substituting equation (3.6) into (3.9) and (3.10) yields

$$\begin{bmatrix} \overline{k}_y \\ \overline{k}_x \end{bmatrix} = g \begin{bmatrix} \mu_{xx} & -\mu_{xy} \\ -\mu_{yx} & \mu_{yy} \end{bmatrix} \begin{bmatrix} \overline{Z}_y{}^{-1} \\ \overline{Z}_x{}^{-1} \end{bmatrix} \eta_o, \tag{3.11}$$

$$\frac{\epsilon_z}{g} = \begin{bmatrix} \overline{k}_x & \overline{k}_y \end{bmatrix} \begin{bmatrix} \overline{Z}_x{}^{-1} \\ \overline{Z}_y{}^{-1} \end{bmatrix} \eta_o. \tag{3.12}$$

Using (3.11) and (3.12), the effective material parameters (ϵ, $\bar{\bar{\mu}}$) can be determined using the tensor transmission-line metamaterial's Z_x and Z_y impedances computed using two independent solution sets of (k_x, k_y, f). Two independent solutions are needed since there are four unknowns $(\mu_{xx}, \mu_{xy}, \mu_{yy}, \epsilon_z)$ and (3.9) and (3.10) provide only three equations. In other words, all that is required to find the material parameters are two full-wave eigenmode simulations of the tensor transmission-line metamaterial, and the field integrations given by (3.2) that allow Z_x, Z_y to be computed. Note, the metamaterial is assumed to be reciprocal: $\mu_{xy} = \mu_{yx}$.

The described homogenization procedure can be easily applied to tensor transmission-

line metamaterials that have frequency independent effective material parameters. For example, commercial electromagnetic eigenmode solvers allow users to stipulate phase delays ($k_x d$ and $k_y d$) across the unit cell and solve for frequency. Therefore, two such simulations with different eigenfrequencies can be used in the homogenization procedure, given that the material parameters are frequency independent.

When the effective material parameters of the tensor transmission-line metamaterial are frequency dispersive, the proposed homogenization method can still be used with certain caveats. For instance, two eigenmode simulations at the same frequency can be used to extract the effective material parameters at that frequency of operation. Unfortunately, commercial electromagnetic solvers do not allow users to stipulate frequency in an eigenmode simulation. Therefore, parametric sweeps may be required to find two eigenmode simulations at the same frequency. Alternatively, the frequency dependence of effective material parameters can be assumed, and the material parameters extracted from eigenmode simulations at different frequencies. As will be shown in the following section, the frequency dependence of the effective material parameters can be predicted from a tensor transmission-line metamaterial's circuit topology.

3.3 Frequency Dependence of Effective Material Parameters

In the described homogenization process, the effective material parameters of tensor transmission-line metamaterials were computed through a field averaging procedure. These material parameters can also be related to the circuit representation of

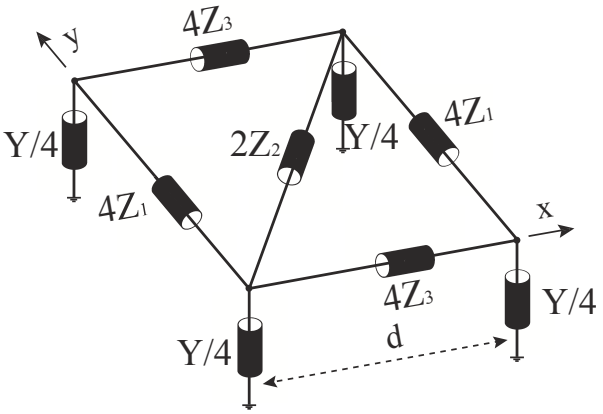

Figure 3.3: Circuit model of the tensor transmission-line metamaterial shown in Fig. 3.1(a).

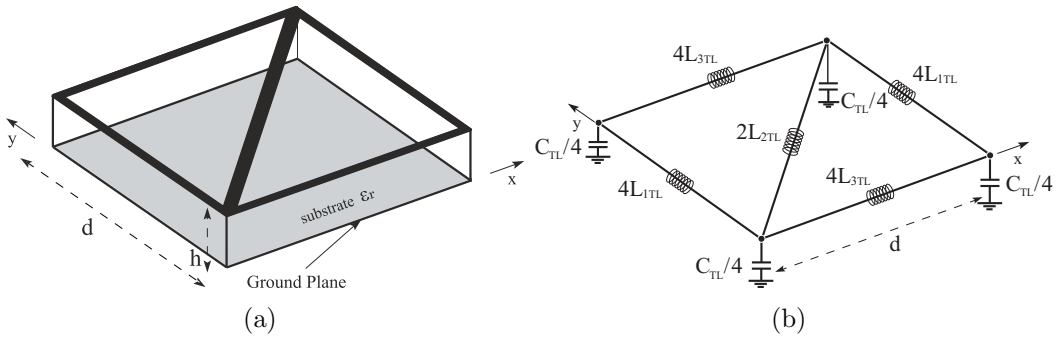

Figure 3.4: (a) A unit cell of the unloaded microstrip grid. (b) A circuit model of the unloaded microstrip grid depicted in Fig. 3.4(a).

the unit cell (see Fig. 3.3) by the following equations derived in Chapter 2:

$$\begin{bmatrix} j\omega\mu_{yy}d & -j\omega\mu_{xy}d \\ -j\omega\mu_{yx}d & j\omega\mu_{xx}d \end{bmatrix} = \frac{1}{g}\begin{bmatrix} Z_{xx} & Z_{xy} \\ Z_{yx} & Z_{yy} \end{bmatrix}$$

$$j\omega\epsilon_z d = gY, \tag{3.13}$$

where

$$\begin{bmatrix} Z_{xx} & Z_{xy} \\ Z_{yx} & Z_{yy} \end{bmatrix} = \begin{bmatrix} \frac{2Z_3(Z_1+Z_2)}{Z_1+Z_2+Z_3} & \frac{-2Z_1Z_3}{Z_1+Z_2+Z_3} \\ \frac{-2Z_1Z_3}{Z_1+Z_2+Z_3} & \frac{2Z_1(Z_3+Z_2)}{Z_1+Z_2+Z_3} \end{bmatrix}.$$

According to (3.13), the frequency dependence of the effective material parameters is determined by the series impedances, Z_1, Z_2, Z_3 and shunt admittance, Y.

3.3.1 Non-dispersive Material Parameters

Let's consider the unloaded microstrip unit cell shown in Fig. 3.4(a), with its circuit representation shown in Fig. 3.4(b). In the circuit model, the transmission lines are represented by series inductances $L_{1TL}, L_{2TL}, L_{3TL}$ and the shunt capacitance C_{TL}. It is assumed that interconnecting microstrip lines are electrically short. Therefore, the series impedances and shunt admittance (see Fig. 3.3) of the unit cell can be written as

$$\begin{gathered} Z_1 = j\omega(L_{1TL}) \qquad Z_2 = j\omega(L_{2TL}) \qquad Z_3 = j\omega(L_{3TL}) \\ Y = j\omega(C_{TL}). \end{gathered} \tag{3.14}$$

Substituting (3.14) into (3.13) yields the effective material parameters in terms of circuit quantities

$$\begin{gathered} \begin{bmatrix} \mu_{xx} & \mu_{xy} \\ \mu_{yx} & \mu_{yy} \end{bmatrix} = \frac{1}{dg} \begin{bmatrix} \frac{2L_{3TL}(L_{1TL}+L_{2TL})}{L_{1TL}+L_{2TL}+L_{3TL}} & \frac{2L_{1TL}L_{3TL}}{L_{1TL}+L_{2TL}+L_{3TL}} \\ \frac{2L_{1TL}L_{3TL}}{L_{1TL}+L_{2TL}+L_{3TL}} & \frac{2L_{1TL}(L_{3TL}+L_{2TL})}{L_{1TL}+L_{2TL}+L_{3TL}} \end{bmatrix}, \\ \epsilon_z = \frac{C_{TL}}{d} g. \end{gathered} \tag{3.15}$$

The equation above (3.15) also reveals the frequency dependence of the effective material parameters. In fact, it shows that the effective material parameters of the unloaded tensor TL metamaterial have no frequency dependence. This is due to the fact that the series impedances are inductive and the shunt admittances are capacitive (see Fig. 3.4). Realistically, however, the effective material parameters of the microstrip tensor TL metamaterial have a weak frequency dependence, due to the inherent frequency dispersion of microstrip lines.

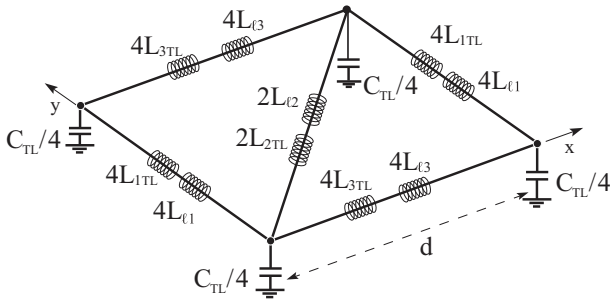

Figure 3.5: A circuit model of the tensor TL metamaterial unit cell depicted in Fig. 3.4(a) when all series loading elements are inductances.

Now, let us consider the case where the unloaded microstrip grid shown in Fig. 3.4(a) is loaded with series inductances. The circuit model for this particular example is depicted in Fig. 3.5. The series loading elements are denoted $L_{\ell1}, L_{\ell2}$ and $L_{\ell3}$. As a result, the impedances of the unit cell (see Fig. 3.3) become

$$\begin{gathered} Z_1 = j\omega(L_{1TL} + L_{\ell1}) \quad Z_2 = j\omega(L_{2TL} + L_{\ell2}) \quad Z_3 = j\omega(L_{3TL} + L_{\ell3}) \\ Y = j\omega(C_{TL}). \end{gathered} \tag{3.16}$$

Substituting (3.16) into (3.13) leads to the effective material parameters for a tensor TL metamaterial unit cell with inductive series loading elements

$$\begin{gathered} \begin{bmatrix} \mu_{xx} & \mu_{xy} \\ \mu_{yx} & \mu_{yy} \end{bmatrix} = \frac{1}{dg} \begin{bmatrix} \frac{2(L_{3TL}+L_{\ell3})(L_{1TL}+L_{\ell1}+L_{2TL}+L_{\ell2})}{L_{1TL}+L_{\ell1}+L_{2TL}+L_{\ell2}+L_{3TL}+L_{\ell3}} & \frac{2(L_{1TL}+L_{\ell1})(L_{3TL}+L_{\ell3})}{L_{1TL}+L_{2TL}+L_{3TL}} \\ \frac{2(L_{1TL}+L_{\ell1})(L_{3TL}+L_{\ell3})}{L_{1TL}+L_{2TL}+L_{3TL}} & \frac{2(L_{1TL}+L_{\ell1})(L_{3TL}+L_{\ell3}+L_{2TL}+L_{\ell2})}{L_{1TL}+L_{\ell1}+L_{2TL}+L_{\ell2}+L_{3TL}+L_{\ell3}} \end{bmatrix} \\ \epsilon_z = \frac{C_{TL}}{d} g. \end{gathered} \tag{3.17}$$

The material parameters once again are non-dispersive.

3.3.2 Dispersive Material Parameters

Now, let us consider a tensor transmission-line metamaterial unit cell possessing dispersive effective material parameters. The material parameters become dispersive

when some or all of the series loading impedances and shunt loading susceptances are negative. In this example, the diagonal branch of the unloaded tensor transmission-line unit cell shown in Fig. 3.4(a) is loaded with a capacitance of value C_ℓ. This series capacitance can simply be added to the diagonal branch of the circuit model for the unloaded unit cell depicted in Fig. 3.4(b). This results in the circuit model of the dispersive tensor TL metamaterial shown in Fig. 3.6. From the model, the impedance expressions of Fig. 3.3 become

$$\begin{gathered} Z_1 = j\omega(L_{1TL}) \qquad Z_2 = j\omega(L_{2TL} - \tfrac{1}{\omega^2(2C_\ell)}) \qquad Z_3 = j\omega(L_{3TL}) \\ Y = j\omega(C_{TL}). \end{gathered} \tag{3.18}$$

Substituting (3.18) into (3.13) reveals the frequency dependence of the effective material parameters of the unit cell shown in Fig. 3.6.

$$\begin{gathered} \begin{bmatrix} \mu_{xx} & \mu_{xy} \\ \mu_{yx} & \mu_{yy} \end{bmatrix} = \frac{1}{dg} \begin{bmatrix} \frac{2L_{3TL}(L_{1TL}+L_{2TL}-\frac{1}{\omega^2 2C_\ell})}{L_{1TL}+L_{2TL}-\frac{1}{\omega^2 2C_\ell}+L_{3TL}} & \frac{2L_{1TL}L_{3TL}}{L_{1TL}+L_{2TL}-\frac{1}{\omega^2 2C_\ell}+L_{3TL}} \\ \frac{2L_{1TL}L_{3TL}}{L_{1TL}+L_{2TL}-\frac{1}{\omega^2 2C_\ell}+L_{3TL}} & \frac{2L_{1TL}(L_{3TL}+L_{2TL}-\frac{1}{\omega^2 2C_\ell})}{L_{1TL}+L_{2TL}-\frac{1}{\omega^2 2C_\ell}+L_{3TL}} \end{bmatrix} \\ \epsilon_z = \frac{C_{TL}}{d} g. \end{gathered} \tag{3.19}$$

From (3.19), it is clear that the material parameters (permeability) are dispersive. The form of the frequency dispersion is explicitly given by the expressions in (3.19). However, to be able to calculate the effective material parameters over a frequency range, the coefficients $(L_{1TL}, L_{2TL}, L_{3TL}, C_\ell)$ must be found. As will be shown in the following section, these coefficients can be found from eigenmode simulations.

3.4 Verification of the Homogenization Method

In this section, two examples are considered that validate the proposed homogenization procedure for both dispersive and non-dispersive tensor transmission-line

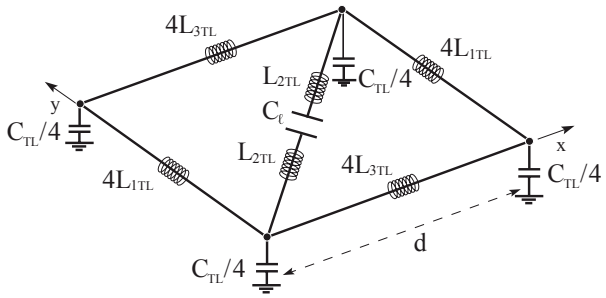

Figure 3.6: A circuit model of the capacitively loaded microstrip grid on diagonal branch.

metamaterial designs. In all the simulations that follow, the substrate is assumed to be lossless and to have a relative permittivity of $\epsilon_r = 3$, and height $h = 0.762$ mm. In addition, the unit cell dimension is assumed to be $d = 8.4$ mm, and the width of the lossless microstrip lines $w = 0.6$ mm.

3.4.1 Non-dispersive Material Parameters

First, let us consider the non-dispersive tensor transmission-line metamaterial from Fig. 3.1(a) with series loading elements

$$Z_{\ell 1} = j\omega L_{\ell 1} \qquad Z_{\ell 2} = j\omega L_{\ell 2} \qquad Z_{\ell 3} = j\omega L_{\ell 3} \tag{3.20}$$

where

$$L_{\ell 1} = 2 \text{ nH} \qquad L_{\ell 2} = 6 \text{ nH} \qquad L_{\ell 3} = 3 \text{ nH} \tag{3.21}$$

The metamaterial's circuit representation is shown in Fig. 3.5, and its non-dispersive material parameters are given by (3.17). Table 3.1 summarizes the results of eigenvalue simulations performed on such a unit cell using the commercial finite element electromagnetic solver, Ansys HFSS. The expressions $k_x d$ and $k_y d$ represent the phase delays across the unit cell in the x and y directions, and f denotes the eigenfrequencies.

$k_xd(deg)$	$k_yd(deg)$	$f(GHz)$	$Z_x(\Omega)$	$Z_y(\Omega)$
15	10	0.632	85.161	96.174
15	-10	0.481	97.308	-165.107
10	10	0.506	94.406	84.317
10	-10	0.379	131.682	-107.214
5	10	0.398	120.921	73.496
5	-10	0.320	387.885	-76.880
0	10	0.328	266.266	68.442
0	-10	0.328	-266.202	-68.435

Table 3.1: Eigenvalue simulation results of tensor TL metamaterial in Fig. 3.1(a) with loadings in (3.20).

The effective material parameters of the tensor transmission-line metamaterial are calculated using two independent simulation results (rows) from Table 3.1. Specifically, the material parameters are found using (3.11) and (3.12). The impedances Z_x and Z_y are calculated from the numerically computed E and H fields using (3.2) and (3.3). Using such a procedure, the effective material parameters are found to be

$$\bar{\bar{\mu}} = \begin{bmatrix} 6.591 & 1.980 \\ 1.980 & 7.650 \end{bmatrix} \mu_o, \qquad \epsilon_z = 1.510\epsilon_o. \tag{3.22}$$

For comparison purposes, a parallel-plate waveguide (see Fig. 3.1(b)) filled with a homogeneous medium with material parameters given by (3.22) was also simulated. The eigenvalue simulation results for the parallel-plate waveguide are summarized in Table 3.2.

The results of Table 3.1 and Table 3.2 show close agreement. Therefore, we can conclude that the effective material parameters accurately model the tensor transmission-line metamaterial. The dispersion curves for both the tensor transmission-line medium and its equivalent parallel-plate waveguide are compared in Fig. 3.7 at three different frequencies: 0.45, 0.65, and 0.85 GHz.

$k_x d(deg)$	$k_y d(deg)$	$f(GHz)$	$Z_x(\Omega)$	$Z_y(\Omega)$
15	10	0.631	85.205	95.211
15	-10	0.481	97.556	-164.827
10	10	0.505	94.405	84.027
10	-10	0.379	131.883	-107.260
5	10	0.397	120.733	73.721
5	-10	0.320	389.972	-77.039
0	10	0.327	264.944	68.575
0	-10	0.327	-264.944	-68.575

Table 3.2: Eigenvalue simulation results of parallel plate medium in Fig. 3.1(b) filled with homogenous medium with material parameters given by (3.22).

3.4.2 Dispersive Material Parameters

We will now find the effective material parameters of a frequency dispersive tensor TL metamaterial using the proposed homogenization method. Consider the tensor TL metamaterial depicted in Fig. 3.1(a) with series loading elements

$$Z_{\ell 1} = 0 \quad Z_{\ell 2} = \frac{1}{j\omega 2C_\ell} \quad Z_{\ell 3} = 0 \tag{3.23}$$

where

$$L_{1TL} = L_{3TL} \quad C_\ell = 20 \text{ pF}. \tag{3.24}$$

The circuit model of the metamaterial unit cell is depicted in Fig. 3.6. In the previous section, the effective material parameters of this metamaterial were shown to be frequency dispersive, and explicitly given by (3.19).

To find the effective material parameters at various frequencies in the homogeneous limit, we must determine the coefficients L_{1TL}, L_{2TL}, C_{TL} and C_ℓ in (3.19) using the proposed homogenization procedure. Eigenmode simulations of the unit cell in Fig. 3.1(a) with loadings given by (3.23) were performed using Ansys HFSS and are summarized in Table 3.3. It should be noted that each eigenmode simulation results

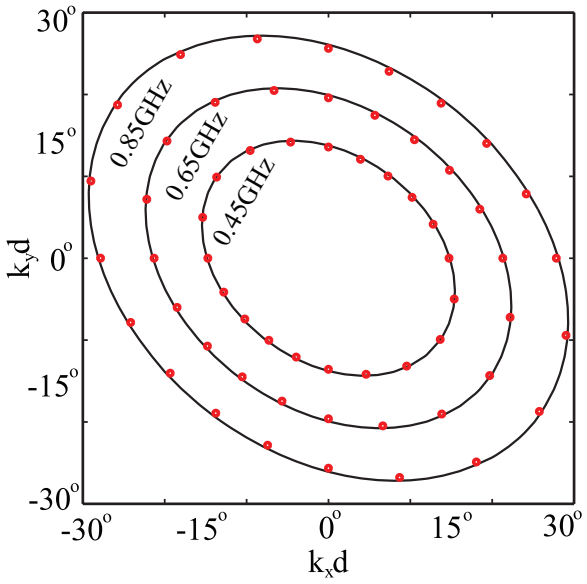

Figure 3.7: Dispersion curves for the tensor TL metamaterial shown in Fig. 3.1(a) with loadings given by (3.20) (solid lines), and the parallel-plate waveguide shown in Fig. 3.1(b) filled with a homogenous medium with material parameters given by (3.22) (dots). Comparison is made at three different frequencies: 0.45, 0.65, and 0.85 GHz.

in two eigenfrequency solutions for a given set of $(k_x d, k_y d)$. This was an expected result as the order of metamaterial's dispersion equation with respect to frequency is four due to the capacitive loading.

Using the results of the two eigenmode simulations along with (3.11), (3.12) and (3.19), the coefficients (electrical parameters) $L_{1TL} = L_{3TL}$, L_{2TL}, C_{TL} and C_ℓ were computed from the effective material parameter expressions using (3.19).

$$L_{1TL} = L_{3TL} = 1.845\text{nH} \quad L_{2TL} = 4.325\text{nH} \quad C_\ell = 12.225\text{pF} \quad C_{TL} = 1.240\text{pF} \tag{3.25}$$

Once again, a parallel-plate waveguide filled with a homogeneous medium with material parameters given by (3.19) and (3.25) was simulated. The eigenvalue simulation results for the parallel-plate waveguide are given in Table 3.4 and show close agreement with those in Table 3.3 for the tensor transmission-line metamaterial, confirming the accuracy of the frequency-dependent effective material parameters.

$k_xd(deg)$	$k_yd(deg)$	$f(GHz)$	$Z_x(\Omega)$	$Z_y(\Omega)$
15	0	0.378	89.218	-53.617
15	0	0.796	42.336	105.073
20	0	0.394	114.061	-33.879
20	0	1.017	44.323	126.645
20	5	0.368	79.050	-55.561
20	5	1.117	45.929	84.534
20	10	0.355	81.217	-113.492
20	10	1.253	48.940	68.830
20	15	0.351	110.708	-592.978
20	15	1.416	52.804	61.268

Table 3.3: Eigenvalue simulation results of capacitively loaded unit cell in Fig. 3.1(a) with loadings (3.23).

$k_xd(deg)$	$k_yd(deg)$	$f(GHz)$	$Z_x(\Omega)$	$Z_y(\Omega)$
15	0	0.376	89.422	-53.138
15	0	0.800	42.049	103.368
20	0	0.380	118.016	-32.132
20	0	1.025	43.778	122.627
20	5	0.366	78.769	-55.139
20	5	1.129	45.185	82.430
20	10	0.357	81.082	-114.140
20	10	1.269	48.016	67.145
20	15	0.348	110.294	-573.180
20	15	1.435	51.565	59.633

Table 3.4: Eigenvalue simulation results of parallel plate medium in Fig. 3.1(b) filled with homogenous medium with material parameters given by (3.19) and (3.25).

The effective material parameters computed using (3.19) and (3.25) are plotted in Fig. 3.8 (solid lines) with respect to frequency. Plotted on the same graph, are the effective material parameters (dots) found directly using (3.11) and (3.12) at individual frequencies. The material parameters for this particular tensor transmission-line metamaterial could be extracted at a single eigenfrequency since there are only three unknowns ($\mu_{xx} = \mu_{yy}, \mu_{xy} = \mu_{yx}, \epsilon_z$) and three equations are provided by (3.11) and (3.12). This close agreement demonstrates that the frequency dependent homogenization procedure can be used to predict effective material parameters of dispersive

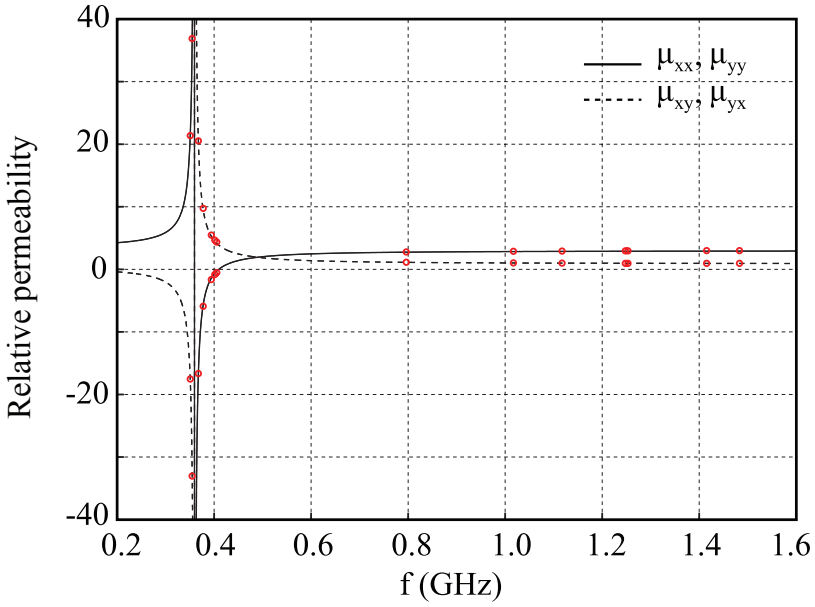

Figure 3.8: Effective material parameter variation with respect to frequency. The figure compares the predicted values (solid line) to the full wave simulation results (dots).

tensor transmission-line metamaterials at various frequencies within the homogeneous limit.

Finally, the analytical dispersion contours for the tensor transmission-line medium and its equivalent parallel-plate waveguide are compared in Fig. 3.9. Specifically, the figure compares the dispersion contours for the parallel-plate waveguide filled with material parameters given by the solid lines in Fig. 3.8 and a tensor transmission-line medium possessing material parameters given by the dots in Fig. 3.8 at three different frequencies: 0.35, 0.37, and 1.25 GHz.

3.5 Conclusions

This chapter presented a rigorous homogenization method for finding the effective material parameters (tensorial permeability and a scalar permittivity) of tensor transmission-line metamaterials. The method utilized a local field averaging procedure over the faces of the realized metamaterial's unit cell to compute its effec-

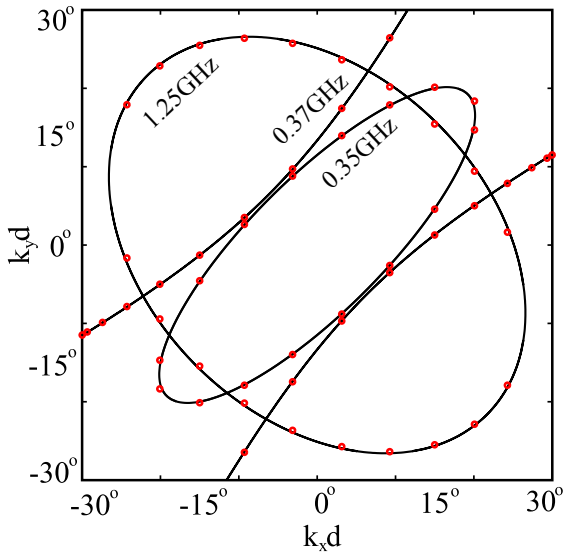

Figure 3.9: Dispersion curves for the tensor TL metamaterial shown in Fig. 3.1(a) with loadings given by (3.23) (solid lines), and the parallel-plate waveguide shown in Fig. 3.1(b) filled with a homogenous medium with material parameters given by (3.19) and (3.25) (dots). Comparison is made at three different frequencies: 0.35, 0.37, and 1.25 GHz.

tive material parameters. In addition, the effective material parameters of tensor transmission-line metamaterials were expressed in terms of their circuit parameters. This allowed the material parameters of frequency dispersive tensor transmission-line metamaterials to be predicted over a range of frequencies within the homogeneous limit. The proposed homogenization method was applied to microstrip implementations of tensor transmission-line metamaterials. Tensor transmission-line metamaterials possessing dispersive and non-dispersive material parameters were considered. The homogenization method was verified through full-wave simulations and shown to successfully compute effective material parameters.

The proposed homogenization method provides an accurate and rapid characterization of tensor transmission-line metamaterials in terms of effective material parameters. The method can account for couplings within the realized tensor transmission-line unit cell, which cannot be captured by the proposed circuit model in the previous chapter. Furthermore, the method takes advantage of the commercial full-wave simu-

lator, Ansys HFSS, which allows to use scripts for automating of the homogenization process. Using scripts, the field integrations and arithmetic operations on the integration results can be computed for sets of prescribed phase delays, and the results can be exported to a computing software, such as MATLAB, for further processing. The incorporation of automation process in the homogenization procedure is prominent when designing practical devices consisting of numerous unit cells.

CHAPTER IV

Experimental Verification of Tensor TL Metamaterials

Up to this point, analytical and simulation results for tensor transmission-line metamaterials have been presented in this thesis. In Chapter 2, tensor transmission-line metamaterials were modeled analytically, and their propagation characteristics were verified through full wave simulations. It was shown that tensor transmission-line metamaterials are circuit networks that are equivalent to magnetically anisotropic, homogeneous media. Apart from the initial circuit model, various other circuit topologies that possess anisotropic electromagnetic properties have also been proposed. The variety of circuit models provides designers with added flexibility when tailoring the effective material parameters for specific applications. Subsequently, two transformation electromagnetics devices, a cylindrical cloak and a field rotator, were designed using tensor transmission-line metamaterials and studied in simulation. In Chapter 3, a homogenization technique to accurately calculate the effective material parameters of tensor transmission-line metamaterials was proposed and verified through simulations. With the homogenization method, it is now possible to characterize the effective material parameters of a realized tensor transmission-line metamaterials using full wave simulations in a rapid and accurate manner.

This chapter confirms the theory of tensor transmission-line metamaterials through

experiment. To this end, tensor transmission-line metamaterials are utilized in the design and implementation of a beam-shifting slab: a transformation electromagnetics device consisting of isotropic and anisotropic media. The design process combines the tools developed for designing tensor transmission-line metamaterials: analytical methods, full-wave simulations, and homogenization method for effective material parameter extraction.

The next section reviews the design and operation of the beam-shifting slab. The coordinate transformations and isotropic and anisotropic material parameters required for the implementation are shown. Subsequent sections detail the design of tensor transmission-line metamaterial unit cells realizing the required material parameters. The electromagnetic behavior of the designed beam-shifting slab is corroborated through circuit simulation, full-wave simulation of an equivalent slab with homogenized material parameters corresponding to the metamaterials employed, and experiment. Toward the end of the chapter, the wide-band frequency response of the slab is analyzed in simulation and experiment.

4.1 The Beam Shifting Slab

Beam-shifting slabs are reflectionless devices that laterally displace the electromagnetic field transmitted through them [92, 93, 94]. The slab presented in this chapter is used to laterally displace a cylindrical wave incident upon it. In others words, to an observer on the far side of the slab (opposite the source), it appears as though the source of the cylindrical wave is shifted along the slab interface. This electromagnetic phenomenon is illustrated in Fig. 4.1 and Fig. 4.2. In Fig. 4.1, the phase of the vertical electric field radiating from a cylindrical source is shown in the presence of a beam-shifting slab. The interfaces of the slab are denoted by thick vertical lines. On the far side of the slab, phase fronts of the cylindrical source appear as if they originate from a hypothetical source located above the actual one. This same

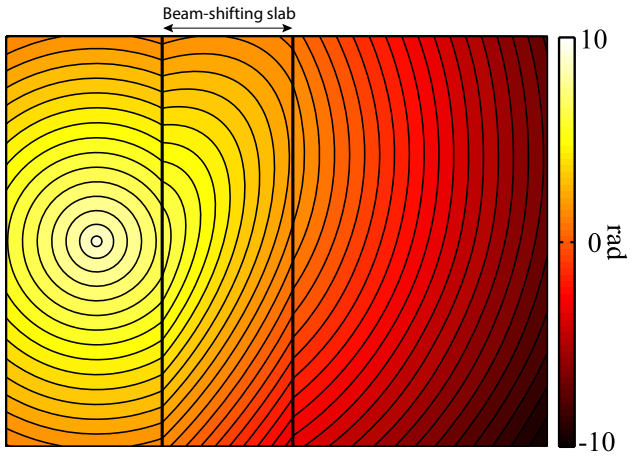

Figure 4.1: Vertical electric field phase distribution for a cylindrical source in the presence of a beam-shifting slab. On the far side of the slab, the radiating point source appears as if laterally displaced. The boundaries of the slab are shown with a solid line.

phenomenon is depicted in Fig. 4.2, where the concentric circles (solid and dashed) represent the phase fronts of two displaced cylindrical sources. On the far side of the structure, the dashed circles are the observed wave, while the actual source radiates from the center of the solid circles.

The beam-shifting slab is a transformation electromagnetics device, so its operation can be represented by a coordinate transformation. The coordinate transformation between the primed transformed coordinates (x', y', z') and unprimed original coordinates (x, y, z) representing the lateral displacement of the field within the slab can be written as:

$$x' = x, \qquad y' = \begin{cases} y, & y < 0 \\ y + bx, & 0 \leq y \leq d \\ y + bd, & d < y \end{cases}, \qquad z' = z, \tag{4.1}$$

where the slab exists between $x = 0$ and $x = d$.

A two dimensional visualization of the coordinate transformation, given by (4.1), can be obtained by plotting the coordinates of the transformed points $(x^{'}, y^{'})$ on

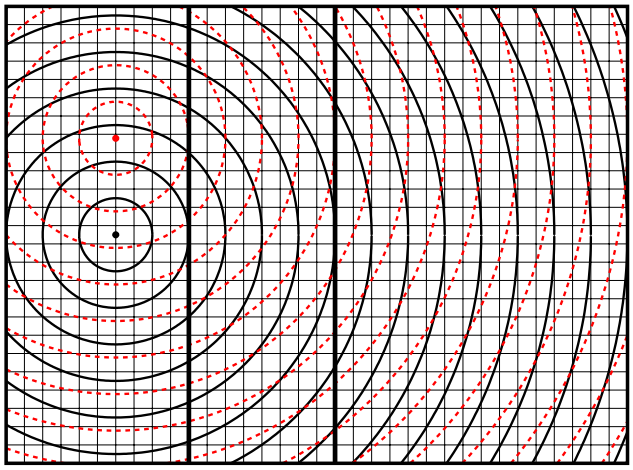

Figure 4.2: Phase fronts of original point source (solid circles) and shifted point source (dashed circles). The center of the dashed circles is laterally 5.28 unit cells above the center of solid circles.

the $x-y$ plane. A set of specific points belonging to coordinate lines (curves) in the $x-y$ plane were selected for the visualization. For example, Fig. 4.3(a) shows lines of constant x and lines of constant y plotted on the $x-y$ plane in red and blue, respectively. The red and blue lines were transformed through the coordinate transformation (4.1) and resulted in the lines shown in Fig. 4.3(b). In a similar manner, Fig. 4.4(a) and Fig. 4.4(b) show the transformation of a different set of points such as curves of constant r (red) and lines of constant θ (blue) originating from the cylindrical source position. These plots allow one to visualize the behaviour of the designed device under different excitations. In fact, Fig. 4.3(b) and Fig. 4.4(b) show the effect of the beam-shifting region under a plane wave excitation propagating along x direction and a cylindrical source excitation located at the center of red circles, respectively. Lateral displacement is obvious for both excitations.

To realize the beam-shifting effect, the material parameters (permittivity and permeability) of the slab are calculated using the coordinate transformation given by

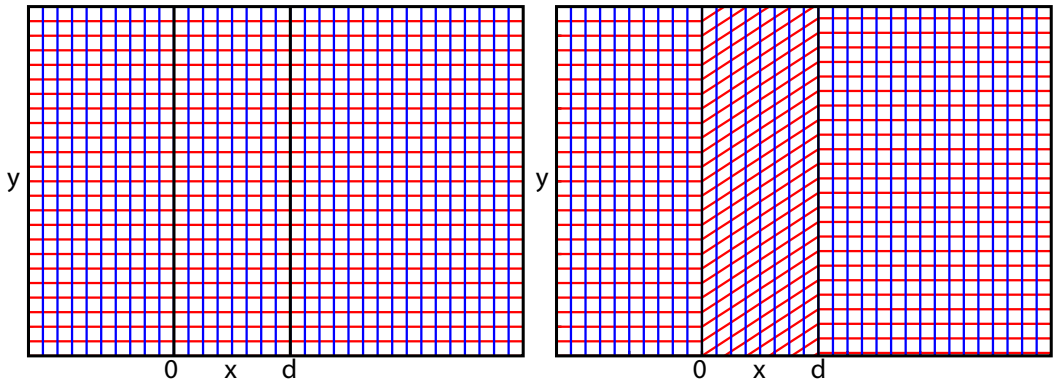

(a) Original (b) Transformed

Figure 4.3: The visualization of the coordinate transformations in (4.1). (a) The lines of constant x and constant y are shown in red an blue color, respectively. (b) The transformation of the red and blue lines under the given transformation in (4.1).

(4.1) and are of the following form [92, 93, 94]:

$$\epsilon_z = \epsilon_o, \qquad \mu = \begin{bmatrix} 1 & b \\ b & 1+b^2 \end{bmatrix} \mu_o, \tag{4.2}$$

where b is a real number related to the amount of lateral displacement. Specifically, the lateral displacement amount is equal to b times the slab thickness [94]. The positive and negative values correspond to upward and downward shifts of the electromagnetic field, respectively. The material parameters given by (4.2) assume that the medium outside the slab is free space with material parameters

$$\epsilon_z = \epsilon_o, \qquad \mu = \mu_o. \tag{4.3}$$

The form of the medium parameters comprising the beam-shifting slab (see Eq. 4.2) is common to other transformation electromagnetics devices such as beam dividers [93], embedded-recessed line source [95], field rotators [70, 96], and invisible slab cloaks [97]. This widespread use of anisotropic material parameters of the form given by Eq. (4.2) motivated the implementation of a beam-shifting slab using tensor transmission-line

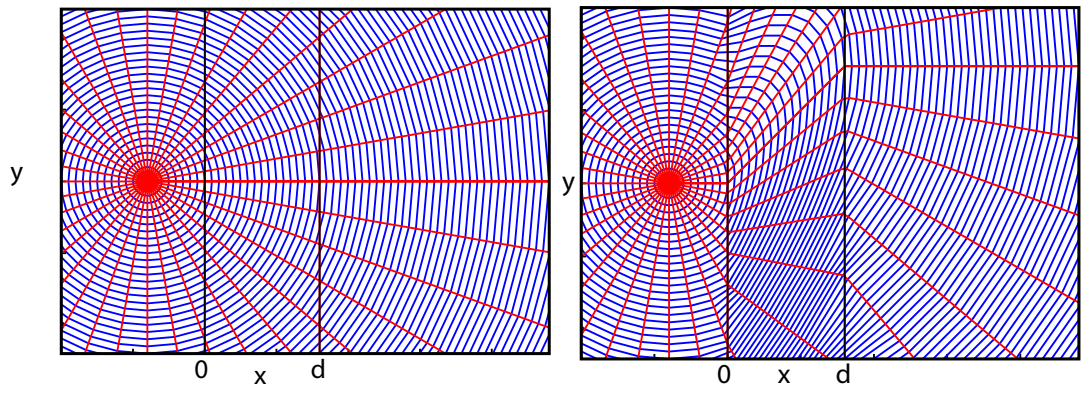

(a) Original (b) Transformed

Figure 4.4: The visualization of the coordinate transformations in (4.1). (a) The lines of constant θ and the curves of constant r are shown in red and blue, respectively. (b) The transformation of the red lines and blue curves under the given transformation in (4.1).

metamaterials.

4.2 Design of Beam-Shifting Slab and Surrounding Medium

As shown in previous section, the realization of a beam-shifting slab requires the design of two homogenous media: the slab with effective material parameters of the form given by (4.2), and the surrounding medium with isotropic material parameters given by (4.3). This section describes the design of these two media using tensor transmission-line metamaterials implemented in microstrip technology. The designs were implemented on a low loss ($\tan\delta = 0.0013$), grounded microwave substrate (Rogers RO3003) of thickness 0.762 mm (30 mil), dielectric constant $\epsilon_r = 3.00$ and metallization thickness of $17\mu m$. The design frequency was chosen to be 1.0 GHz for a practical size and implementation of a beam-shifting device.

Fig. 4.5 and Fig. 4.6 show unit cell topologies for the transmission-line metamaterials as well as their dimensions. The unit cell depicted in Fig. 4.5 was used to design the surrounding isotropic medium. The anisotropic unit cell of Fig. 4.6 was used for the beam-shifting slab.

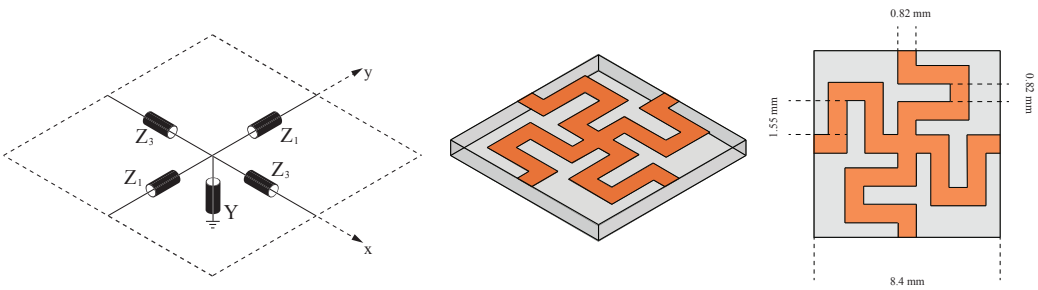

(a) Circuit schematic. (b) Printed-circuit layout

Figure 4.5: (a) Circuit schematic and (b) printed-circuit layout of the isotropic unit cell. The effective material parameters of the isotropic, homogeneous periodic medium consisting of such unit cells are $\epsilon_z = 2.205\epsilon_o$ and $\mu = 5.00\mu_o$.

$k_x d(deg)$	$k_y d(deg)$	$f(GHz)$	$Z_x(\Omega)$	$Z_y(\Omega)$
10	0	0.299	51.896	∞
20	10	0.421	72.658	72.658

Table 4.1: Eigenvalue simulation results of tensor transmission-line metamaterial in Fig. 4.5.

The effective material parameters of the metamaterial unit cells were found using the homogenization method outlined in Chapter 3. The eigenmode simulation results for the isotropic unit cell shown in Fig. 4.5 are given in Table 4.2. By applying the homogenization procedure to these quantities, the effective material parameters were calculated to be

$$\epsilon_z = 2.205\epsilon_o, \qquad \mu = 5.00 \begin{bmatrix} 1.00 & 0.00 \\ 0.00 & 1.00 \end{bmatrix} \mu_o. \tag{4.4}$$

The electrical size of the isotropic unit cell is one sixth of a guided wavelength at the design frequency. This is adequately small for the metamaterial to behave as a homogenous medium with the effective material parameters given by (4.4).

Given that material parameters of the isotropic medium given by (4.4), the slab's

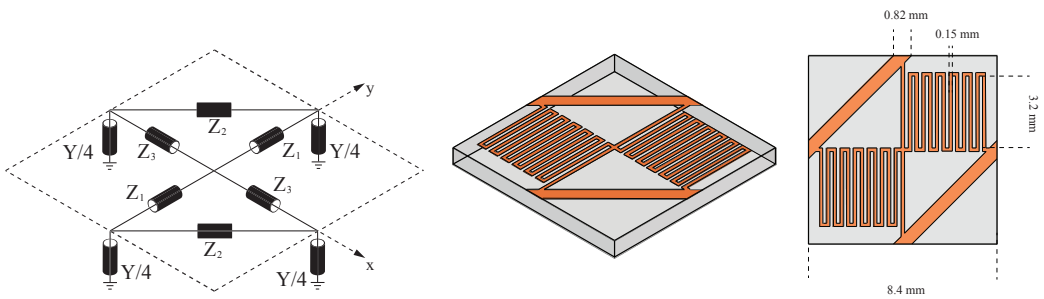

(a) Circuit schematic. (b) Printed-circuit layout.

Figure 4.6: (a) Circuit schematic and (b) printed-circuit layout of the anisotropic unit cell. The effective material parameters of the anisotropic, homogeneous periodic medium consisting of such unit cells are $\epsilon_z = 2.215\epsilon_o$ and $\mu_{xx} = 4.90 \times 1\mu_o$, $\mu_{xy} = \mu_{yx} = 4.90 \times 0.66\mu_o$, $\mu_{yy} = 4.90 \times 1.45\mu_o$.

anisotropic effective material parameters must be of the following form

$$\epsilon_z = 2.205\epsilon_o, \qquad \mu = 5.00 \begin{bmatrix} 1.00 & b \\ b & 1+b^2 \end{bmatrix} \mu_o, \tag{4.5}$$

where b is a real number representing the amount of lateral displacement provided by the slab. For this design, $b = 0.66$, which corresponds to a lateral shift of 5.28 unit cell lengths in an upward direction for a beam-shifting slab that is eight unit cells-thick.

The topology of the anisotropic unit cell is depicted in Fig. 4.6. To calculate its homogenized material parameters, the eigenmode simulation results shown in Table 4.2 were used.

$k_x d(deg)$	$k_y d(deg)$	$f(GHz)$	$Z_x(\Omega)$	$Z_y(\Omega)$
-20	12.5	0.521	-74.678	183.271
10	20	0.920	68.325	43.953

Table 4.2: Eigenvalue simulation results of tensor transmission-line metamaterial in Fig. 4.6.

From the tabulated data, its effective material parameters were calculated to be

$$\epsilon_z = 2.215\epsilon_o, \qquad \mu = 4.90 \begin{bmatrix} 1.00 & 0.66 \\ 0.66 & 1.45 \end{bmatrix} \mu_o. \tag{4.6}$$

These effective material parameters are very close to the desired parameters given by (4.5). Note that the effective permittivity (ϵ_z) values of the slab and surrounding isotropic medium were designed to be identical, as required by (4.2) and (4.3). This resulted in an impedance match between the surrounding isotropic medium and the anisotropic slab for all angles of incidence, rendering the slab reflectionless.

4.3 Simulation and Experiment at the Design Frequency

This section presents the simulated and experimental performance of the designed beam-shifting slab. Fig. 4.7 shows the simulation and experimental set-up. In the schematic, each square represents a transmission-line metamaterial unit cell. To highlight the operation of the beam-shifting slab, two separate structures were studied. In the first structure, all the squares in the setup (both light and dark in color) were isotropic unit cells. Therefore, the test structure was homogenous and isotropic, and supported a cylindrical field emanating from the source. The second structure incorporated the beam-shifting slab. The slab consisted of 8×25 anisotropic unit cells (shown darker in color in Fig. 4.7). It was sandwiched between two isotropic media, consisting of 10×25 and 16×25 isotropic unit cells (lighter in color). This structure was used to experimentally demonstrate how a reflectionless beam-shifting slab can laterally displace the field of a cylindrical source.

The cylindrical source, common to both structures, was centered with respect to the transverse direction, and located 6 unit cells away from the leftmost edge of the test set-up. The outer boundaries of the test set-up were terminated with matched

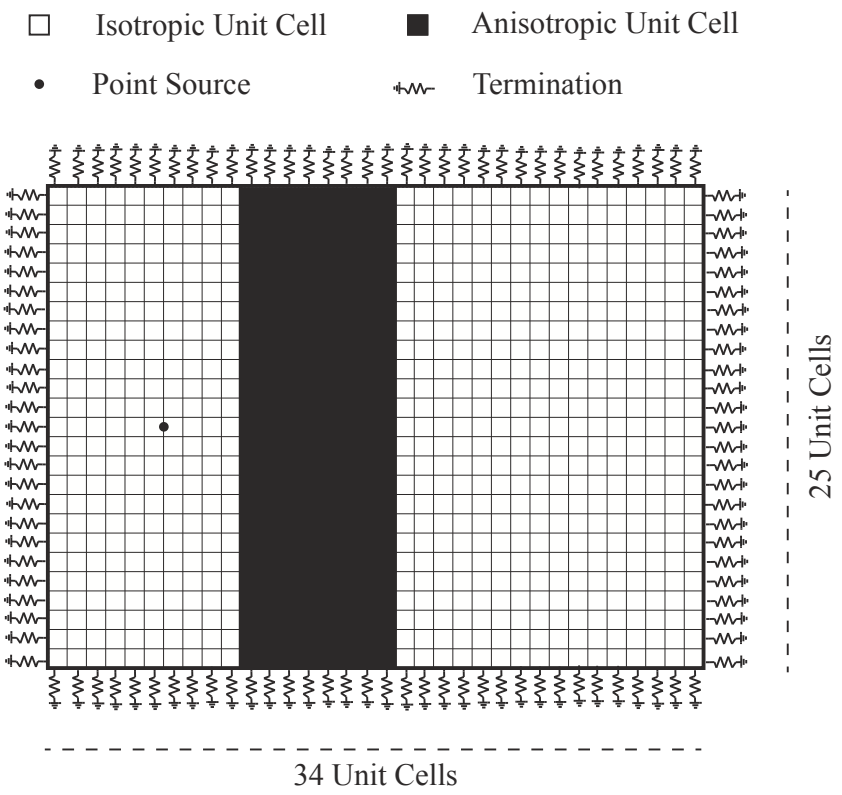

Figure 4.7: Simulation and experimental set-up for the transmission-line based beam-shifting slab. The anisotropic slab, consisting of 8×25 unit cells (shown darker in color), is sandwiched between two isotropic media, consisting of (10×25 and 16×25) unit cells (shown lighter in color). The point source excitation is denoted with a black dot. The outer boundaries of the set-up are terminated with matched impedances.

impedances in order to eliminate reflections. These impedances were calculated using full-wave simulation results of the homogenized structure. First, the simulation was used to calculate field values at the boundary of simulation domain. Then, the wave impedances normal to the boundaries were calculated. This was accomplished by calculating the ratio of tangential electric field, E_z, to tangential magnetic field, H_x or H_y, at the boundary. Finally, the circuit impedances (terminations) were calculated by multiplying the wave impedances by the height to width ratio of the unit cells. Commercially available 0603 package resistors were used for the resistive part of the terminations. The reactive parts of the terminations were neglected, since they were

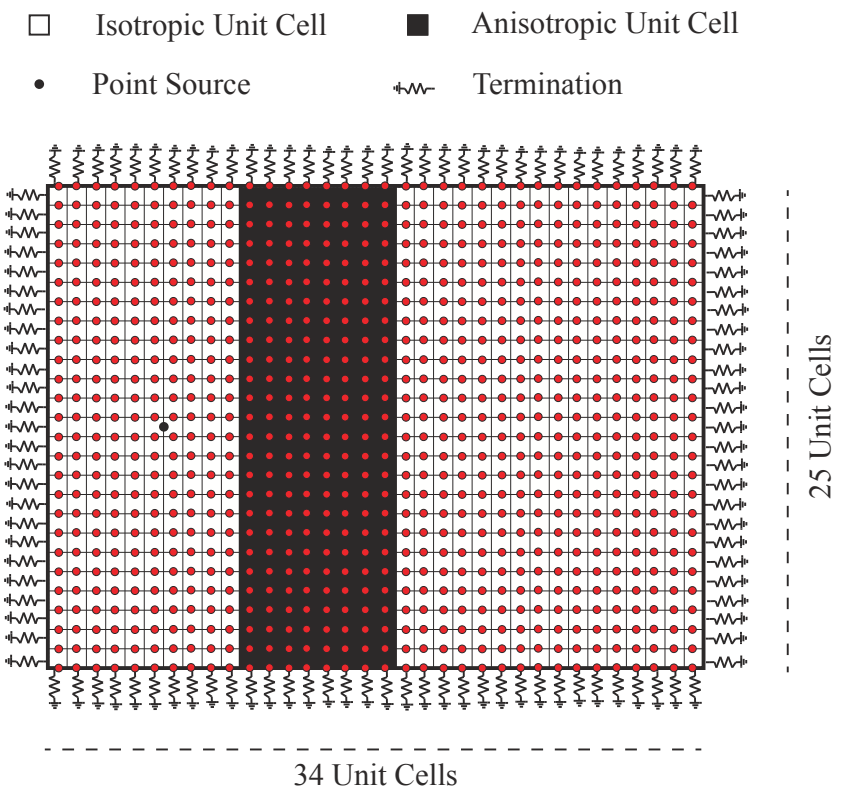

Figure 4.8: Interconnecting nodes. Data points for simulation and measurement results are collected from the dotted positions.

generally much lower than the real parts.

Simulation and measurement results are presented as contour plots of the node voltages between unit cells. The node positions are identified with dots in Fig. 4.8.

4.3.1 Simulations

Simulations were performed using a combination of full-wave electromagnetic computation and circuit analysis. In the circuit simulations of the overall structures, the unit cells of Fig. 4.7 were replaced with the respective four-port S-parameter files of the designed unit cells depicted in Fig. 4.5 and Fig. 4.6. Agilent's Advanced Design System (ADS) was used for the circuit simulations. The S parameters of the unit cells were computed using Agilent's Momentum full-wave electromagnetic simulator.

For the first case, where the structure consists of only isotropic unit cells, a contour

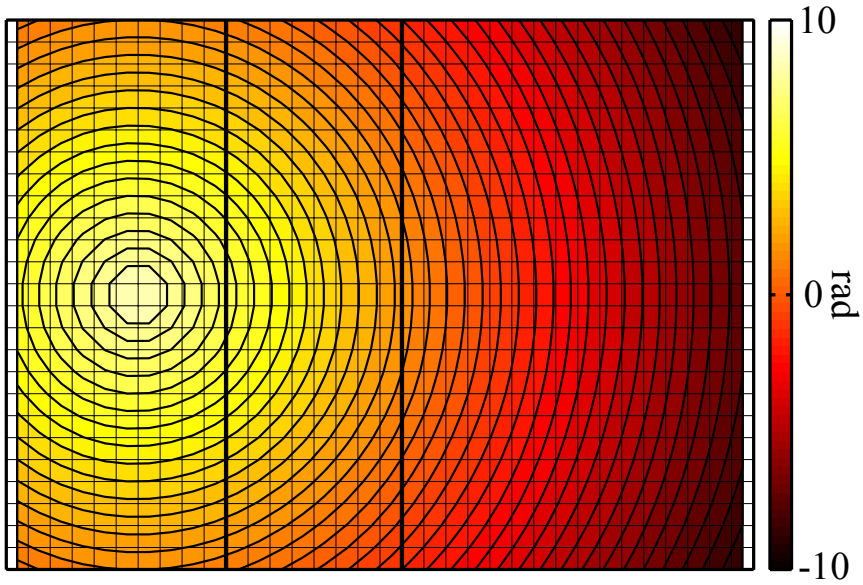

Figure 4.9: A contour plot of the simulated voltage phase at the interconnecting nodes (see Fig. 4.8) of the simulated isotropic medium. The simulation frequency is 1.0 GHz.

plot of simulated voltage phases at the nodes is plotted in Fig. 4.9. A cylindrical wave emanating from the source can be clearly observed at the design frequency of 1.0 GHz.

For the second case, where the beam-shifting slab is sandwiched between two isotropic structures, a contour plot of the simulated voltage phases at the nodes is plotted in Fig. 4.10. The simulated operation of the slab is as expected. The field is shifted laterally by the slab.

4.3.2 Experiments

The experimental structure is shown in Fig. 4.11. Both experimental structures were excited by a coaxial (SMA) connector through the microstrip ground plane. The center conductor of the SMA connector was attached to the microstrip grid of an isotropic unit cell, while the outer conductor of the connector was attached to the ground plane just below. The vertical electric field was probed 1.5 mm above the entire surface of the structure, using a short coaxial probe with an extended center

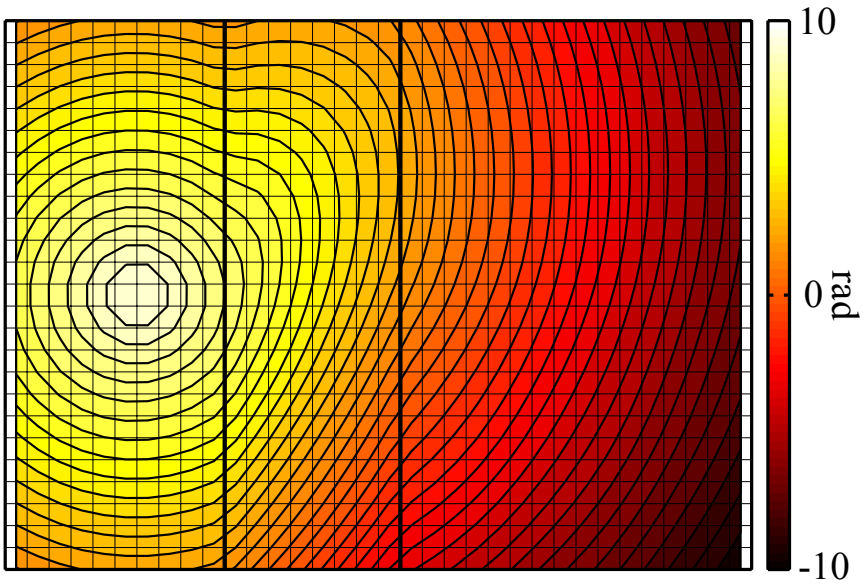

Figure 4.10: A contour plot of the simulated voltage phase at the interconnecting nodes (see Fig. 4.8) of the simulated beam-shifting slab. The simulation frequency is 1.0 GHz.

conductor. Port 1 of a network analyzer was connected to the coaxial connector and port 2 was connected to the probe, which was scanned above the surface of the structure using a two dimensional translation stage. The measured transmission coefficient, S_{21}, is proportional to the voltage of the nodes with respect to the ground plane. Fig. 4.12 shows the experimental structure for the first case, which entirely consists of the isotropic unit cells shown in Fig. 4.5. Fig. 4.13 shows a contour plot of the phase of the measured vertical electric field above the nodes of the unit cells (see Fig. 4.8) at 1.0 GHz. It is clear that the measurement results for the isotropic structure (Fig. 4.13) closely agree with simulation (Fig. 4.9).

Fig. 4.14 shows the experimental structure for the second case, where the beam-shifting slab is present. A contour plot of the phase of the measured vertical electric field above each node is shown in Fig. 4.15 at 1.0 GHz. Once again, excellent agreement is observed with the simulated node voltages shown in Fig. 4.10. In addition to the phase response of the experimental slab, a time snapshot of the vertical electric field is shown in Fig. 4.16. It confirms that the slab is in fact reflectionless.

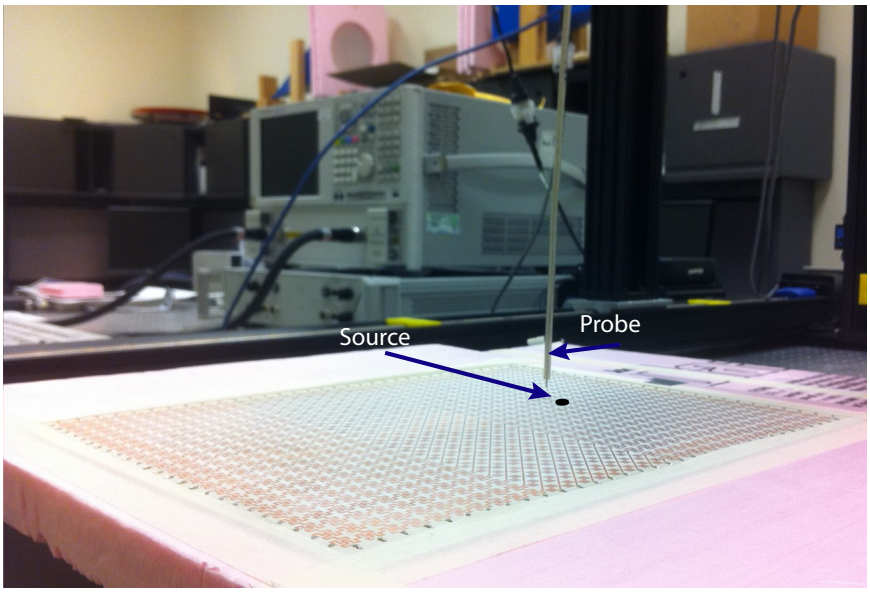

Figure 4.11: The experimental setup. An experimental structure, source position and coaxial probe with an extended center conductor are shown.

4.4 Bandwidth

The successful operation of the beam-shifting slab was demonstrated at a design frequency of 1 GHz. However, the designed device promises a wide bandwidth of operation due to the traveling-wave nature of tensor transmission-line metamaterials and non-dispersive unit cells utilized in this specific design. As discussed in Chapter 4, the unit cell is non-dispersive (as long as electrically small) when all the series loadings in the tensor transmission-line unit cell are inductive. This is clearly the case for the unit cells used in the beam shifting slab, as shown in Fig. 4.5(b) and Fig. 4.6(b). To verify the wide bandwidth of operation, the frequency response of the designed beam-shifting slab was studied in simulation and experiment.

4.4.1 Bandwidth Prediction from Simulations

The bandwidth of operation of the beam-shifting slab can be predicted by studying the dispersion characteristics of the anisotropic transmission-line metamaterial used in its design. The dispersion surface of the designed anisotropic unit cell (see Fig. 4.6)

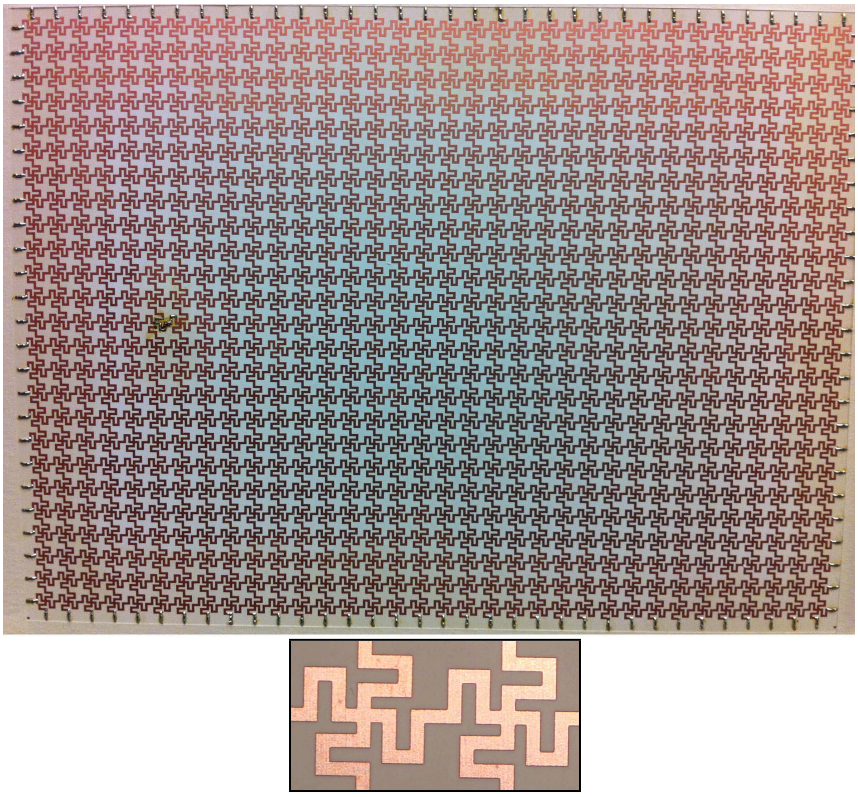

Figure 4.12: The experimental structure consisting of only isotropic unit cells fabricated using standard PCB technology. Two connected isotropic unit cells are shown in the inset.

comprising the beam-shifting slab is plotted in Fig. 4.17. The solid curves plotted on the horizontal plane show the isofrequency dispersion contours at four different frequencies: 1, 2, 3 and 3.5 GHz. In the same figure, the isofrequency dispersion contours of the homogenous medium with material parameters in (4.6) are plotted with circles. As observed in Fig. 4.17, the isofrequency dispersion contours of the transmission-line metamaterial and the homogenous medium essentially overlap up to 3.0 GHz. Above this frequency, they differ significantly due to the spatial dispersion of the transmission-line metamaterial.

In conclusion, the designed beam former is expected to perform reasonably well up around to 3.0 GHz. In the following part, this prediction is verified by through measurements.

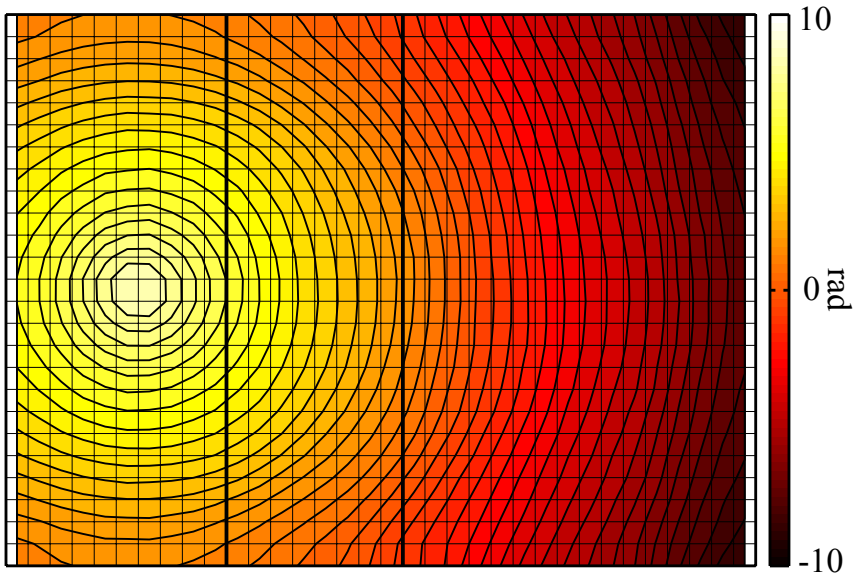

Figure 4.13: A contour plot of the measured vertical electric field phase at the interconnecting nodes (see Fig. 4.8) of the experimental structure in Fig. 4.12. The measurement frequency is 1.0 GHz.

4.4.2 Experimental Verification of Predicted Bandwidth

Fig. 4.18 and Fig. 4.19 show the phase of the measured vertical electric field above each unit cell in the experimental structure (see Fig. 4.14) at two disparate frequencies: 0.8 GHz and 1.2 GHz, respectively. As can be seen, the slab maintains its beam-shifting and reflectionless properties at both frequencies. As for frequencies far from the design frequency, Fig. 4.20 and Fig. 4.21 show the phase and time snapshot of the vertical electric field above each unit cell in the experimental structure at 2.0 GHz and 3.0 GHz, respectively. The beam-shifting properties are still apparent despite the degraded performance at 3.0 GHz due to spatial dispersion within the transmission-line metamaterials. Such a performance verifies the bandwidth predictions of the previous section based on full-wave simulation.

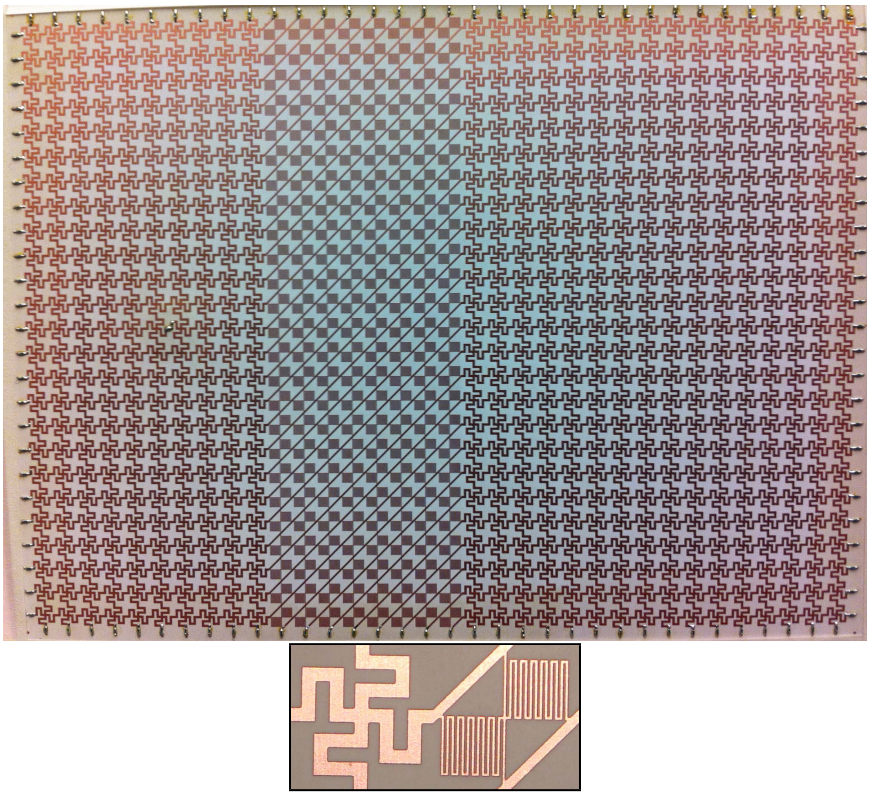

Figure 4.14: The experimental structure with a beam-shifting slab fabricated using standard PCB technology. Two connected isotropic and anisotropic unit cells are shown in the inset.

4.5 Conclusion

In this chapter, a transformation electromagnetic device, a beam-shifting slab, was implemented using tensor transmission-line metamaterials. It was studied in simulation and experiment. Simulation and experimental results demonstrated that radiation from a cylindrical source is shifted upward by 5.28 unit cells due to the presence of the beam-shifting slab. The design of the unit cells forming the anisotropic slab and surrounding isotropic medium was reviewed. The experimental performance of the designed slab was compared to its simulated performance, and excellent agreement was observed. Moreover, the frequency dependence of the device was studied in both simulation and experiment. A reasonable performance from the design frequency of 1 GHz up to 3 GHz has been demonstrated, and a wide bandwidth of

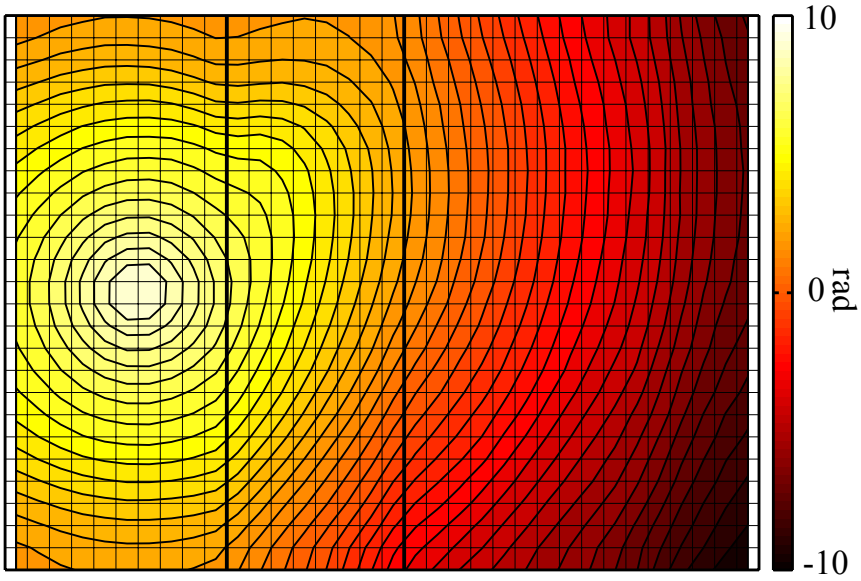

Figure 4.15: A contour plot of the measured vertical electric field phase at the interconnecting nodes (see Fig. 4.8) of the experimental structure in Fig. 4.14. The measurement frequency is 1.0 GHz.

operation confirmed.

Most importantly, this work experimentally verified the anisotropic behavior of tensor transmission-line metamaterials as well as the homogenization procedure used to extract their material parameters. Further, it experimentally demonstrated the suitability of using tensor metamaterials to design transformation electromagnetics devices. Now that the theory behind tensor transmission-line metamaterials has been verified through simulation and experiment, these metamaterials can be used to implement larger and more complex devices that are both anisotropic, inhomogeneous.

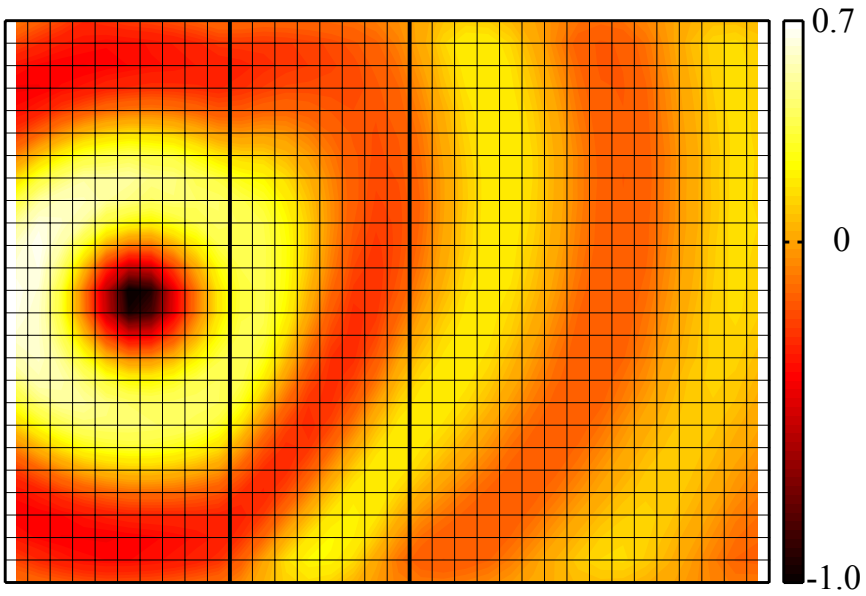

Figure 4.16: Time snapshot of the measured, steady state vertical electric field at the interconnecting nodes (see Fig. 4.8) of the experimental structure in Fig. 4.14. The measurement frequency is 1.0 GHz. The plot is normalized with respect to the maximum value of the plotted data.

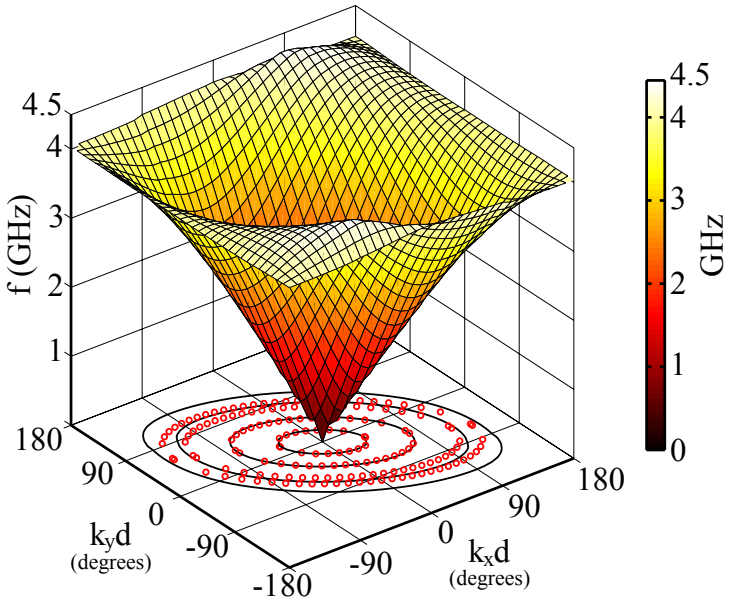

Figure 4.17: The dispersion surface of the anisotropic unit cell shown in Fig. 4.6. The solid curves plotted on the horizontal plane show the isofrequency dispersion contours for the anisotropic transmission-line metamaterial at four different frequencies: 1, 2, 3 and 3.5 GHz. The isofrequency dispersion contours of the equivalent homogenous medium with material parameters given by (4.6) are plotted with circles.

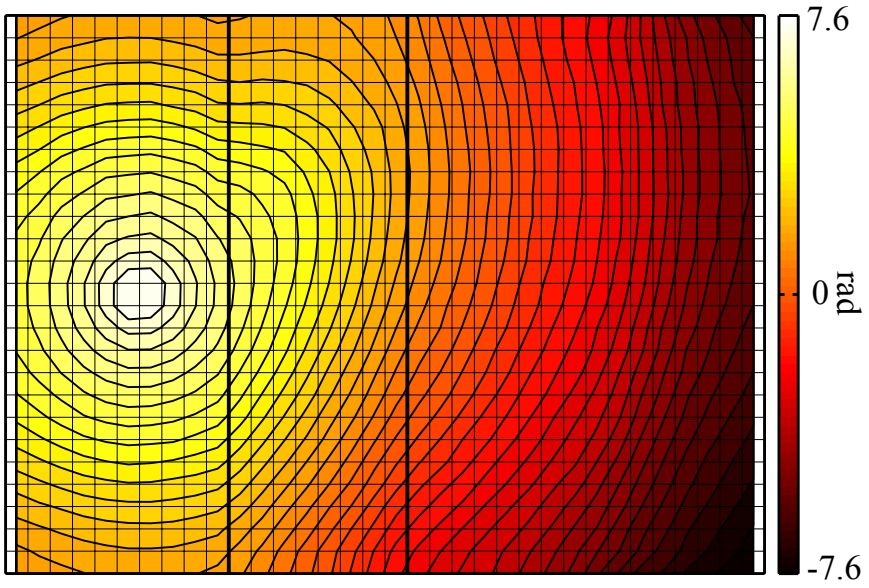

Figure 4.18: A contour plot of the measured vertical electric field phase at the interconnecting nodes (see Fig. 4.8) of the experimental structure in Fig. 4.12. The measurement frequency is 0.8 GHz.

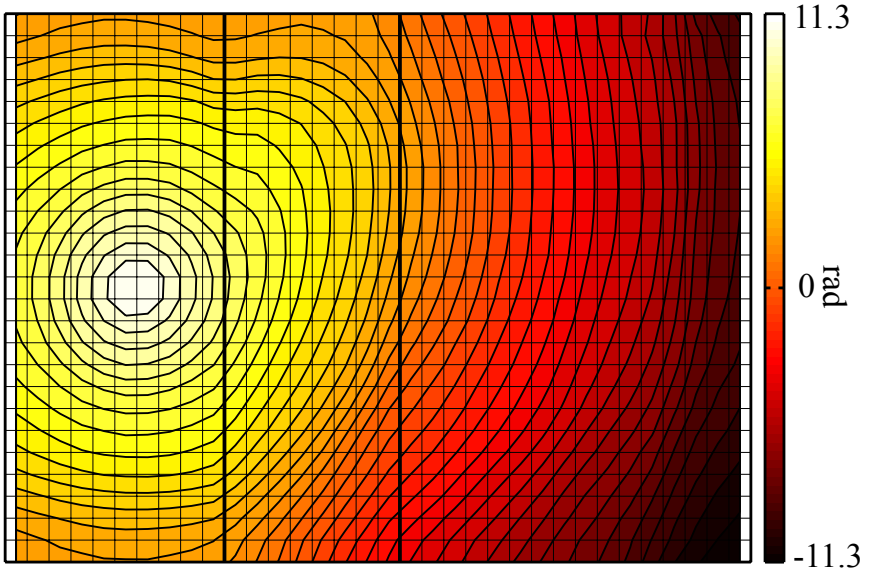

Figure 4.19: A contour plot of the measured vertical electric field phase at the interconnecting nodes (see Fig. 4.8) of the experimental structure in Fig. 4.12. The measurement frequency is 1.2 GHz.

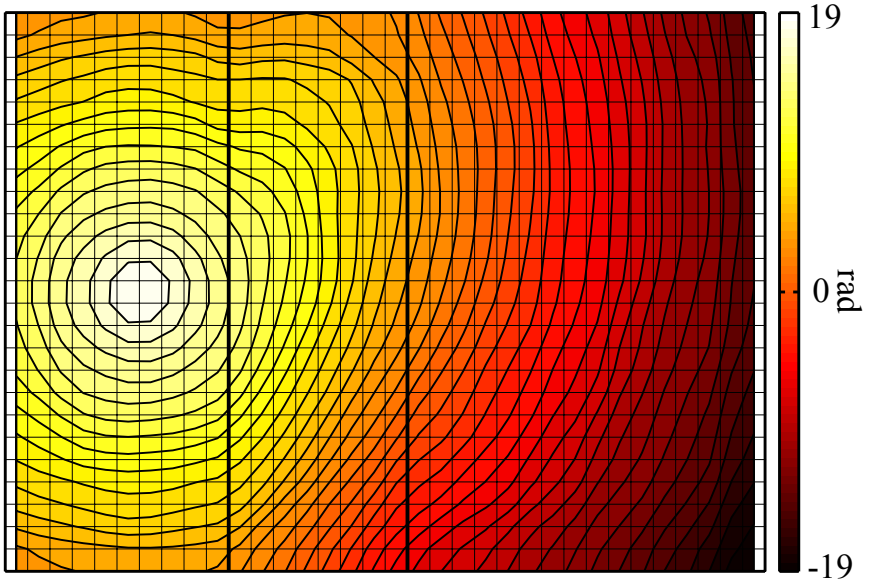

(a) Phase contours at 2.0 GHz

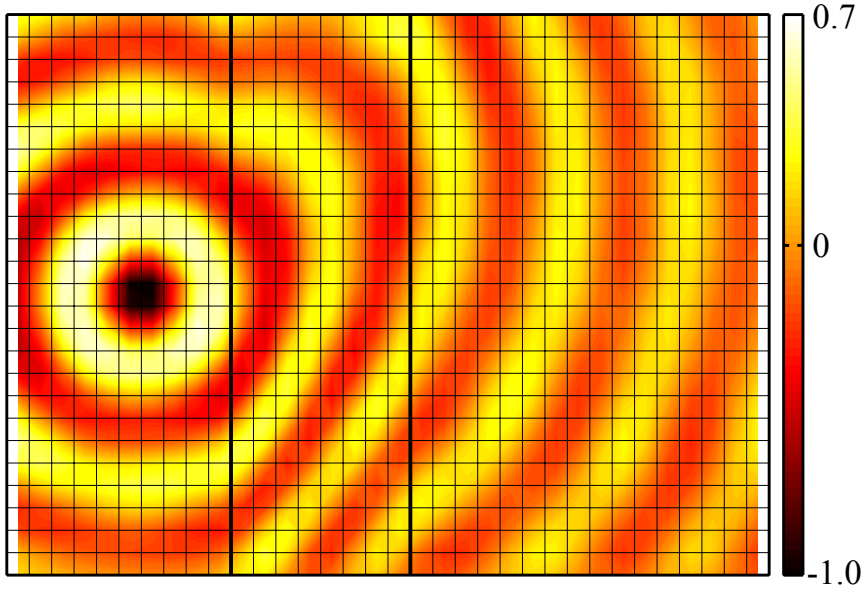

(b) Time snapshot at 2.0 GHz

Figure 4.20: (a) A phase contour plot and (b) time snapshot of the measured, steady state vertical electric field at the interconnecting nodes (see Fig. 4.8) of the experimental structure in Fig. 4.14. The measurement frequency is 2.0 GHz.

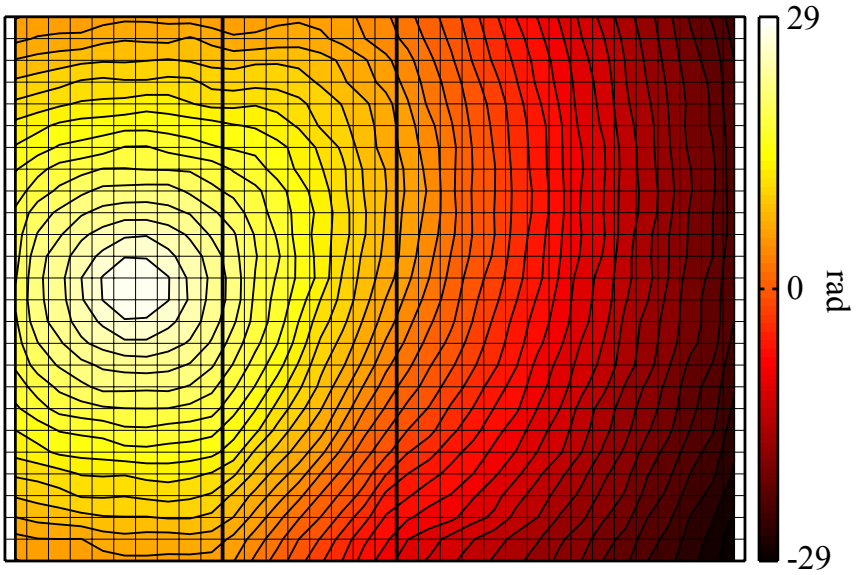

(a) Phase contours at 3.0 GHz

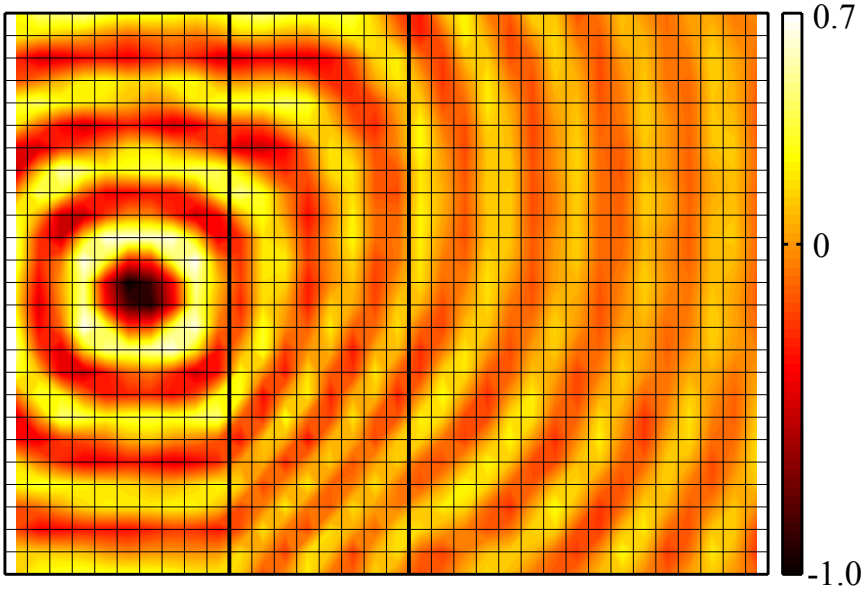

(b) Time snapshot at 3.0 GHz

Figure 4.21: (a) A phase contour plot and (b) time snapshot of the measured, steady state vertical electric field at the interconnecting nodes (see Fig. 4.8) of the experimental structure in Fig. 4.14. The measurement frequency is 3.0 GHz.

CHAPTER V

Tailoring the Phase and Power Flow of Electromagnetic Fields

Greater control over material parameters provides greater control over electromagnetic fields. So far, this thesis has focused on establishing control over the material parameters. This was achieved by designing tensor transmission-line metamaterials. A tensor transmission-line metamaterials' ability to realize arbitrary, anisotropic material parameters has been demonstrated through theory, simulation and experiment. This chapter focuses on translation of this control over material parameters to control of electromagnetic fields. Specifically, the chapter introduces a novel, intuitive and effective method of controlling electromagnetic fields through material anisotropy and inhomogeneity.

5.1 Introduction

It is well known that an anisotropic material can support electromagnetic propagation with phase progression and power flow in different directions [98]. This simple fact suggests that a carefully designed medium, which is anisotropic and spatially inhomogeneous, can tailor phase and power flow as a function of position. In such a medium, anisotropy controls the local phase and power flow, while the inhomogeneity

allows spatial variation. Such spatial control of electromagnetic fields can be used to independently tailor the phase and amplitude of a field profile.

Transformation electromagnetics [36, 50], has provided a prescription for finding the material parameters needed for such field manipulation [51, 52, 53, 54]. In transformation electromagnetics, a desired field distribution is derived from an initial one through a coordinate transformation. The form invariance of Maxwell's equations under coordinate transformations is then exploited to calculate the required spatial distribution of material parameters. In short, transformation electromagnetics designs begin with a coordinate transformation, from which material parameters are computed. However, finding the coordinate transformation that yields the field of interest is not always intuitive, straightforward, or necessarily possible. For example, a designer may know what field is needed but may not necessarily know the coordinate transformation that yields the field of interest.

In this chapter, an entirely new method for arbitrarily controlling the phase progression and power flow of electromagnetic fields within a region of interest is proposed. Specifically, the proposed method describes how to design an inhomogeneous, anisotropic medium that supports prescribed spatial distributions of the wave vector ($\vec{k}$) and the direction of Poynting vector ($\vec{S}$). Material parameters are defined in terms of phase progression and power flow within a region of space (the transformation region), that is embedded within a surrounding medium. First, spatial distributions of the wave vector ($\vec{k}$) and Poynting vector ($\vec{S}$) direction are stipulated within the transformation region. From these two distributions, the required anisotropic, inhomogeneous material parameters needed to support such propagation are found. Plane-wave relations in anisotropic media are used along with an impedance matching process to find the material parameters required to establish desired electromagnetic field profiles.

The developed formulation could have a broad technological impact, since it allows

one to independently tailor the phase and amplitude profile of an electromagnetic field. Principally, the work can find application in the design of electromagnetic and optical guiding structures as well as radiating apertures.

Furthermore, proposed method can be related to transformation electromagnetics if the prescribed spatial distributions of $\vec{k}$ and direction of $\vec{S}$ are given in terms of coordinate transformation. In this case, the proposed method can be used to find alternative material parameters for transformation electromagnetic devices. These alternative material parameters can support exactly the same field pattern as the original ones of the transformation electromagnetic device for a particular polarization. The same approach used in finding the alternative material parameters can be extended further to design dual functional devices that combine the characteristics of two separate transformation electromagnetics devices into one.

The rest of the chapter is organized into six sections. The next section outlines the proposed deign method. It starts with a review of plane-wave relations in an anisotropic, homogeneous medium. These relations are then used to develop a systematic design procedure for finding the material parameters needed to support arbitrary spatial distributions of phase and power flow. The following section presents examples that demonstrate the potential of the described approach. In these examples, the field of a cylindrical source is tailored to realize field profiles with various phase and amplitude distributions. The examples were carefully chosen to demonstrate the method's arbitrary (independent) control over the phase and power flow of electromagnetic fields. Next, the relationship between the proposed method and transformation electromagnetics is drawn. The method is used to find alternative material parameters for transformation electromagnetic devices and to design dual functional transformation electromagnetic devices. The simulated performance of these devices is presented for verification purposes. Toward the end of chapter, specific applications of the proposed method for the design of guiding and radiating

electromagnetic structures are discussed. The last section summarizes the findings of this chapter.

5.2 The Design Method

The proposed design method can be explained in simple, qualitative terms. The medium to be designed can be viewed as a canvas onto which we paint the desired arrows of phase progression and power flow direction. From these two plots, we then derive the material parameters needed to support such propagation. A few simplifying assumptions are made in finding the material parameters of the anisotropic inhomogeneous transformation region. In the design approach, it is assumed that (a) the region is discretized into unit cells that are much smaller than the guided wavelength and (b) the discretized cells are displaced (not in the extreme near field) from a localized source. This allows the electromagnetic field within each cell to be treated locally as a plane wave.

5.2.1 Plane-Wave Relations in Anisotropic Homogeneous Medium

For simplicity, the proposed design approach is applied to a 2D medium. In particular, a TM_z polarization is considered (a TE_z formulation can be derived using Duality [99]). Therefore, the non-zero field quantities are the magnetic field in x and y directions (H_x and H_y) and the electric field in z direction (E_z). At each point in space, the relevant material parameters are a 2×2 relative permeability tensor in the $x - y$ plane and a scalar relative permittivity in the z direction:

$$\bar{\bar{\mu}} = \begin{bmatrix} \mu_{xx} & \mu_{xy} \\ \mu_{yx} & \mu_{yy} \end{bmatrix}, \qquad \epsilon = \epsilon_z. \tag{5.1}$$

We will first review plane-wave relations in an anisotropic homogeneous medium,

and then use them to define material parameters in terms of the local wave vector $\vec{k}$, direction of Poynting vector $\vec{S}$ and the permittivity constant ϵ_z. For the polarization of interest, Maxwell's time-harmonic equations for plane waves are:

$$-j\vec{k} \times \vec{E} = -j\omega\bar{\bar{\mu}}\mu_o\vec{H}, \tag{5.2}$$

$$-j\vec{k} \times \vec{H} = j\omega\epsilon_z\epsilon_o\vec{E}. \tag{5.3}$$

Considering only the non-zero field quantities, these two vector equations can be rewritten as:

$$\begin{bmatrix} \overline{k}_y \\ \overline{k}_x \end{bmatrix} = \begin{bmatrix} \mu_{xx} & -\mu_{xy} \\ -\mu_{yx} & \mu_{yy} \end{bmatrix} \begin{bmatrix} \overline{\eta}_y{}^{-1} \\ \overline{\eta}_x{}^{-1} \end{bmatrix} \tag{5.4}$$

$$\epsilon_z = \begin{bmatrix} \overline{k}_x & \overline{k}_y \end{bmatrix} \begin{bmatrix} \overline{\eta}_x{}^{-1} \\ \overline{\eta}_y{}^{-1} \end{bmatrix} \tag{5.5}$$

where $\overline{\eta}_x = -\frac{1}{\eta_o}\frac{E_z}{H_y}$, $\overline{\eta}_y = \frac{1}{\eta_o}\frac{E_z}{H_x}$ are the wave impedances and $\overline{k}_x = \frac{k_x}{k_o}$, $\overline{k}_y = \frac{k_y}{k_o}$ are the wave numbers in the x and y directions, normalized with respect to their free space values. Using (5.5), the wave impedances can be written in terms of the wave numbers, the ratio $\kappa = \frac{\overline{\eta}_x}{\overline{\eta}_y}$, and the permittivity constant:

$$\overline{\eta}_x = \frac{\overline{k}_x + \kappa\overline{k}_y}{\epsilon_z}, \qquad \overline{\eta}_y = \frac{\overline{k}_x + \kappa\overline{k}_y}{\kappa\epsilon_z}. \tag{5.6}$$

The ratio κ defines the direction (θ_s) of $\vec{S}$ with respect to the x axis: κ=tan(θ_s). Therefore, if $\vec{k} = k_x\hat{x} + k_y\hat{y}$ and the ratio κ are given at a point in space, the wave impedances are defined by the local permittivity. Expressions for the permeability

tensor can also be written using (5.4) and (5.5) as:

$$\bar{\bar{\mu}} = \begin{bmatrix} \frac{\overline{k}_y}{\epsilon_z}(\frac{\overline{k}_x}{\kappa} + \overline{k}_y) + \frac{\mu_{xy}}{\kappa} & \mu_{xy} \\ \mu_{yx} & \frac{\overline{k}_x}{\epsilon_z}(\overline{k}_x + \kappa\overline{k}_y) + \mu_{yx}\kappa \end{bmatrix}, \tag{5.7}$$

where μ_{xy} and μ_{yx} can be chosen arbitrarily, while still ensuring the specified phase and power flow. If it is further assumed that the permeability tensor $\bar{\bar{\mu}}$ is symmetric and its determinant is equal to that of the surrounding medium's (assumed to be free space) permeability $\bar{\bar{\mu}}_s$

$$|\bar{\bar{\mu}}| = |\bar{\bar{\mu}}_s| = 1, \tag{5.8}$$

the expressions for the permeability tensor simplify to:

$$\bar{\bar{\mu}} = \begin{bmatrix} \frac{\epsilon_z}{(\overline{k}_x+\kappa\overline{k}_y)^2} + \frac{\overline{k}_y^2}{\epsilon_z} & \frac{\kappa\epsilon_z}{(\overline{k}_x+\kappa\overline{k}_y)^2} - \frac{\overline{k}_x\overline{k}_y}{\epsilon_z} \\ \frac{\kappa\epsilon_z}{(\overline{k}_x+\kappa\overline{k}_y)^2} - \frac{\overline{k}_x\overline{k}_y}{\epsilon_z} & \frac{\kappa^2\epsilon_z}{(\overline{k}_x+\kappa\overline{k}_y)^2} + \frac{\overline{k}_x^2}{\epsilon_z} \end{bmatrix}. \tag{5.9}$$

This condition on the determinant of the permeability tensor is an inherent property of transformation electromagnetics designs. It ensures that the transformed region (device) remains impedance matched to its surrounding medium under all plane-wave excitations. Therefore, if $\vec{k}$ and κ are stipulated, (5.9) shows that the local permittivity constant defines the local permeability tensor.

5.2.2 A Systematic Design Procedure To Find Material Parameters

Using the expressions for the wave impedances (5.6) and permeability entries (5.9), a systematic design procedure is introduced for finding the material parameters needed to support arbitrary spatial distributions of phase and power flow. The design procedure allows the material parameters of the anisotropic, inhomogeneous transformation region to be found.

To find the material parameters, the two dimensional transformation region is

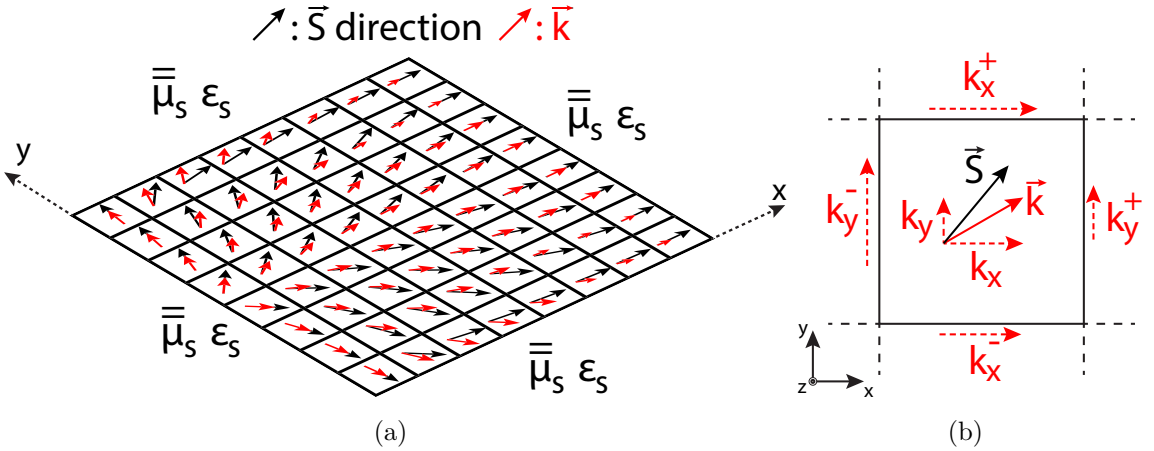

Figure 5.1: (a) The transformation region embedded within a surrounding medium. The transformation region is discretized into unit cells, with the wave vector $\vec{k}$ and direction of $\vec{S}$ stipulated at the center of each cell. (b) A unit cell of the transformation region. The wavenumbers along the edges of the cell are shown. The equality $\Delta k_x = \Delta k_y$ must hold for a unit cell where $\Delta k_x = k_x^+ - k_x^-$ and $\Delta k_y = k_y^+ - k_y^-$. The wave vector at the center of unit cell is $\vec{k} = \frac{k_x^+ + k_x^-}{2}\hat{x} + \frac{k_y^+ + k_y^-}{2}\hat{y}$.

discretized into a grid of unit cells, as shown in Fig 5.1(a). Here, a simple square grid is considered. Next, $\vec{k}$ and direction of $\vec{S}$ are stipulated at the center of each unit cell, defining the phase and power flow within the discretized space (see Fig. 5.1(a)). From these two spatial distributions, the permeability of the unit cells can be written in terms of each cell's permittivity using (5.9). Therefore, the unknowns to be solved for become the unit cell permittivities. They can be found through an impedance matching process in which the wave impedances, given by (5.6), of adjacent unit cells are matched. Once the permittivities are found through this process, the permeability entries can be computed using (5.9).

A rigorous optimization method for finding the optimal permittivity distribution that impedance matches adjacent cells is described in the Appendix B. The optimization process adjusts the permittivities of all unit cells to minimize inter-cell reflections. For designs where there are input and desired output field distributions, a linear transition in wave impedances between the input and output can be used

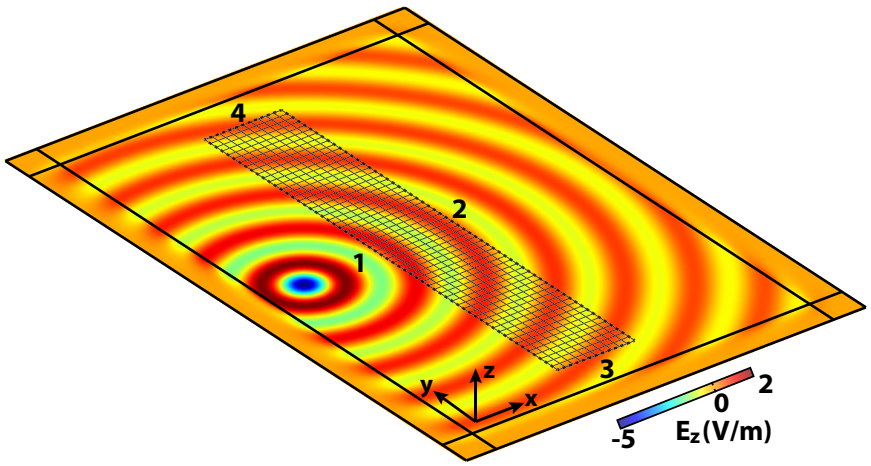

Figure 5.2: A time snapshot of the vertical electric field (E_z) radiated from a cylindrical (vertical electric current) source in an isotropic medium ($\mu = 1$, $\epsilon = 1$). The transformation region, consisting of 10×60 square unit cells ($1.4\lambda_\circ \times 8.4\lambda_\circ$ at 10 GHz), is denoted by dashed lines. In the examples, the source's field is reshaped over the transformation region.

to find the permittivity distribution instead of an optimization process. According to (5.6), the permittivity of a unit cell can be calculated from one of its wave impedances, $\overline{\eta}_x$ or $\overline{\eta}_y$, if $\vec{k}$ and κ are specified. This simple technique will be used to find the permittivity distributions for the design examples presented in Section 5.3. As noted earlier, once the permittivity values of the unit cells are found, the permeability tensor is calculated using (5.9). Due to (5.8), the inhomogeneous, anisotropic transformation region remains impedance matched to its surrounding medium under different excitations.

5.3 Examples: Tailoring the Field of a Cylindrical Source

To demonstrate the potential of the described approach for controlling electromagnetic fields, six illustrative examples are presented. These examples were carefully chosen to highlight the proposed method's ability to control the phase and power flow of electromagnetic fields.

Let us consider a vertical electric current source radiating in an isotropic medium

with relative material parameters: $\mu_s = 1$, $\epsilon_s = 1$. A time snapshot of the vertical electric field emanating from the cylindrical source is shown in Fig. 5.2. In the examples, the source's field is reshaped over the transformation region, denoted by the dashed lines. The transformation region is discretized into 10×60 square unit cells. The unit cell dimension is assumed to be $d = \frac{\lambda_\circ}{7.2}$ (4.2 mm) at an operating frequency of 10 GHz. This results in a transformation region that is $1.4\lambda_\circ \times 8.4\lambda_\circ$. The cylindrical source is located 10 unit cells from the input boundary (boundary 1 shown in Fig. 5.2). Through these examples, we will demonstrate arbitrary spatial control of the wave vector and Poynting vector direction within the transformation region. Such control over electromagnetic fields will be used to transform the incident field at input boundary 1 to a desired field (amplitude and phase) distribution at output boundary 2 (see Fig. 5.2). All electromagnetic simulations are performed using COMSOL Multiphysics: a commercial finite element electromagnetic solver.

A few things need to be said about defining the phase progression and power flow within the transformation region. In general, the phase progression must be physical. The difference in wavenumbers between a unit cell's y-directed edges ($\Delta k_y = k_y^+ - k_y^-$) must be equal to the difference in wavenumbers between its x directed edges ($\Delta k_x = k_x^+ - k_x^-$), as shown in Fig. 5.1(b). In other words, the phase delay around the cell edges must sum to zero: $k_y^- + k_x^+ - k_y^+ - k_x^- = 0$. The wave vector at the center of each unit cell can be found by averaging the wavenumbers along the x- and y- directed edges separately: $\vec{k} = \frac{k_x^+ + k_x^-}{2}\hat{x} + \frac{k_y^+ + k_y^-}{2}\hat{y}$. In contrast, the Poynting vector direction at the center of each unit cell can be set arbitrarily.

In all the examples that follow, phase progression within the transformation region is systematically defined. The wavenumbers k_y along the input boundary (boundary 1 in Fig. 5.2) are dictated by the cylindrical excitation, given that the transformation region is reflectionless. The wavenumbers k_y along all other y-directed unit cell edges are assigned, assuming the input phase distribution (k_y variation) at boundary 1

transitions linearly through the transformation region to the output phase distribution at boundary 2. The wavenumbers k_x along boundary 3 are assigned arbitrarily. The wavenumbers k_x along all other x-directed cell edges are then found using the relation: $\Delta k_x = \Delta k_y$.

The Poynting vector directions for cells along boundary 1 are dictated by the cylindrical excitation. In the first four examples, linear power flow through the transformation region is assumed when mapping the input power density at boundary 1 to the output power density at boundary 2. A detailed discussion of the linear power density mapping is provided in Appendix C. The mapping allows the Poynting vector direction to be determined at the center of each unit cell within the transformation region. Further, the power through the input and output boundaries is assumed to be equal, in order to eliminate power leakage through the sides (boundaries 3 and 4) of the transformation region. The permittivity distribution in the transformation region is calculated using (5.6) from the wave vector and power flow distributions and $\overline{\eta}_x$, which is linearly varied from boundary 1 to boundary 2. It should be pointed out that linear power flow and a linear phase transition from the input to the output field profiles are assumed for simplicity. These are only one set of an infinite number of possibilities. In fact, the last two examples demonstrate cases where linear power flow from input boundary 1 to output boundary 2 is not assumed.

5.3.1 Output Profile with a Trapezoidal Power Density and Linear Phase

First, let us consider an example where the transformation region produces a trapezoidal power density with a linear phase progression at boundary 2. Specifically, a wavenumber of $k_y = 0.20k_o$ is chosen along the boundary 2, and a wave number of $k_x = 0$ along boundary 3. Fig. 5.3(a) shows the assigned $\vec{k}$ and direction of $\vec{S}$ vectors with red and black arrows, respectively. The calculated permittivity distribution is shown in Fig. 5.3(b). The permeability tensor of each unit cell is found by substituting

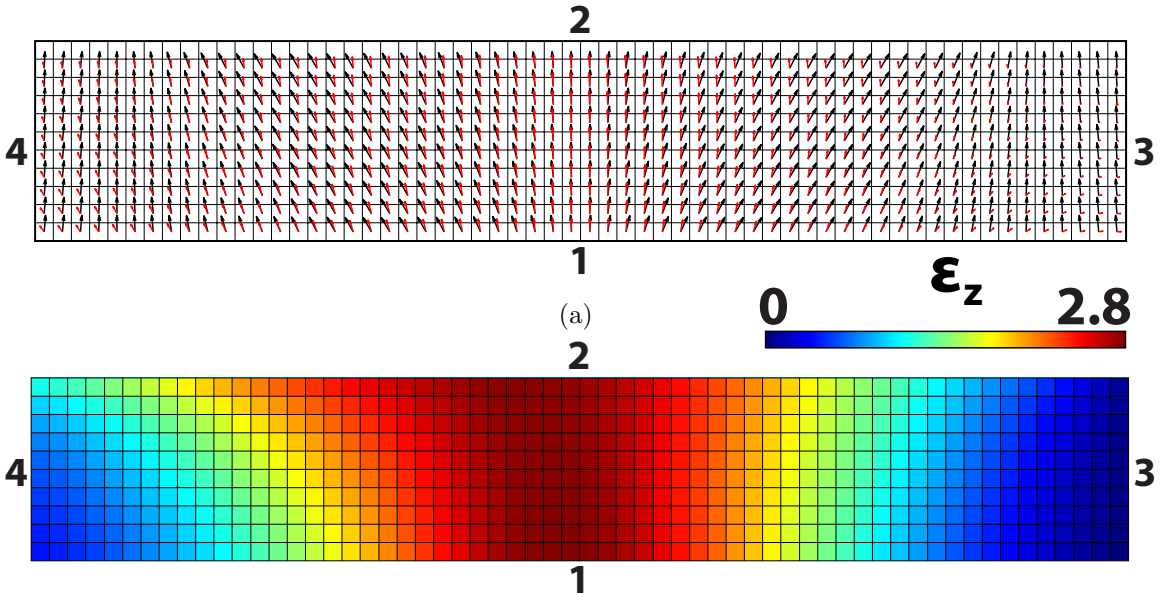

Figure 5.3: (a) Spatial distributions of $\vec{k}$ and direction of $\vec{S}$ that establish a trapezoidal power density and linear phase profile along boundary 2. (b) Calculated permittivity distribution assuming a linearly tapered wave impedance, $\overline{\eta}_x$, from boundary 1 to boundary 2.

the vector distributions of Fig. 5.3(a) and the permittivity values of Fig. 5.3(b) into (5.9). A time snapshot of the simulated, vertical electric field (E_z) is shown in Fig. 5.4(a). A beam emerging from boundary 2 at an angle of 12° with respect to x axis is observed, verifying that the phase progression along boundary 2 is $k_y = 0.20k_o$. Fig. 5.4(b) and Fig. 5.4(c) plot the ideal (stipulated) and simulated power density and phase profiles at boundaries 1 and 2. Close agreement is shown.

5.3.2 Output Profile with a Trapezoidal Power Density and Uniform Phase

The first example considered a transformation region that produces a trapezoidal power density with a linear phase progression along boundary 2. Here, we present a variation of this example, where the transformation region produces a trapezoidal power density with a uniform phase progression at boundary 2. Specifically, a

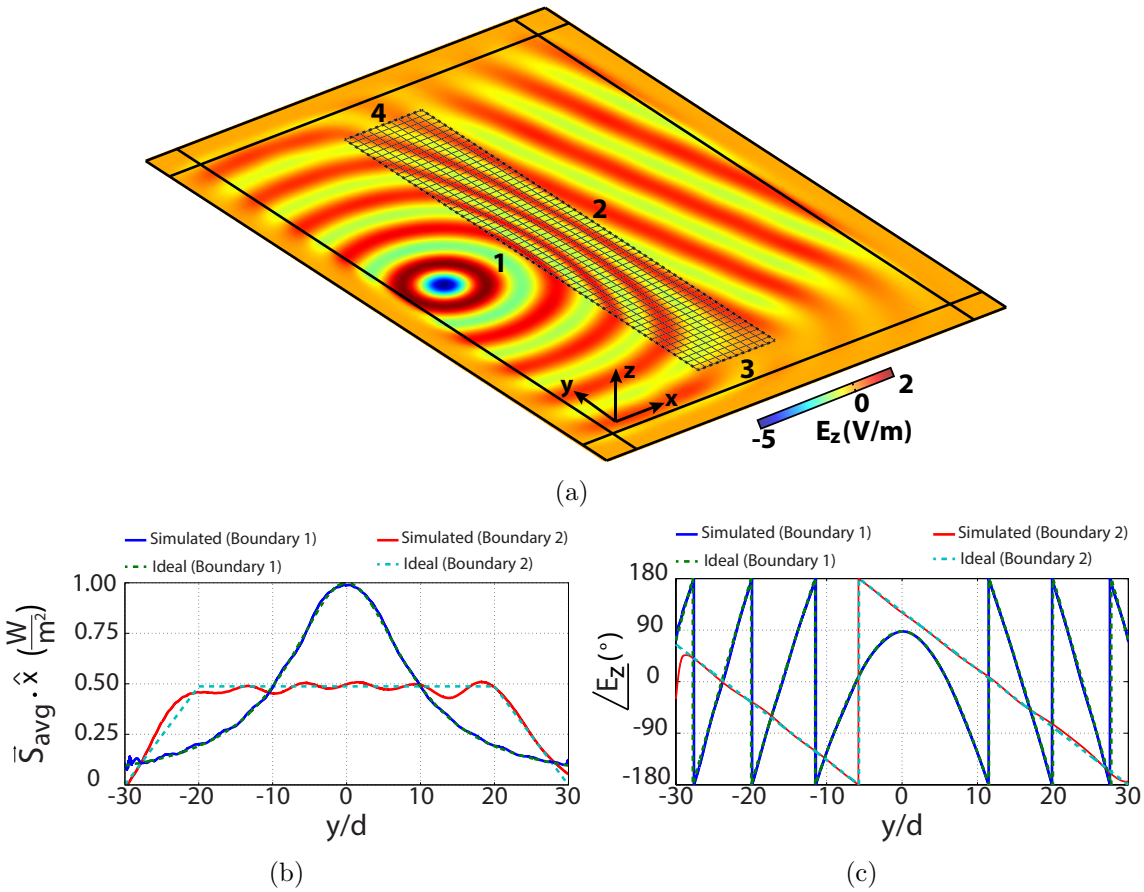

Figure 5.4: (a) Time snapshot of the simulated, vertical electric field (E_z) within the transformation region of the design shown in Fig. 5.3. (b) Simulated and ideal power densities along boundary 1 and boundary 2 (c) Phase profiles along boundary 1 and boundary 2. $y = 0$ corresponds to the center of the transformation region.

wavenumber of $k_y = 0$ is chosen along boundary 2, and a wave number of $k_x = 0$ along boundary 3. By keeping the power density profile the same as in the previous example and only reshaping the output phase profile, we demonstrate the independent control over the phase flow. Fig. 5.5(a) shows the assigned $\vec{k}$ and direction of $\vec{S}$ vectors with red and black arrows, respectively. The permittivity distribution calculated using the tapered wave impedance approach is shown in Fig. 5.5(b). The permeability tensor of each unit cell is found by substituting the vector distributions of Fig. 5.5(a) and the permittivity values of Fig. 5.5(b) into (5.9). A time snapshot of the simulated, vertical electric field (E_z) is shown in Fig. 5.6(a). A beam emerging from bound-

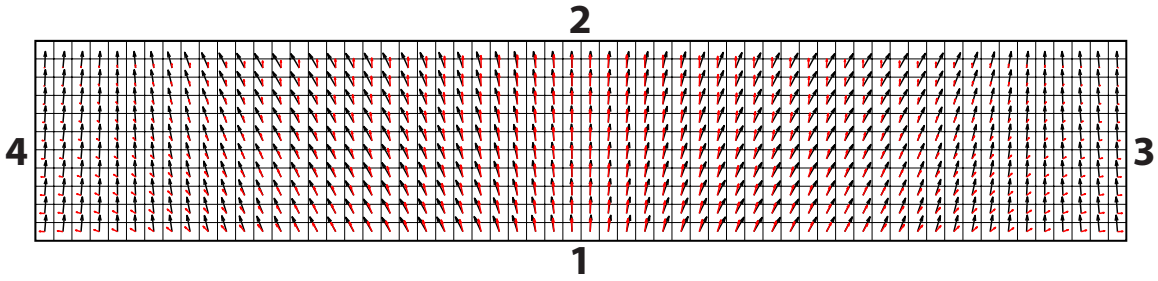

(a)

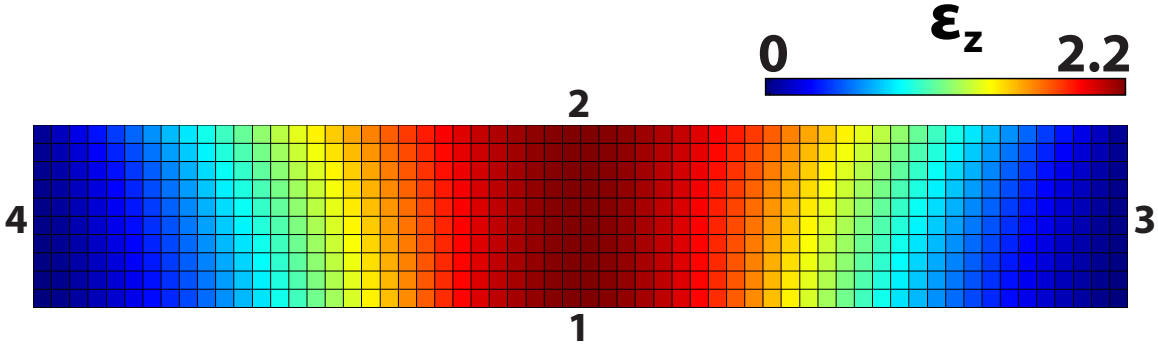

(b)

Figure 5.5: (a) Spatial distributions of $\vec{k}$ and direction of $\vec{S}$ that establish a trapezoidal power density and uniform phase profile along boundary 2. (b) Calculated permittivity distribution assuming a linearly tapered wave impedance $\overline{\eta}_x$ from boundary 1 to boundary 2.

ary 2 in the normal direction is observed, verifying that the phase progression along boundary 2 is $k_y = 0$. Fig. 5.6(b) and Fig. 5.6(c) plot the simulated and ideal power density and phase profiles at boundaries 1 and 2. Close agreement is shown.

5.3.3 Output Profile with Triangular Power Density with Uniform Phase

This time, the phase profile is kept the same as in the previous example, but a different output power profile is stipulated. This is done to demonstrate independent control over the power flow. In this example, a transformation region is designed to produce a triangular power density distribution with a uniform output phase at boundary 2. Zero phase progression ($k_y = 0$) is assumed along boundary 2, and a wavenumber of $k_x = 0$ along boundary 3. Fig. 5.7(a) shows the assigned $\vec{k}$ and direc-

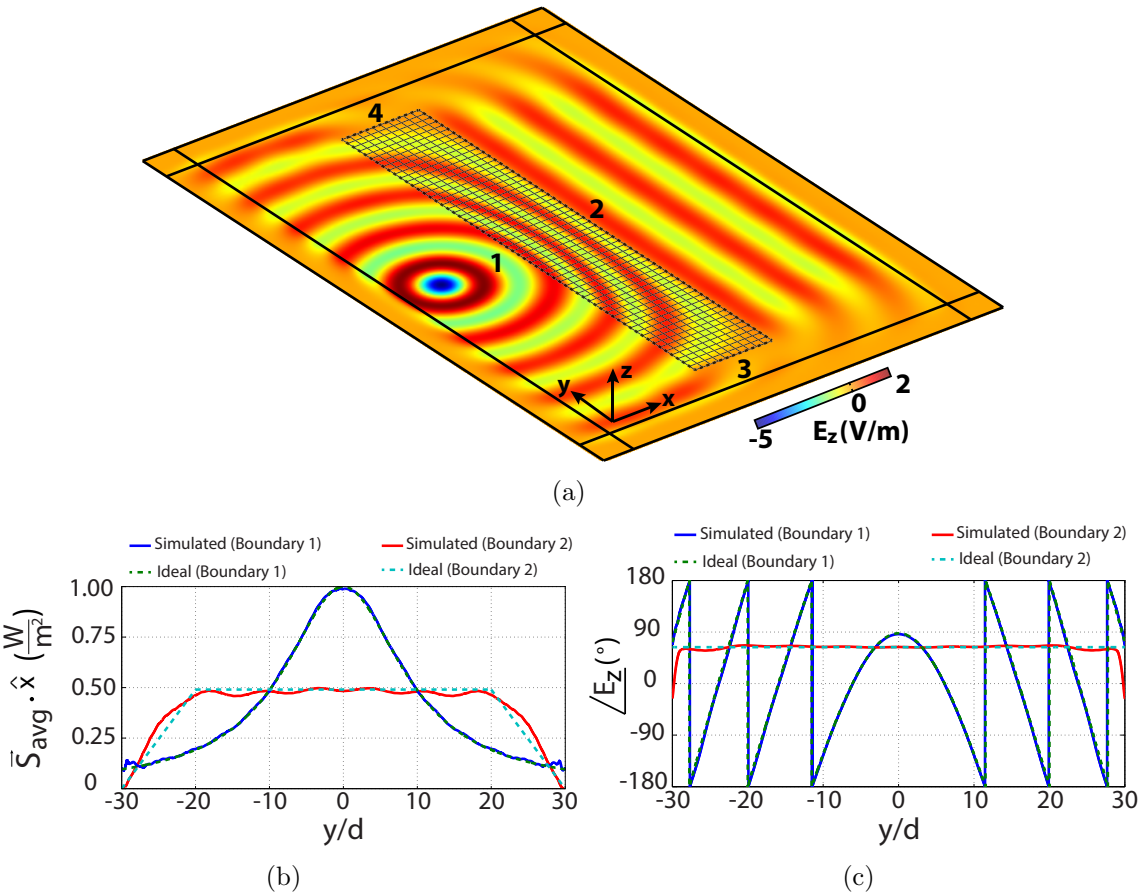

Figure 5.6: (a) Time snapshot of the simulated, vertical electric field (E_z) within the transformation region of the design shown in Fig. 5.5(a). (b) Simulated and ideal power density (c) Phase profiles along boundary 1 and boundary 2. y = 0 corresponds to the center of the transformation region.

tion of $\vec{S}$ vectors with red and black arrows, respectively. The required permittivity distribution is plotted in Fig. 5.7(b). The permeability tensor of each unit cell is found as in the previous examples. A time snapshot of the simulated, vertical electric field is shown in Fig. 5.8(a). A beam emerging from boundary 2 in the normal direction verifies the desired phase progression along boundary 2: $k_y = 0$. In Fig. 5.8(b) and Fig. 5.8(c), the ideal and simulated power density and phase profiles at boundaries 1 and 2 are plotted, and show close agreement.

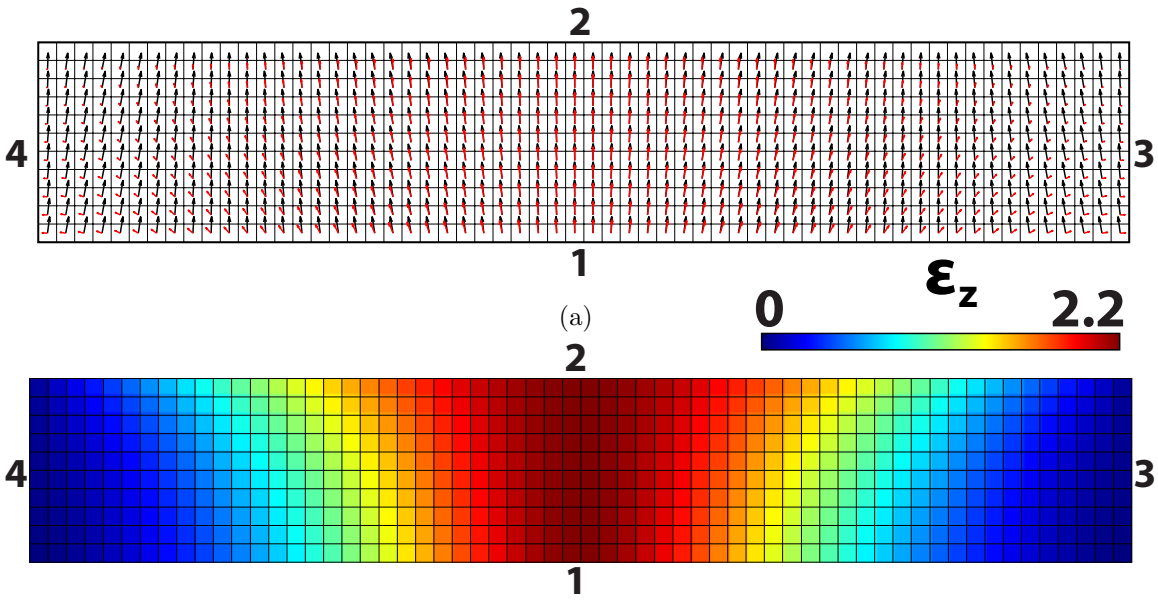

Figure 5.7: (a) Spatial distributions of $\vec{k}$ and direction of $\vec{S}$ that establish a triangular power density and uniform phase profile along boundary 2. (b) Calculated permittivity distribution assuming a linearly tapered wave impedance, $\overline{\eta}_x$, from boundary 1 to boundary 2.

5.3.4 Output Profile with a Trapezoidal Power Density and Arbitrary Phase

The objective of the next example is to show that the proposed method can be used to establish more irregular field profiles. In this example, we consider a transformation region which produces a trapezoidal power density with the arbitrary phase distribution shown in Fig. 5.9(a). Specifically, a varying wavenumber k_y is assigned along boundary 2, and a wave number of $k_x = 0$ along boundary 3. Fig. 5.9(b) shows the assigned $\vec{k}$ and direction of $\vec{S}$ with red and black arrows, respectively. The permittivity distribution calculated using the tapered wave impedance approach is shown in Fig. 5.9(c). The permeability tensor of each unit cell is found by substituting the vector distributions of Fig. 5.9(b) and the permittivity values of Fig. 5.9(c) into (5.9). A time snapshot of the simulated, vertical electric field (E_z) and simulated Poynting vector direction at the center of unit cells are shown in Fig. 5.10(a). A top

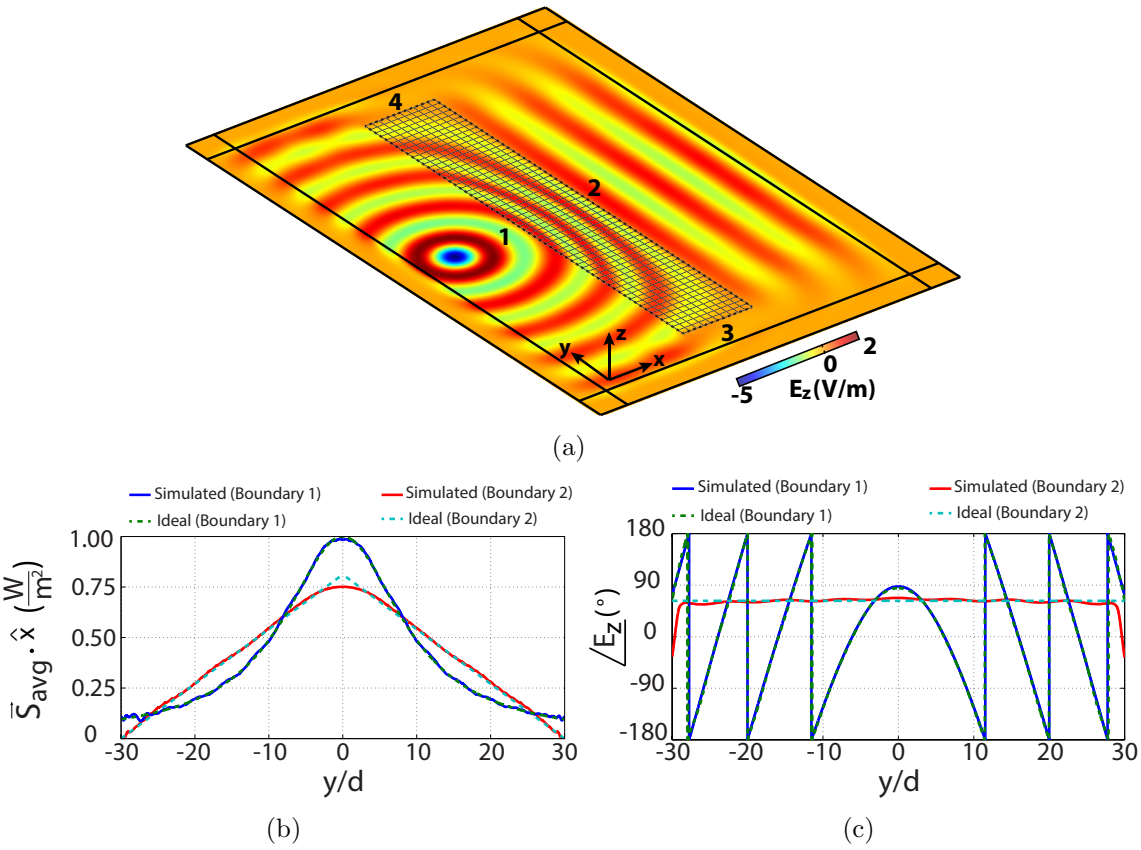

Figure 5.8: (a) Time snapshot of the simulated, vertical electric field (E_z) within the transformation region of the design shown in Fig. 5.7. (b) Simulated and ideal power densities along boundary 1 and boundary 2. (c) Phase profiles along boundary 1 and boundary 2. $y = 0$ corresponds to the center of the transformation region.

view of the field is shown in Fig. 5.10(a) for a better visualization of the simulated Poynting vector directions. Fig. 5.10(b) and Fig. 5.10(c) plot the simulated and ideal power density and phase profiles at boundaries 1 and 2. The close agreement verifies that the method can support irregular output field profiles.

5.3.5 Output Profile with a Trapezoidal Power Density and Uniform Phase Achieved Using Different Power Flow Distributions

Here, we revisit the case where the transformation region produces a trapezoidal power density with a uniform phase progression along boundary 2. However, the

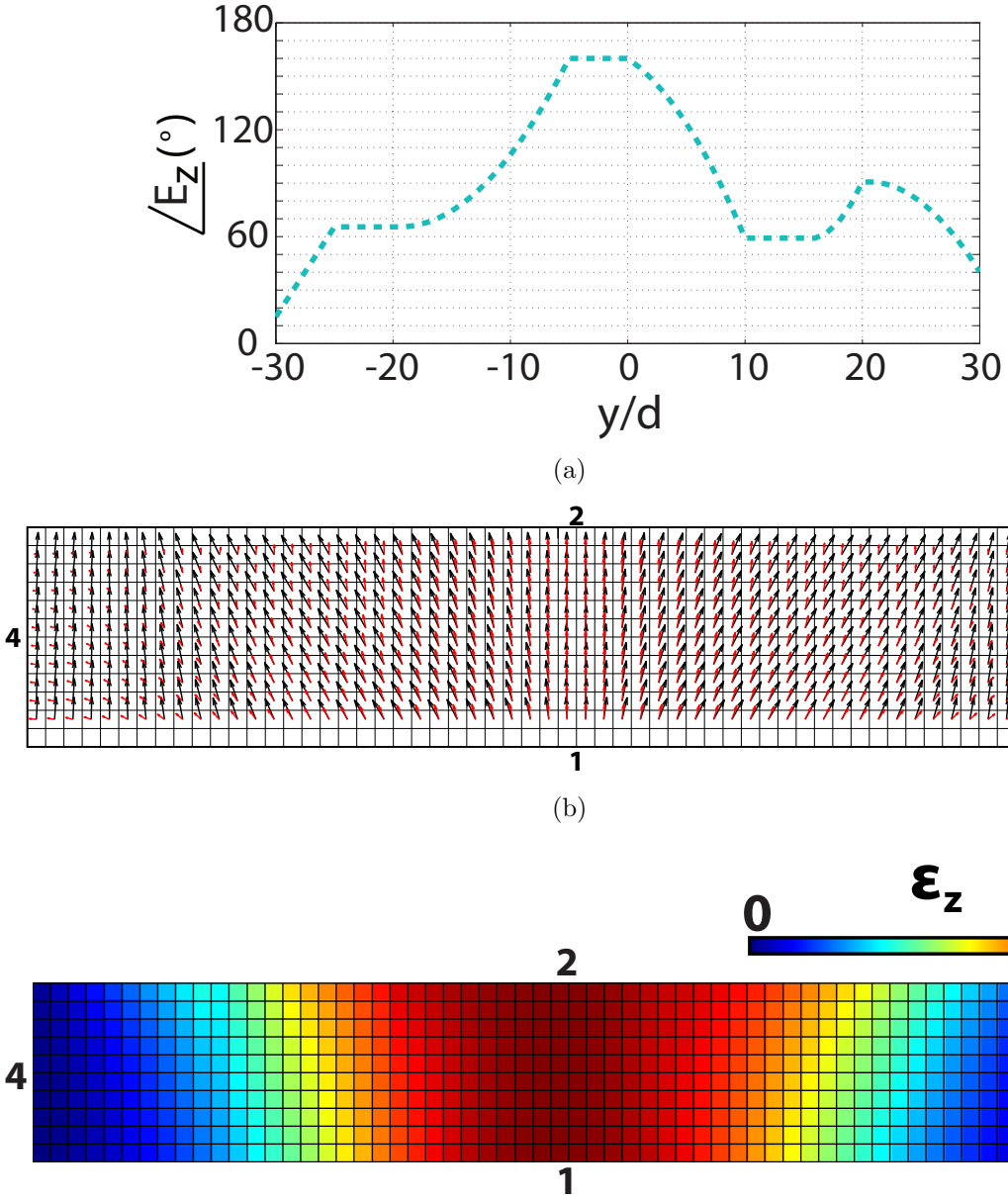

Figure 5.9: (a) Desired output phase profile. Tangential wave numbers, k_y, along boundary 2 are assigned accordingly. (b) Spatial distributions of $\vec{k}$ and direction of $\vec{S}$ that establish a trapezoidal power density and uniform phase profile along boundary 2. (c) Calculated permittivity distribution assuming a linearly tapered wave impedance $\overline{\eta}_x$ from boundary 1 to boundary 2.

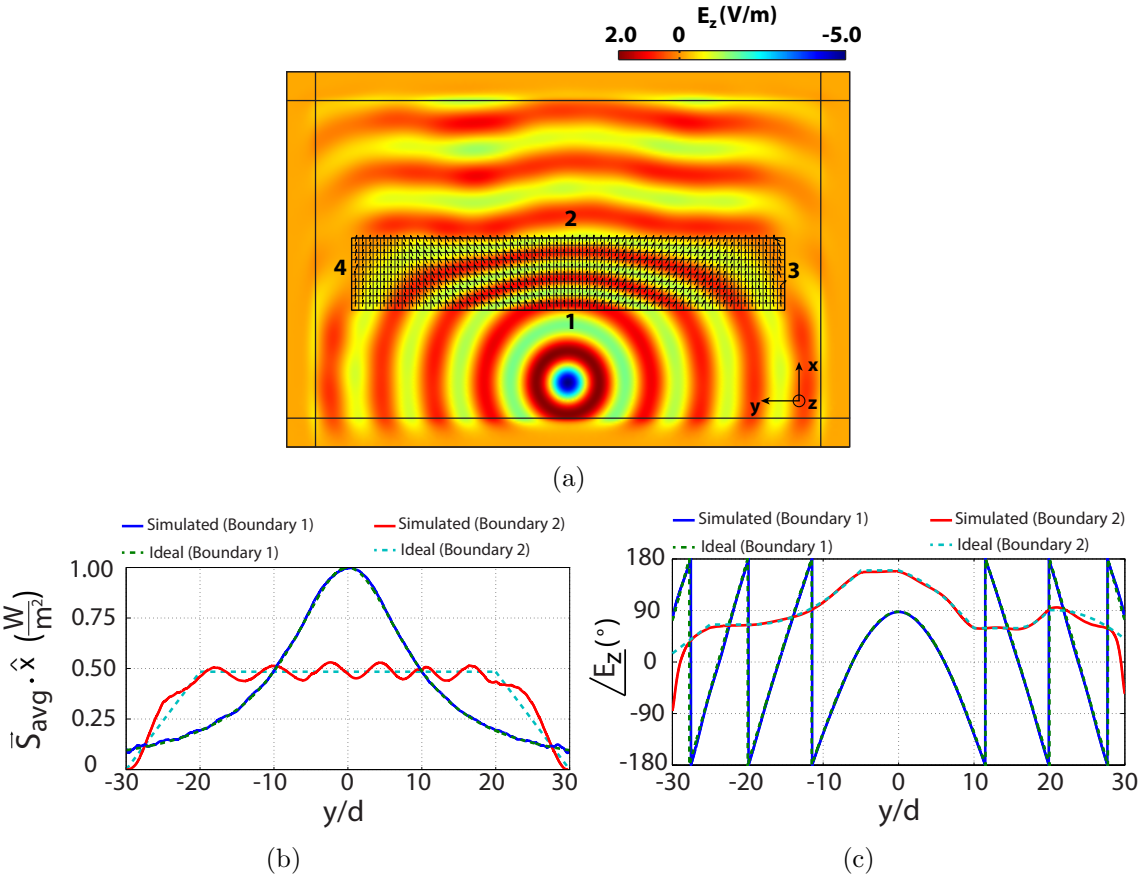

Figure 5.10: (a) Time snapshot of the simulated, vertical electric field (E_z) within the transformation region of the design shown in Fig. 5.9(a). Black arrows show the simulated Poynting vector directions at the center of unit cells. (b) Simulated and ideal power density (c) Phase profiles along boundary 1 and boundary 2. y = 0 corresponds to the center of the transformation region.

Poynting vector directions are chosen to be different from the the linear power flow distribution used earlier. This example shows that even abrupt changes in power flow are possible within the transformation region, and that different power flow assignments can result in the same power density profile at the output. It should be pointed out that the phase is still linearly varied from input to output in this example. A wavenumber of $k_y = 0$ is chosen along boundary 2, and a wave number of $k_x = 0$ along boundary 3. Fig. 5.11(a) shows the assigned $\vec{k}$ and direction of $\vec{S}$ with red and black arrows, respectively. The permittivity distribution calculated using the

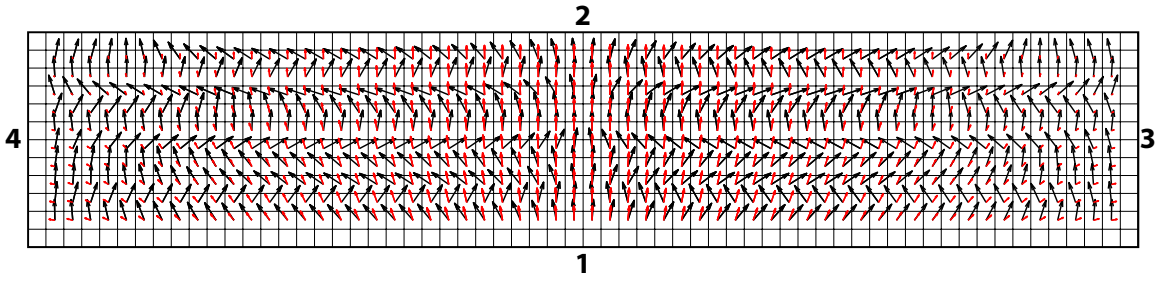

(a)

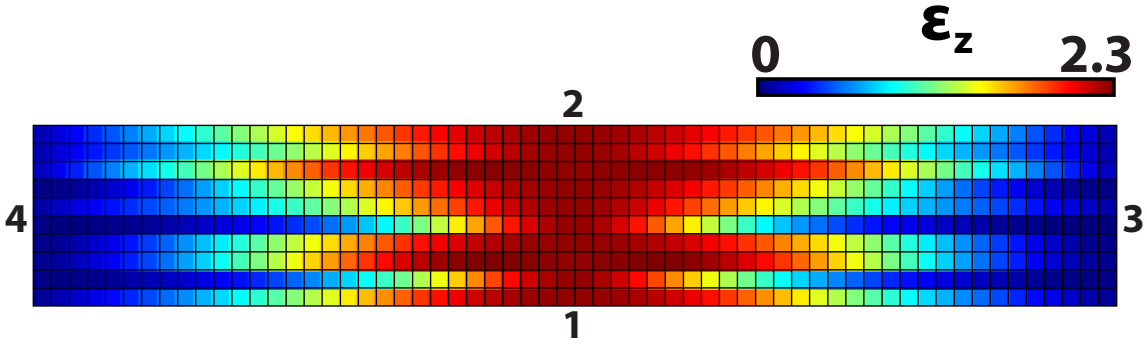

(b)

Figure 5.11: (a) Spatial distributions of $\vec{k}$ and direction of $\vec{S}$ that establish a trapezoidal power density and uniform phase profile along boundary 2. (b) Calculated permittivity distribution assuming a linearly tapered wave impedance $\overline{\eta}_x$ from boundary 1 to boundary 2.

tapered wave impedance approach is shown in Fig. 5.11(b). The permeability tensor of each unit cell is found by substituting the vector distributions of Fig. 5.11(a) and the permittivity values of Fig. 5.11(b) into (5.9). A time snapshot of the simulated, vertical electric field (E_z) and simulated Poynting vector direction at the center of unit cells are shown in Fig. 5.12(a). A top view of the field is shown Fig. 5.12(a) for a better visualization of the simulated Poynting vector directions. Fig. 5.12(b) and Fig. 5.12(c) plot the simulated and ideal power density and phase profiles at boundaries 1 and 2. The close agreement verifies that the method can support abrupt changes in the vectorial distributions. It also highlights the fact that there are infinite number of vectorial distributions that can yield the same output field profile.

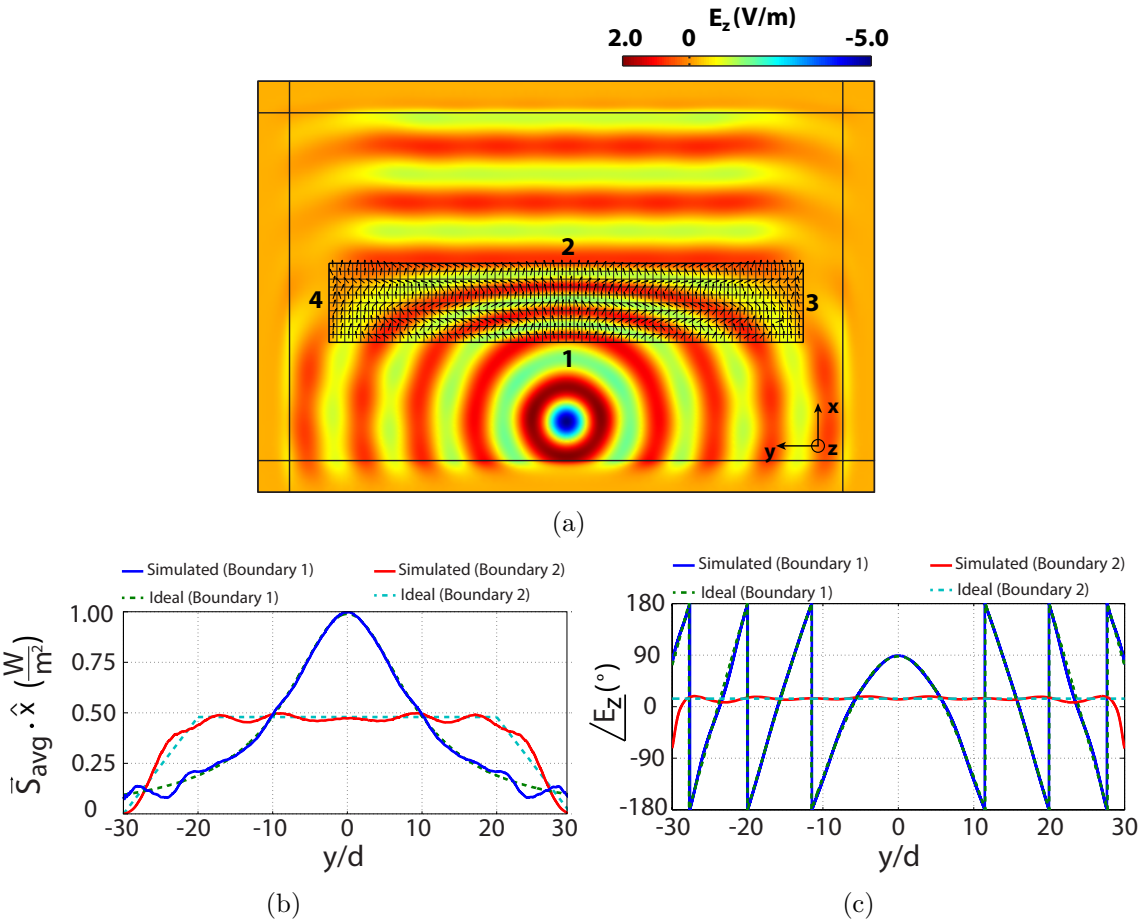

Figure 5.12: (a) Time snapshot of the simulated, vertical electric field (E_z) within the transformation region of the design shown in Fig. 5.11(a). Black arrows show the simulated Poynting vector directions at the center of unit cells. (b) Simulated and ideal power density (c) Phase profiles along boundary 1 and boundary 2. y = 0 corresponds to the center of the transformation region.

5.3.6 Arbitrary Control of Phase and Power Control Within the Transformation Region

The examples presented so far have shown that the field of a source can be molded into desired phase and amplitude profiles. However, the proposed design approach is not limited to designing devices based solely on input-output relations. The design approach provides full control of the phase progression and power flow of electromagnetic fields within a region of space (the transformation region) without aiming for a

specific output profile. This last example considers the case where power flow within the transformation region is assigned arbitrarily, while the phase of the source field is collimated.

In this example, the Poynting vector directions are changed linearly from boundary 1 to boundary 2 along a fixed value of y (a row). For the first 15 rows (closest to boundary 4), the angle of the Poynting vector with respect to the x axis decreases from its initial value at boundary 1 to an angle of zero degrees at boundary 2. For the next 30 rows (central section of the transformation region), the Poynting vector angle decreases from its value at boundary 1 to the negative of that angle at boundary 2. For the last 15 rows (closest to boundary 3), the Poynting vector angle decreases from its value at boundary 1 to an angle of -30 degrees at boundary 2. The wave vectors within the transformation region are chosen to be the same as those in the second example of the main text (see Fig. 5a), which produce a collimated beam at boundary 2. Fig. 5.13(a) shows the assigned $\vec{k}$ and direction of $\vec{S}$ vectors with red and black arrows, respectively. The permittivity distribution calculated using the tapered wave impedance approach is shown in Fig. 5.13(b). The permeability tensor of each unit cell is found as in the previous examples. Fig. 5.14(a) compares the initially assigned (black) and simulated (blue) Poynting vector directions. Close agreement is once again observed. Moreover, Fig. 5.14(b) plots the phase of the electric field within the transformation region, showing that the field is collimated at boundary 2.

5.4 Beam Former

The condition imposed on the determinant of the permeability tensor (equation 5.8) allows the designed structures to act as a beam former. Laterally displacing the cylindrical source results in the scans the beam emerging from boundary 2. The beam former is in fact reflectionless for all beam scanning angles due to the determinant condition. In this section, the design presented in Section 5.3.2 is revisited. This

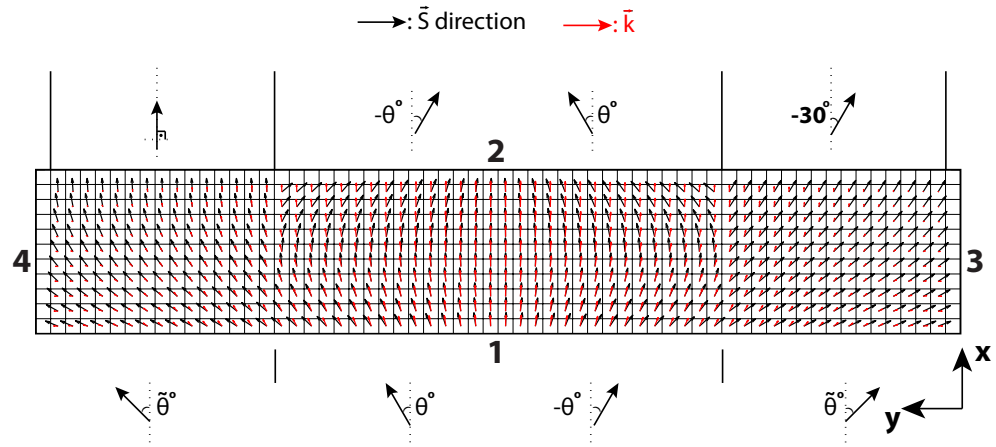

(a)

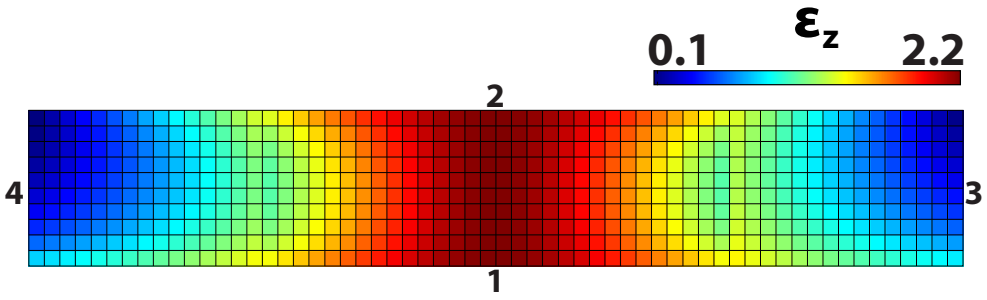

(b)

Figure 5.13: (a) Spatial distributions of $\vec{k}$ and direction of $\vec{S}$ that establish a trapezoidal power density and uniform phase profile along boundary 2. (b) Calculated permittivity distribution assuming a linearly tapered wave impedance, $\overline{\eta}_x$, from boundary 1 to boundary 2.

design produced a trapezoidal power density at the output with a uniform phase. The source is laterally displaced in upward and downward directions to demonstrate the reflectionless beam scanning property of the designed device. Fig. 5.15 shows time snapshots of the simulated, vertical electric fields for various source positions. In Fig. 5.15(a), the source is positioned at the center of the device. A beam emerging from boundary 2 in the normal direction is observed. In Fig. 5.15(b) and Fig. 5.15(c), the source is displaced by 4 and 8 unit cells, respectively, in the upward direction. Beams emerging from boundary 2 at an angles of -13° and -26° are shown, respectively. Similarly, in Fig. 5.15(b) and Fig. 5.15(c), the source is displaced by 4 and 8 unit cells in the downward direction. Beams emerging from boundary 2 at angles of 13°

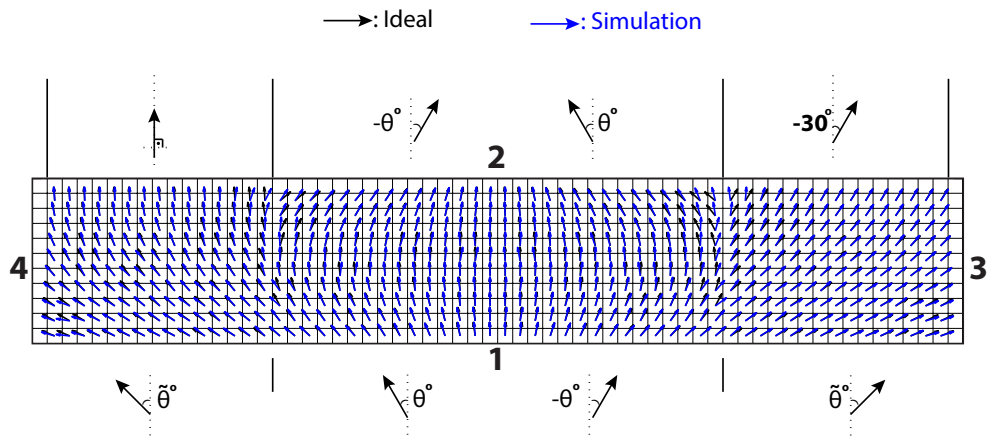

(a)

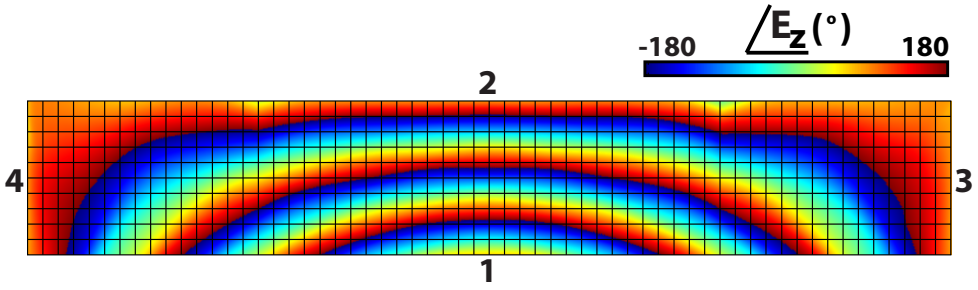

(b)

Figure 5.14: (a) Comparison of the ideal (assigned) and simulated Poynting vector directions. (b) Simulated phase of the vertical electric field (E_z) within the transformation region.

and 26° are observed, respectively.

In all cases, the cylindrical wave is impedance matched to the transformation region since the material parameters satisfy the condition given by (5.8).

5.5 Relationship with Transformation Electromagnetics

The proposed method defines the material parameters in terms of the spatial distributions of the wave vector ($\vec{k}$) and direction of Poynting vector ($\vec{S}$) within a region of space. This method can be related to transformation electromagnetics if the spatial distribution of these vectors are obtained via coordinate transformation. Such a relation will provide an alternative perspective on transformation electromagnetic

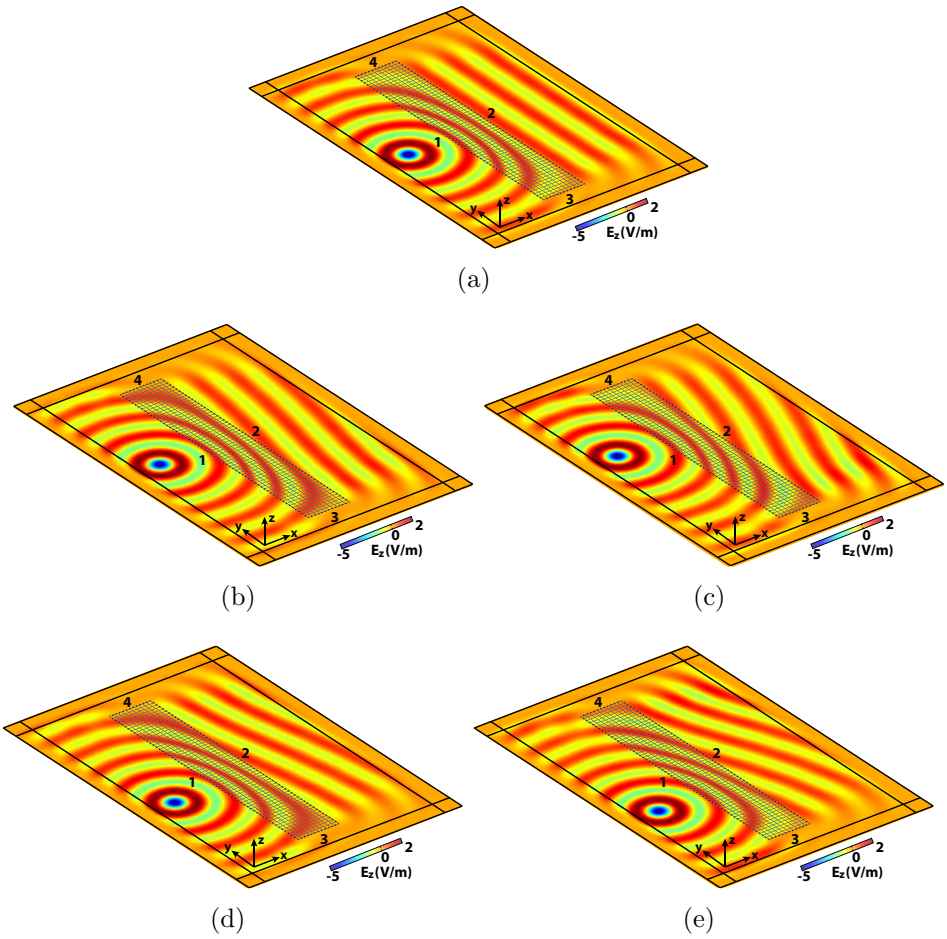

Figure 5.15: A time snapshot of the vertical electric field (E_z) radiated from a cylindrical (vertical electric current) source at laterally displaced positions: (a) center position, (b) 4 unit cells above, (c) 8 unit cells above, (c) 4 unit cells below, (d) 8 unit cells below center position.

device design.

In this section, the proposed method is used to find alternative material parameters for 2D transformation electromagnetics devices. The alternative material parameters support exactly the same field pattern as those of the original transformation electromagnetics device for a given excitation. Furthermore, the same method is extended to design dual functional transformation electromagnetics devices that combine the characteristics of two separate transformation devices into one. Analytical calculations are shown and the results verified through the full-wave simulation of well-known transformation electromagnetics devices: an electromagnetic field rotator

and a cylindrical electromagnetic field concentrator. Although the transformation electromagnetics devices possessing alternative material parameters only work for a particular illumination direction, the method presented will find application in the design of antennas and beam-forming networks with a fixed feed position. Furthermore, the alternative material parameters reported may be used to simplify designs and reduce anisotropy in transformation electromagnetics devices. They can be used to reduce the eigenvalues of material tensors (diagonalized material parameters) since large material parameters can be challenging to realize. They can also lead to designs with attainable circuit components, completely printed implementations and devices with desirable frequency responses when tensor transmission-line metamaterials are considered for their implementation. The dual functional devices requiring nonreciprocal material parameters can also be implemented using tensor transmission-line metamaterial with nonlinear components: transistors, diodes, magnetic materials.

5.5.1 Alternative Material Parameters for Transformation Electromagnetics Designs

First, the concept of alternative material parameters is discussed. Let us consider equation (5.4). If the wavenumbers and wave impedances values, $(\overline{k}_x, \overline{k}_y, \overline{\eta}_x, \overline{\eta}_y)$, are known in (5.4) for all points in space, the permeability and permittivity can be expressed in terms of these quantities. Assuming that both wave impedances are finite, the permeability tensor and permittivity can be written as follows:

$$\overline{\mu} = \begin{bmatrix} \overline{k}_y\overline{\eta}_y + \frac{\overline{\eta}_y}{\overline{\eta}_x}\mu_{xy} & \mu_{xy} \\ \mu_{yx} & \overline{k}_x\overline{\eta}_x + \frac{\overline{\eta}_x}{\overline{\eta}_y}\mu_{yx} \end{bmatrix}, \quad \epsilon_z = \frac{\overline{k}_x}{\overline{\eta}_x} + \frac{\overline{k}_y}{\overline{\eta}_y}, \tag{5.10a}$$

where μ_{xy} and μ_{yx} can be chosen arbitrarily. The material parameters for the limiting cases where one of the wave impedances becomes infinity can also be written. If the

impedance in x direction becomes infinite, ($\overline{\eta}_x \to \infty$):

$$\overline{\mu} = \begin{bmatrix} \overline{k}_y\overline{\eta}_y & \mu_{xy} \\ -\overline{k}_x\overline{\eta}_y & \mu_{yy} \end{bmatrix}, \qquad \epsilon_z = \frac{\overline{k}_y}{\overline{\eta}_y}, \tag{5.10b}$$

where μ_{xy} and μ_{yy} can be chosen arbitrarily. If the impedance in y direction becomes infinite, ($\overline{\eta}_y \to \infty$):

$$\overline{\mu} = \begin{bmatrix} \mu_{xx} & -\overline{k}_y\overline{\eta}_x \\ \mu_{yx} & \overline{k}_x\overline{\eta}_x \end{bmatrix}, \qquad \epsilon_z = \frac{\overline{k}_x}{\overline{\eta}_x}, \tag{5.10c}$$

where μ_{xx} and μ_{yx} can be chosen arbitrarily. As shown by (5.10), an infinite number of solutions (permeability tensors) can be found to satisfy the given set of wave numbers and wave impedances, given that two of the permeability tensor entries μ_{xy}, μ_{yx} can be freely chosen. This fact can be utilized to define alternative material parameters for a transformation electromagnetics design. The spatial distributions of wavenumbers and wave impedances, $(\overline{k}_x, \overline{k}_y, \overline{\eta}_x, \overline{\eta}_y)$ within a transformation electromagnetics device, can be computed for a specific plane-wave illumination. Using (5.10), numerous alternative material parameters can be found that support the same $(\overline{k}_x, \overline{k}_y, \overline{\eta}_x, \overline{\eta}_y)$ distribution for the given plane-wave illumination. The transformation-derived material parameters can be replaced by the alternative ones within any part or over the entire transformed space. The alternative material parameters retain the same $(\overline{k}_x, \overline{k}_y, \overline{\eta}_x, \overline{\eta}_y)$ within the device under the particular plane-wave illumination they were calculated for.

The anisotropy of the transformation electromagnetics device can be reduced using alternative material parameters through a judicious choice of the free parameter μ_{xy} for each unit cell. The free parameters should be chosen such that the dispersion curve of the alternative material parameters most closely approaches a circle. This

specific value of the free parameter can be computed by minimizing the function

$$f(\lambda_1, \lambda_2) = \frac{\lambda_1}{\lambda_2} + \frac{\lambda_2}{\lambda_1}, \tag{5.11}$$

where λ_1, λ_2 are the positive eigenvalues of the alternative permeability tensor given by (5.10a), when the material parameters are reciprocal: $\mu_{xy} = \mu_{yx}$. The function (5.11) is minimized when

$$\mu_{xy} = \mu_{yx} = \frac{\overline{\eta}_x \overline{\eta}_y (\overline{k}_x \overline{\eta}_x - \overline{k}_y \overline{\eta}_y)(\overline{k}_x \overline{\eta}_y - \overline{k}_y \overline{\eta}_x)}{(\overline{k}_x \overline{\eta}_y + \overline{k}_y \overline{\eta}_x)(\overline{\eta}_x^2 + \overline{\eta}_y^2)}. \tag{5.12}$$

For this particular μ_{xy} value, the dispersion curve of the alternative material parameters approaches a circle, while supporting the same wavenumber and wave impedance, $(\overline{k}_x, \overline{k}_y, \overline{\eta}_x, \overline{\eta}_y)$ as the transformed material parameters.

The alternative material parameters (5.10a) become equal to the transformation-derived material parameters for specific values of μ_{xy} and μ_{yx}. If the permeability matrix is symmetric and its determinant is set to unity (assuming that the initial medium is free space), the following off-diagonal permeability entries result

$$\mu_{xy} = \mu_{yx} = \frac{1 - \overline{k}_x \overline{\eta}_x \overline{k}_y \overline{\eta}_y}{\overline{k}_x \overline{\eta}_y + \overline{k}_y \overline{\eta}_x}, \tag{5.13}$$

and the transformation-derived material parameters are recovered. Note that this condition corresponds to the condition stipulated by (5.8), which ensures that the transformation device remains impedance matched to its surrounding medium under all plane-wave excitations.

5.5.2 Dual Functional Transformation Electromagnetics Designs

Using an argument similar to the one used to find alternative materials, we can show that a single device can also be designed to behave as two separate transfor-

mation electromagnetics devices for two different plane-wave illuminations. That is, material parameter distributions can be found that support two different electromagnetic field distributions belonging to separate transformation electromagnetics devices.

For a given spatial distribution of wavenumbers and wave impedances, $(\overline{k}_x, \overline{k}_y, \overline{\eta}_x, \overline{\eta}_y)$, matrix equation (5.4) is an under-determined system. Generally, there are two equations and four unknowns $(\mu_{xx}, \mu_{xy}, \mu_{yx}, \mu_{yy})$. Therefore, two more independent equations can be written for a second set of $(\overline{k}_x, \overline{k}_y, \overline{\eta}_x, \overline{\eta}_y)$ corresponding to a different transformation electromagnetics device. In this way, a system with four equations and four unknowns can be obtained.

Let $(\overline{k}_{x1}, \overline{k}_{y1}, \overline{\eta}_{x1}, \overline{\eta}_{y1})$ and $(\overline{k}_{x2}, \overline{k}_{y2}, \overline{\eta}_{x2}, \overline{\eta}_{y2})$ represent the first and second set of wavenumbers and wave impedances, respectively. These are the wavenumber and wave impedance distributions observed in the two different transformation electromagnetics devices under the two different plane-wave illuminations. From them, we can calculate the material parameters needed to support the functionality of both devices under different plane-wave illuminations. Both of these sets must satisfy equations (5.4) and (5.5). The first set is substituted into (5.4) and (5.5), and the equations can be written as follows:

$$\begin{bmatrix} \overline{k}_{y1} \\ \overline{k}_{x1} \end{bmatrix} = \begin{bmatrix} \mu_{xx} & -\mu_{xy} \\ -\mu_{yx} & \mu_{yy} \end{bmatrix} \begin{bmatrix} {\overline{\eta}_{y1}}^{-1} \\ {\overline{\eta}_{x1}}^{-1} \end{bmatrix}, \tag{5.14a}$$

$$\epsilon_z = \frac{\overline{k}_{x1}}{\overline{\eta}_{x1}} + \frac{\overline{k}_{y1}}{\overline{\eta}_{y1}}. \tag{5.14b}$$

Similarly, the second set is substituted into (5.4) and (5.5):

$$\begin{bmatrix} \overline{k}_{y2} \\ \overline{k}_{x2} \end{bmatrix} = \begin{bmatrix} \mu_{xx} & -\mu_{xy} \\ -\mu_{yx} & \mu_{yy} \end{bmatrix} \begin{bmatrix} {\overline{\eta}_{y2}}^{-1} \\ {\overline{\eta}_{x2}}^{-1} \end{bmatrix}, \tag{5.15a}$$

$$\epsilon_z = \frac{\overline{k}_{x2}}{\overline{\eta}_{x2}} + \frac{\overline{k}_{y2}}{\overline{\eta}_{y2}}. \tag{5.15b}$$

Equations (5.14a) and (5.15a) can then be combined to yield

$$\begin{bmatrix} \overline{k}_{y1} & \overline{k}_{y2} \\ \overline{k}_{x1} & \overline{k}_{x2} \end{bmatrix} = \begin{bmatrix} \mu_{xx} & -\mu_{xy} \\ -\mu_{yx} & \mu_{yy} \end{bmatrix} \begin{bmatrix} {\overline{\eta}_{y1}}^{-1} & {\overline{\eta}_{y2}}^{-1} \\ {\overline{\eta}_{x1}}^{-1} & {\overline{\eta}_{x2}}^{-1} \end{bmatrix} \tag{5.16}$$

and the permeability matrix solved for

$$\begin{bmatrix} \mu_{xx} & -\mu_{xy} \\ -\mu_{yx} & \mu_{yy} \end{bmatrix} = \begin{bmatrix} \overline{k}_{y1} & \overline{k}_{y2} \\ \overline{k}_{x1} & \overline{k}_{x2} \end{bmatrix} \begin{bmatrix} {\overline{\eta}_{y1}}^{-1} & {\overline{\eta}_{y2}}^{-1} \\ {\overline{\eta}_{x1}}^{-1} & {\overline{\eta}_{x2}}^{-1} \end{bmatrix}^{-1}. \tag{5.17}$$

It is assumed that the 2×2 matrix consisting of the wave impedances is invertible.

The permittivity can be calculated using either (5.14b) or (5.15b):

$$\epsilon_z = \frac{\overline{k}_{x1}}{\overline{\eta}_{x1}} + \frac{\overline{k}_{y1}}{\overline{\eta}_{y1}} = \frac{\overline{k}_{x2}}{\overline{\eta}_{x2}} + \frac{\overline{k}_{y2}}{\overline{\eta}_{y2}}. \tag{5.18}$$

Strictly speaking, both sets of wavenumbers and wave impedances must have the same permittivity to be seamlessly combined.

Two transformation devices with different permittivity distributions can still be combined into a single device by trading off the inherent reflectionless properties of the individual transformation electromagnetics devices. In this case, the wavenumbers $(\overline{k}_x, \overline{k}_y)$ and the ratio of wave impedances $(\frac{\overline{\eta}_x}{\overline{\eta}_y} = \kappa)$ are maintained in the dual functional device as in the two separate transformation electromagnetics devices. As noted earlier, the ratio of wave impedances at any point in space is representative of

the Poynting vector direction at that point. In order to express the material parameters in terms of this new data set $(\overline{k}_x, \overline{k}_y, \kappa)$, we start by writing (5.4) and (5.5) as follows:

$$\begin{bmatrix} \overline{k}_y \\ \overline{k}_x \end{bmatrix} = \overline{\eta}_x{}^{-1} \begin{bmatrix} \mu_{xx} & -\mu_{xy} \\ -\mu_{yx} & \mu_{yy} \end{bmatrix} \begin{bmatrix} \kappa \\ 1 \end{bmatrix} \tag{5.19a}$$

$$\epsilon_z = \overline{\eta}_x{}^{-1}(\overline{k}_x + \kappa \overline{k}_y), \tag{5.19b}$$

assuming that $\overline{\eta}_x$ is finite. To obtain a system of equations solely consisting of wave numbers and the wave impedance ratios, we rearrange the expression (5.19b) as follows:

$$\overline{\eta}_x{}^{-1} = \frac{\epsilon_z}{(\overline{k}_x + \kappa \overline{k}_y)}. \tag{5.20}$$

Substituting (5.20) into (5.19a) results in

$$\begin{bmatrix} \overline{k}_y \\ \overline{k}_x \end{bmatrix} = \frac{\epsilon_z}{(\overline{k}_x + \kappa \overline{k}_y)} \begin{bmatrix} \mu_{xx} & -\mu_{xy} \\ -\mu_{yx} & \mu_{yy} \end{bmatrix} \begin{bmatrix} \kappa \\ 1 \end{bmatrix}. \tag{5.21}$$

To simplify the notation, let's define the product of the scalar permittivity and permeability tensor as the index tensor

$$\begin{bmatrix} n_{xx} & n_{xy} \\ n_{yx} & n_{yy} \end{bmatrix} = \overline{\mu}\epsilon_z = \begin{bmatrix} \mu_{xx}\epsilon_z & \mu_{xy}\epsilon_z \\ \mu_{yx}\epsilon_z & \mu_{yy}\epsilon_z \end{bmatrix}. \tag{5.22}$$

Using (5.21), (5.22) can be written as

$$\begin{bmatrix} \overline{k}_y(\overline{k}_x + \kappa \overline{k}_y) \\ \overline{k}_x(\overline{k}_x + \kappa \overline{k}_y) \end{bmatrix} = \begin{bmatrix} n_{xx} & -n_{xy} \\ -n_{yx} & n_{yy} \end{bmatrix} \begin{bmatrix} \kappa \\ 1 \end{bmatrix}. \tag{5.23}$$

The equation above consists of solely wavenumbers and the wave impedance ratios. We can now calculate the medium parameters needed to support two different sets: $(\overline{k}_{x1}, \overline{k}_{y1}, \kappa_1)$ and $(\overline{k}_{x2}, \overline{k}_{y2}, \kappa_2)$. Equation (5.23) can be written in terms of the two sets as

$$\begin{bmatrix} \overline{k}_{y1}(\overline{k}_{x1} + \kappa_1 \overline{k}_{y1}) & \overline{k}_{y2}(\overline{k}_{x2} + \kappa_2 \overline{k}_{y2}) \\ \overline{k}_{x1}(\overline{k}_{x1} + \kappa_1 \overline{k}_{y1}) & \overline{k}_{x2}(\overline{k}_{x2} + \kappa_2 \overline{k}_{y2}) \end{bmatrix} = \begin{bmatrix} n_{xx} & -n_{xy} \\ -n_{yx} & n_{yy} \end{bmatrix} \begin{bmatrix} \kappa_1 & \kappa_2 \\ 1 & 1 \end{bmatrix}. \quad (5.24)$$

Solving for the index tensor yields

$$\begin{bmatrix} n_{xx} & -n_{xy} \\ -n_{yx} & n_{yy} \end{bmatrix} = \begin{bmatrix} \overline{k}_{y1}(\overline{k}_{x1} + \kappa_1 \overline{k}_{y1}) & \overline{k}_{y2}(\overline{k}_{x2} + \kappa_2 \overline{k}_{y2}) \\ \overline{k}_{x1}(\overline{k}_{x1} + \kappa_1 \overline{k}_{y1}) & \overline{k}_{x2}(\overline{k}_{x2} + \kappa_2 \overline{k}_{y2}) \end{bmatrix} \begin{bmatrix} \kappa_1 & \kappa_2 \\ 1 & 1 \end{bmatrix}^{-1}, \quad (5.25)$$

where again it has been assumed that the 2×2 matrix of wave impedance ratios is invertible. In summary, (5.25) defines the material parameters (the index tensor) that support two different sets of wavenumbers and wave impedance ratios (Poynting vector directions) under two separate plane-wave illuminations. When these two sets belong to two transformation electromagnetics devices, the resultant dual functional device performs as two separate transformation electromagnetics devices under the different excitations. In order to define the permittivity and permeability individually, a permittivity distribution must be selected first and the permeability distribution found using (5.22). Since the reflectionless property of the transformation electromagnetics is waived for such designs, the overall performance of the dual functional transformation electromagnetics device depends on the amount of impedance mismatch. One can optimize the permittivity distribution ϵ_z in order to minimize these mismatches.

The method described here is a generalization of the methods utilized to simplify the material parameters of the cylindrical cloak in [37] and [100]. One can obtain the same simplified material sets reported in these references using (5.25). To do so, two

sets of wavenumbers and wave impedance ratios $(\overline{k}_x, \overline{k}_y, \kappa)$ of the cylindrical cloak under two different plane-wave illuminations are required.

5.5.3 Relating the Alternative Material Parameters to Coordinate Transformations

In the previous section, alternative material parameters were found assuming the wavenumber and the wave impedance distributions (or their ratios) for plane-wave illuminations. In this section, the wavenumber and wave impedance distributions within the transformation electromagnetics device will be found from the coordinate transformation defining the transformation device and the illuminating field. The alternative material parameters given by (5.10, 5.17, 5.25) will also be rewritten in terms of the coordinate transformation and the illuminating field.

Transformation electromagnetics devices are characterized by coordinate transformations. A point in the original space can be represented by (x, y, z). Under the coordinate transformation, it is transformed to a coordinate (x', y', z') in the transformed space. To be consistent with the previous sections, we will only consider 2D transformations. 2D coordinate transformations from the original space to the transformed space can be written as:

$$x' = x'(x, y), \qquad y' = y'(x, y), \qquad z' = z. \tag{5.26}$$

The Jacobian matrix of the transformation defined by (5.26) can be expressed as:

$$J = \begin{bmatrix} \frac{\partial x'}{\partial x} & \frac{\partial x'}{\partial y} & \frac{\partial x'}{\partial z} \\ \frac{\partial y'}{\partial x} & \frac{\partial y'}{\partial y} & \frac{\partial y'}{\partial z} \\ \frac{\partial z'}{\partial x} & \frac{\partial z'}{\partial y} & \frac{\partial z'}{\partial z} \end{bmatrix} = \begin{bmatrix} J_{11} & J_{12} & 0 \\ J_{21} & J_{22} & 0 \\ 0 & 0 & 1 \end{bmatrix}. \tag{5.27}$$

According to transformation electromagnetics, the material parameters of the trans-

formed space are given by:

$$\bar{\bar{\mu}}' = \bar{\bar{\epsilon}}' = \frac{JJ^T}{|J|}, \tag{5.28}$$

assuming that the original space is free space: $\mu = 1$ and $\epsilon = 1$. For the polarization of interest, the relevant material parameters can be rewritten in terms of the Jacobian matrix entries as,

$$\bar{\bar{\mu}}' = \frac{1}{|J|}\begin{bmatrix} J_{11}^2 + J_{12}^2 & J_{11}J_{21} + J_{12}J_{22} \\ J_{11}J_{21} + J_{12}J_{22} & J_{21}^2 + J_{22}^2 \end{bmatrix}, \tag{5.29a}$$

$$\epsilon_z = \frac{1}{|J|}, \tag{5.29b}$$

where

$$|J| = J_{11}J_{22} - J_{12}J_{21}.$$

is the determinant of the Jacobian matrix (5.27). To remain consistent with the convention used in the previous section, we will remove the prime signs from the quantities belonging to the transformed space hereafter.

The wavenumber distribution $\overline{k}$ at every point in the transformed space can be related to the illuminating plane-wave's wavenumber distribution in the original space $\overline{k}_i$ through the Jacobian matrix:

$$\overline{k} = (J^T)^{-1}\overline{k}_i. \tag{5.30}$$

This equation can be written explicitly in terms of the Jacobian matrix entries:

$$\begin{bmatrix} \overline{k}_x \\ \overline{k}_y \end{bmatrix} = \frac{1}{|J|}\begin{bmatrix} J_{22} & -J_{21} \\ -J_{12} & J_{11} \end{bmatrix}\begin{bmatrix} \overline{k}_{ix} \\ \overline{k}_{iy} \end{bmatrix}. \tag{5.31}$$

The same can be done for the wave impedance within the original and transformed spaces. To derive this relationship, we start by noting that the Jacobian matrix

relates the electric and magnetic field distributions ($\overline{E}$, $\overline{H}$) in the transformed space to the plane-wave illumination ($\overline{E}_i, \overline{H}_i$) in the original space through the following relations:

$$\overline{E} = (J^T)^{-1}\overline{E}_i, \qquad \overline{H} = (J^T)^{-1}\overline{H}_i. \tag{5.32}$$

These relations can be explicitly written in terms of Jacobian matrix entries as follows:

$$\begin{aligned} \overline{E}_z &= \overline{E}_{iz}, \\ \overline{H} = \begin{bmatrix} \overline{H}_x \\ \overline{H}_y \end{bmatrix} &= \frac{1}{|J|} \begin{bmatrix} J_{22} & -J_{21} \\ -J_{12} & J_{11} \end{bmatrix} \begin{bmatrix} \overline{H}_{ix} \\ \overline{H}_{iy} \end{bmatrix}. \end{aligned} \tag{5.33}$$

By using (5.32) and (5.33), the relation between the wave impedances within the transformed space $\overline{\eta}$ and wave impedances of the illuminating field in the original space $\overline{\eta}_i$ can be written as:

$$\overline{\eta}^{-1} = \frac{J}{|J|}\overline{\eta}_i{}^{-1}. \tag{5.34}$$

Recasting (5.34) in terms of Jacobian matrix entries results in

$$\begin{bmatrix} \overline{\eta}_x{}^{-1} \\ \overline{\eta}_y{}^{-1} \end{bmatrix} = \frac{1}{|J|} \begin{bmatrix} J_{11} & J_{12} \\ J_{21} & J_{22} \end{bmatrix} \begin{bmatrix} \overline{\eta}_{xi}{}^{-1} \\ \overline{\eta}_{yi}{}^{-1} \end{bmatrix}. \tag{5.35}$$

Equations (5.31) and (5.35) show how to calculate the wavenumbers and wave impedances, ($\overline{k}_x, \overline{k}_y, \overline{\eta}_x, \overline{\eta}_y$), for a given coordinate transformation (5.27) and plane-wave illumination denoted by wavenumbers and wave impedances, ($\overline{k}_{ix}, \overline{k}_{iy}, \overline{\eta}_{ix}, \overline{\eta}_{iy}$).

Now, we can write the alternative material parameters (5.10) in terms of the coordinate transformation (5.27), and a plane-wave illumination with a propagation angle θ with respect to x axis. The plane wave is represented by normalized wavenumbers,

$(\overline{k}_{ix}, \overline{k}_{iy}) = (\cos\theta, \sin\theta)$ and wave impedances, $(\overline{\eta}_{ix}, \overline{\eta}_{iy}) = (\frac{1}{\cos\theta}, \frac{1}{\sin\theta})$, in the original space. Using (5.31), the wavenumbers $(\overline{k}_x, \overline{k}_y)$ in the transformed space can be written as

$$\begin{bmatrix} \overline{k}_x \\ \overline{k}_y \end{bmatrix} = \frac{1}{|J|} \begin{bmatrix} J_{22} & -J_{21} \\ -J_{12} & J_{11} \end{bmatrix} \begin{bmatrix} \cos\theta \\ \sin\theta \end{bmatrix}. \tag{5.36}$$

Using (5.35), the wave impedances $(\overline{\eta}_x, \overline{\eta}_y)$ in the transformed space can be written as

$$\begin{bmatrix} \overline{\eta}_x{}^{-1} \\ \overline{\eta}_y{}^{-1} \end{bmatrix} = \frac{1}{|J|} \begin{bmatrix} J_{11} & J_{12} \\ J_{21} & J_{22} \end{bmatrix} \begin{bmatrix} \cos\theta \\ \sin\theta \end{bmatrix}. \tag{5.37}$$

Substituting (5.36) and (5.37) into (5.10a), yields the alternative material parameters in terms of the coordinate transformation and illuminating field:

$$\begin{aligned} \mu_{xx} &= \frac{J_{11}\sin\theta - J_{12}\cos\theta}{J_{21}\cos\theta + J_{22}\sin\theta} + \frac{J_{11}\cos\theta + J_{12}\sin\theta}{J_{21}\cos\theta + J_{22}\sin\theta}\mu_{xy}, \\ \mu_{yy} &= \frac{J_{22}\cos\theta - J_{21}\sin\theta}{J_{11}\cos\theta + J_{12}\sin\theta} + \frac{J_{21}\cos\theta + J_{22}\sin\theta}{J_{11}\cos\theta + J_{12}\sin\theta}\mu_{yx}, \\ \epsilon_z &= \frac{1}{|J|}, \end{aligned} \tag{5.38}$$

where again μ_{xy} and μ_{yx} are free parameters. In addition, (5.10b) and (5.10c) can be written in similar way. In summary, (5.38) presents alternative material parameters to those given by (5.29). The transformation electromagnetics device with alternative material parameters, however, only works for a plane-wave illumination with a propagation angle θ with respect to the x axis.

The material parameters derived for dual functional devices, (5.17) and (5.25), can also be related to the coordinate transformation and illuminating field. Let's assume that the two transformation electromagnetics devices to be combined into a

single device are represented by the following coordinate transformations:

$$\begin{aligned} &(a) \quad x_1{}' = x_1{}'(x,y), \qquad y_1{}' = y_1{}'(x,y), \qquad z_1{}' = z_1. \\ &(b) \quad x_2{}' = x_2{}'(x,y), \qquad y_2{}' = y_2{}'(x,y), \qquad z_2{}' = z_2. \end{aligned} \tag{5.39}$$

Let their respective Jacobian matrices be represented by

$$(a) \;\; J = \begin{bmatrix} J_{11} & J_{12} & 0 \\ J_{21} & J_{22} & 0 \\ 0 & 0 & 1 \end{bmatrix}, \qquad (b) \;\; \widetilde{J} = \begin{bmatrix} \tilde{J}_{11} & \tilde{J}_{12} & 0 \\ \tilde{J}_{21} & \tilde{J}_{22} & 0 \\ 0 & 0 & 1 \end{bmatrix}. \tag{5.40}$$

Using (5.36) and (5.37), we can write wavenumbers and wave impedances in the transformed space in terms of the illuminating fields and the Jacobian matrices of the transformations (5.40). Let's further assume that the dual functional device behaves as the first transformation electromagnetics device (5.40a), under a plane-wave illumination with a propagation angle θ_1. The illuminating plane wave is represented by wavenumbers $(\overline{k}_{ix}, \overline{k}_{iy}) = (\cos\theta_1, \sin\theta_1)$ and $(\overline{\eta}_{ix}, \overline{\eta}_{iy}) = (\frac{1}{\cos\theta_1}, \frac{1}{\sin\theta_1})$. For this illumination, (5.36) and (5.37) become:

$$\begin{aligned} \begin{bmatrix} \overline{k}_{1x} \\ \overline{k}_{1y} \end{bmatrix} &= \frac{1}{|J|} \begin{bmatrix} J_{22} & -J_{21} \\ -J_{12} & J_{11} \end{bmatrix} \begin{bmatrix} \cos\theta_1 \\ \sin\theta_1 \end{bmatrix}, \\ \begin{bmatrix} \overline{\eta}_{1x}^{-1} \\ \overline{\eta}_{1y}^{-1} \end{bmatrix} &= \frac{1}{|J|} \begin{bmatrix} J_{11} & J_{12} \\ J_{21} & J_{22} \end{bmatrix} \begin{bmatrix} \cos\theta_1 \\ \sin\theta_1 \end{bmatrix}. \end{aligned} \tag{5.41}$$

The dual functional device behaves as a different transformation electromagnetics device (5.40b) under a plane-wave illumination with a propagation angle θ_2. The illuminating field is represented by wavenumbers $(\overline{k}_{ix}, \overline{k}_{iy}) = (\cos\theta_2, \sin\theta_2)$ and $(\overline{\eta}_{ix}, \overline{\eta}_{iy}) =$

$(\frac{1}{\cos\theta_2}, \frac{1}{\sin\theta_2})$. For this illumination, (5.36) and (5.37) simplify to:

$$\begin{bmatrix} \overline{k}_{2x} \\ \overline{k}_{2y} \end{bmatrix} = \frac{1}{|\widetilde{J}|} \begin{bmatrix} \tilde{J}_{22} & -\tilde{J}_{21} \\ -\tilde{J}_{12} & \tilde{J}_{11} \end{bmatrix} \begin{bmatrix} \cos\theta_2 \\ \sin\theta_2 \end{bmatrix},$$
$$\begin{bmatrix} \overline{\eta}_{2x}^{-1} \\ \overline{\eta}_{2y}^{-1} \end{bmatrix} = \frac{1}{|\widetilde{J}|} \begin{bmatrix} \tilde{J}_{11} & \tilde{J}_{12} \\ \tilde{J}_{21} & \tilde{J}_{22} \end{bmatrix} \begin{bmatrix} \cos\theta_2 \\ \sin\theta_2 \end{bmatrix}. \tag{5.42}$$

Substituting $(\overline{k}_{x1}, \overline{k}_{y1}, \overline{\eta}_{x1}, \overline{\eta}_{y1})$ from (5.41) and $(\overline{k}_{x2}, \overline{k}_{y2}, \overline{\eta}_{x2}, \overline{\eta}_{y2})$ from (5.42) into (5.17) and (5.18) results in the material parameters for dual functional device in terms of coordinate transformation and plane-wave illumination:

$$\begin{bmatrix} \mu_{xx} & -\mu_{xy} \\ -\mu_{yx} & \mu_{yy} \end{bmatrix} = \begin{bmatrix} \frac{J_{11}\sin\theta_1 - J_{12}\cos\theta_1}{|J|} & \frac{\tilde{J}_{11}\sin\theta_2 - \tilde{J}_{12}\cos\theta_2}{|\widetilde{J}|} \\ \frac{J_{22}\cos\theta_1 - J_{21}\sin\theta_1}{|J|} & \frac{\tilde{J}_{22}\cos\theta_2 - \tilde{J}_{21}\sin\theta_2}{|\widetilde{J}|} \end{bmatrix} \tag{5.43}$$
$$\begin{bmatrix} \frac{J_{21}\cos\theta_1 + J_{22}\sin\theta_1}{|J|} & \frac{\tilde{J}_{21}\cos\theta_2 + \tilde{J}_{22}\sin\theta_2}{|\widetilde{J}|} \\ \frac{J_{11}\cos\theta_1 + J_{12}\sin\theta_1}{|J|} & \frac{\tilde{J}_{11}\cos\theta_2 + \tilde{J}_{12}\sin\theta_2}{|\widetilde{J}|} \end{bmatrix}^{-1}$$
$$\epsilon_z = \frac{1}{|J|} = \frac{1}{|\widetilde{J}|}. \tag{5.44}$$

In a similar way, the index tensor (5.25) can be written in terms of the coordinate transformation and the plane-wave illumination given by (5.36) and (5.37):

$$\begin{bmatrix} n_{xx} & -n_{xy} \\ -n_{yx} & n_{yy} \end{bmatrix} = \begin{bmatrix} \frac{J_{11}\sin\theta_1 - J_{12}\cos\theta_1}{|J|(J_{11}\cos\theta_1 + J_{12}\sin\theta_1)} & \frac{\tilde{J}_{11}\sin\theta_2 - \tilde{J}_{12}\cos\theta_2}{|\widetilde{J}|(\tilde{J}_{11}\cos\theta_2 + \tilde{J}_{12}\sin\theta_2)} \\ \frac{J_{22}\cos\theta_1 - J_{21}\sin\theta_1}{|J|(J_{11}\cos\theta_1 + J_{12}\sin\theta_1)} & \frac{\tilde{J}_{22}\cos\theta_2 - \tilde{J}_{21}\sin\theta_2}{|\widetilde{J}|(\tilde{J}_{11}\cos\theta_2 + \tilde{J}_{12}\sin\theta_2)} \end{bmatrix} \tag{5.45}$$
$$\begin{bmatrix} \frac{J_{21}\cos\theta_1 + J_{22}\sin\theta_1}{J_{11}\cos\theta_1 + J_{12}\sin\theta_1} & \frac{\tilde{J}_{21}\cos\theta_2 + \tilde{J}_{22}\sin\theta_2}{\tilde{J}_{11}\cos\theta_2 + \tilde{J}_{12}\sin\theta_2} \\ 1 & 1 \end{bmatrix}^{-1}$$

5.6 Full-wave Verification

In this section, we demonstrate the performance of transformation devices designed using alternative material parameters as well as dual functional transformation electromagnetic devices. The reported simulations were performed using the commercial finite element solver, Comsol Multiphysics.

Three cases are considered. First, a transformation electromagnetics device with alternative material parameters is shown to operate the same as the transformation electromagnetics device with transformed material parameters for a particular plane-wave illumination. Second, a dual functional device combining two transformation electromagnetics devices with the same permittivity profile is designed and simulated. Finally, a dual functional device combining two transformation electromagnetics devices with different permittivity profiles is demonstrated.

This section begins with a short review of the two transformation devices considered in this section: an electromagnetic field rotator and a cylindrical electromagnetic field concentrator.

5.6.1 Electromagnetic Field Rotator

An electromagnetic field rotator is a transformation electromagnetics region that rotates an incident electromagnetic field by a prescribed angle within a defined annulus [41]. The transformation domain for such a device is circular and its coordinate transformation in cylindrical coordinates is:

$$\begin{aligned} r' &= r, \\ \phi' &= \begin{cases} \phi + \phi_o \frac{R_2 - r}{R2 - R1} & R_1 < r < R_2, \\ \phi + \phi_o & r < R_1, \end{cases} \\ z' &= z, \end{aligned} \tag{5.46}$$

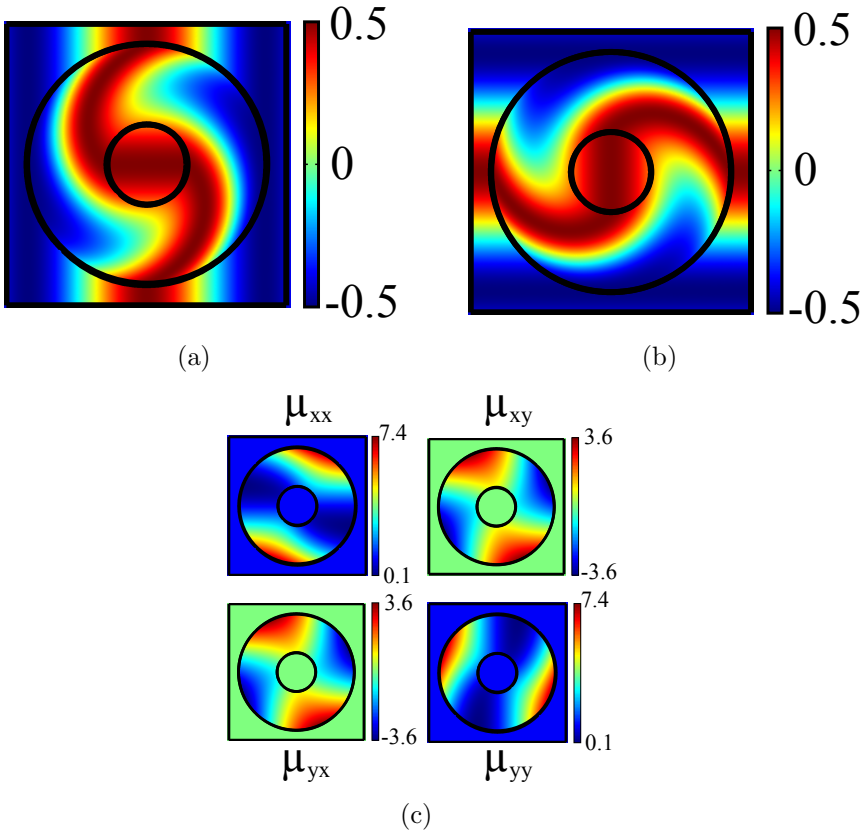

Figure 5.16: A steady state snapshot in time of vertical electric field within and surrounding an electromagnetic field rotator. (a) The field distribution for a plane-wave illumination along the x direction. (b) The field distribution for a plane-wave illumination along the y direction. (c) The permeability distribution. The permittivity value is equal to that of free space.

where R_1 and R_2 are the radii of the inner and outer concentric circles, respectively. The constant ϕ_o is the angle of field rotation observed within the inner circle. The transformed material parameters derived using the transformation electromagnetics method (5.29) are:

$$\overline{\mu} = R(\phi') \begin{bmatrix} 1 & -t \\ -t & 1+t^2 \end{bmatrix} R(\phi')^T, \qquad \epsilon_z = 1 \quad (R_1 < r' < R_2), \tag{5.47}$$

$$\mu = 1, \qquad \epsilon_z = 1 \quad (r' < R_1). \tag{5.48}$$

where

$$R(\phi') = \begin{bmatrix} \cos\phi' & -\sin\phi' \\ \sin\phi' & \cos\phi' \end{bmatrix}, \qquad t = \frac{r'\phi'_o}{R_2 - R_1}.$$

The radii of the inner and outer circles of the field rotators considered are assumed to be $0.17\lambda_o$ and $0.51\lambda_o$ respectively, where λ_o is the free-space wavelength at 3 GHz. Fig. 5.16 shows the performance of an electromagnetic field rotator. Fig. 5.16(a) and Fig. 5.16(b) depict the vertical (out of plane) electric field within and surrounding the field rotator when illuminated by a plane wave propagating in the x (horizontal) and y (vertical) directions, respectively. The field rotator, implemented with the transformed material parameters (5.47) shown in Fig. 5.16(c), performs a 90 degree field rotation independent of illumination direction.

5.6.2 Cylindrical Electromagnetic Field Concentrator

A cylindrical electromagnetic field concentrator concentrates the field of an incoming plane wave into a prescribed circular region [101]. The coordinate transformation for such a device is also defined over a circular region:

$$r' = \begin{cases} \frac{R_1}{R_2} r & 0 \le r \le R_2 \\ \frac{R_3 - R_1}{R_3 - R_2} r - \frac{R_2 - R_1}{R_3 - R_2} R_3 & R_2 \le r \le R_3, \end{cases}$$

$$\phi' = \phi, \tag{5.49}$$

$$z' = z, \tag{5.50}$$

where R_1 and R_3 are the inner and outer radii of two concentric circles. The variable R_2 is the radius of an intermediate circle that is used as a design parameter. The material parameters resulting from the transformation above are:

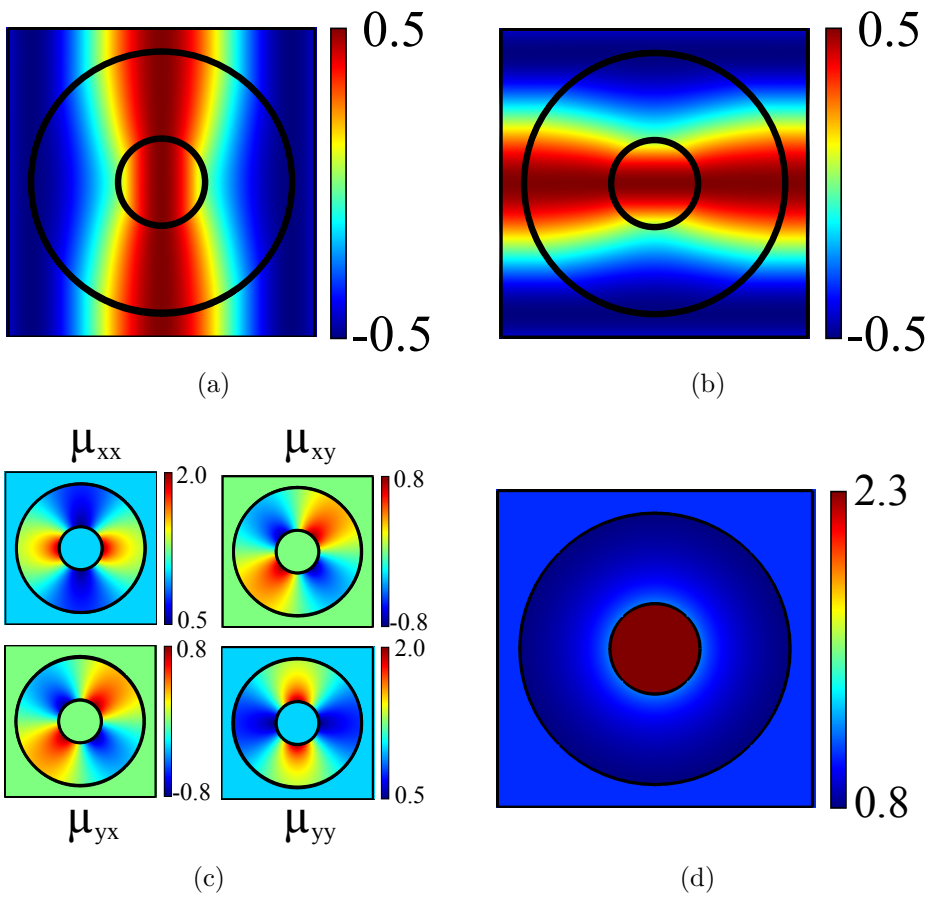

Figure 5.17: A steady state snapshot in time of vertical electric field within and surrounding the cylindrical field concentrator. (a) The field distribution for a plane-wave illumination along the x direction (b) The field distribution for a plane-wave illumination along the y direction. (c) The permeability distribution. (d) The permittivity distribution.

$$\overline{\mu} = R(\phi') \begin{bmatrix} \eta & 0 \\ 0 & \frac{1}{\eta} \end{bmatrix} R(\phi')^T, \qquad \epsilon_z = \frac{\eta}{\beta}, \qquad (R_1 < r' < R_3),$$

$$\mu = 1, \qquad \epsilon_z = (\frac{R_2}{R_1})^2, \qquad (r' < R_1). \tag{5.51}$$

where

$$\eta = (1 + \frac{e}{f}\frac{R_3}{r'}), \qquad \beta = \frac{h}{f},$$
$$e = R_2 - R_1, \qquad f = R_3 - R_2, \qquad h = R_3 - R_1.$$

The geometric dimensions of the field concentrator considered were chosen to be the same as for the field rotator. The radii of the inner, intermediate and outer circles were selected to be $0.17\lambda_o$, $0.26\lambda_o$ and $0.51\lambda_o$, where λ_o is the free-space wavelength at 3 GHz. Fig. 5.17 shows the performance of an electromagnetic field concentrator. Fig. 5.17(a) and Fig. 5.17(b) depict the vertical (out of plane) electric field within and surrounding the electromagnetic field concentrator when illuminated by a plane wave propagating in the x (horizontal) and y (vertical) directions. The permeability and permittivity distributions for the device are shown in Fig. 5.17(c) and Fig. 5.17(d), respectively.

5.6.3 Field Rotator with Alternative Material Parameters

Here, we compare the simulated performance of a field rotator implemented with the transformed material parameters (see Fig. 5.16) to that of the field rotator with alternative material parameters. We consider two examples. The goal of the first example is to demonstrate that alternative material parameters can replace the transformed material parameters at arbitrary locations within the device. The patches in Fig. 5.18(a) are replaced with materials possessing alternative material parameters. The alternative material parameters within the square patches are calculated using (5.38) for a plane-wave incident at $\theta = 0$ degree (along the x axis) and assuming $\mu_{xy} = \mu_{yx} = 0$. Fig. 5.18(c) shows the alternative material parameter distributions. Fig. 5.18(a) shows the simulated performance of the field rotator with alternative parameters for a plane-wave illumination in the x-direction. For a plane wave in-

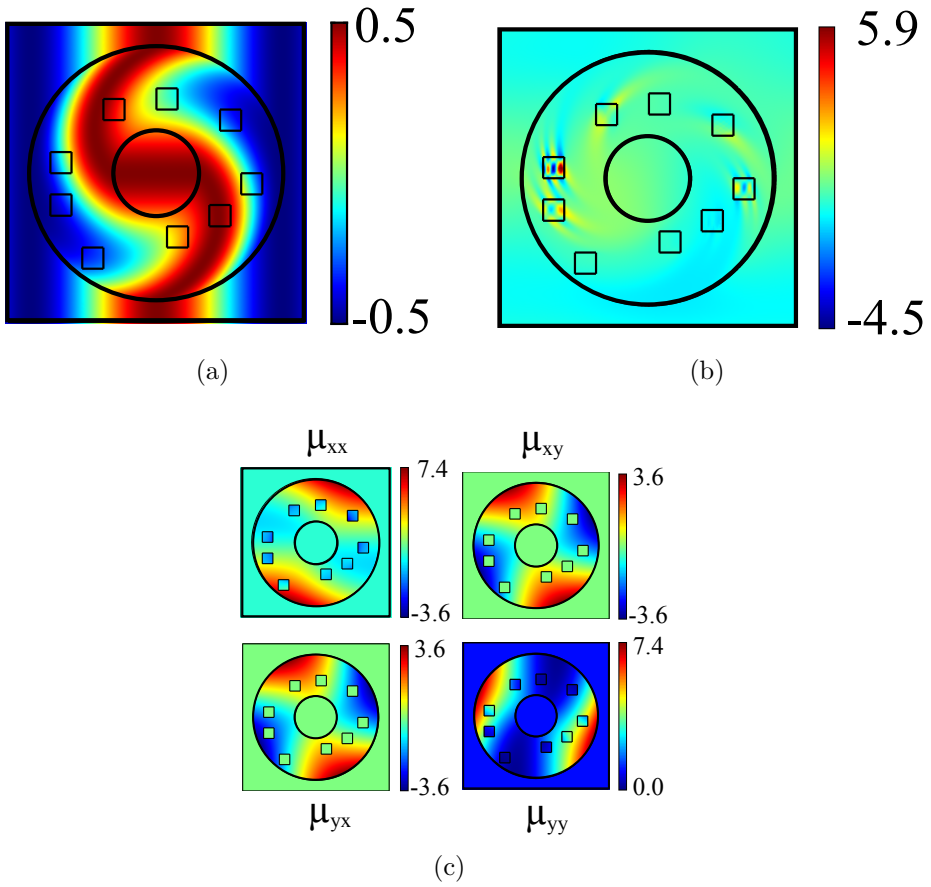

Figure 5.18: A steady state snapshot in time of vertical electric field within and surrounding the field rotator employing alternative material parameters. The patches are replaced with alternative material parameters. (a) The field distribution for a plane-wave illumination along the x direction. (b) The field distribution for a plane-wave illumination along the y direction. (c) The alternative material parameter (permeability) distribution. The permittivity is equal to that of free space.

cidence along the x direction, the field rotator performs exactly as it should (see Fig. 5.16(a)). However, since the alternative material parameters are found for a plane-wave illumination along the x direction, the device does not work for other plane-wave illuminations. Fig. 5.18(b) shows the field distribution for a plane-wave incidence along the y direction. It is clear that the device does not function as a field rotator as for such a plane-wave illumination.

The second example shows that alternative material parameters can be used to reduce anisotropy, while producing the exactly same field pattern. Fig. 5.19(a) shows

the alternative material parameters over the annulus of the field rotator. These alternative material parameters were calculated using (5.12) for a plane wave incident along the x axis. They are used to replace the transformed material parameters over the entire annulus. Fig. 5.19(b) compares the dispersion curves for the transformed (black ellipses) and alternative material parameters (red ellipses) at a number of points within the annulus. Fig. 5.19(c) and Fig. 5.19(d) show the simulated performance of the field rotator with the alternative parameters given in Fig. 5.19(a). Once again, for a plane wave incidence along the x direction, the field rotator performs as it should (see Fig. 5.16(a)). However, since the alternative material parameters are found for a plane-wave illumination along the x direction, the device does not work for other plane-wave illuminations. Fig. 5.19(d) shows the field distribution for a plane-wave incidence along the y direction. Clearly, the device does not function as a field rotator for such a plane-wave illumination.

5.6.4 Dual Functional Device: Combining Field Rotators with Different Rotation Angles

In this section, we verify that two transformation electromagnetics devices with the same permittivity profile can be combined. We designed a field rotator that rotates the incident field by 90 degrees when illuminated along x direction and rotates it by 45 degrees when the illuminated along y direction.

For such a design, the required material parameters are given by (5.43) and (5.44). In these equations, the angles were set to $\theta_1 = 0$ degree and $\theta_2 = 90$ degrees representing the plane wave illuminations along x and y directions, respectively. The coordinate transformations for the field rotators are given by (5.46) with $\phi_o = 90$ degrees and $\phi_o = 45$ degrees, representing two field rotators with distinct rotational angles.

The permeability values calculated using (5.43) are plotted in Fig. 5.20(c). The

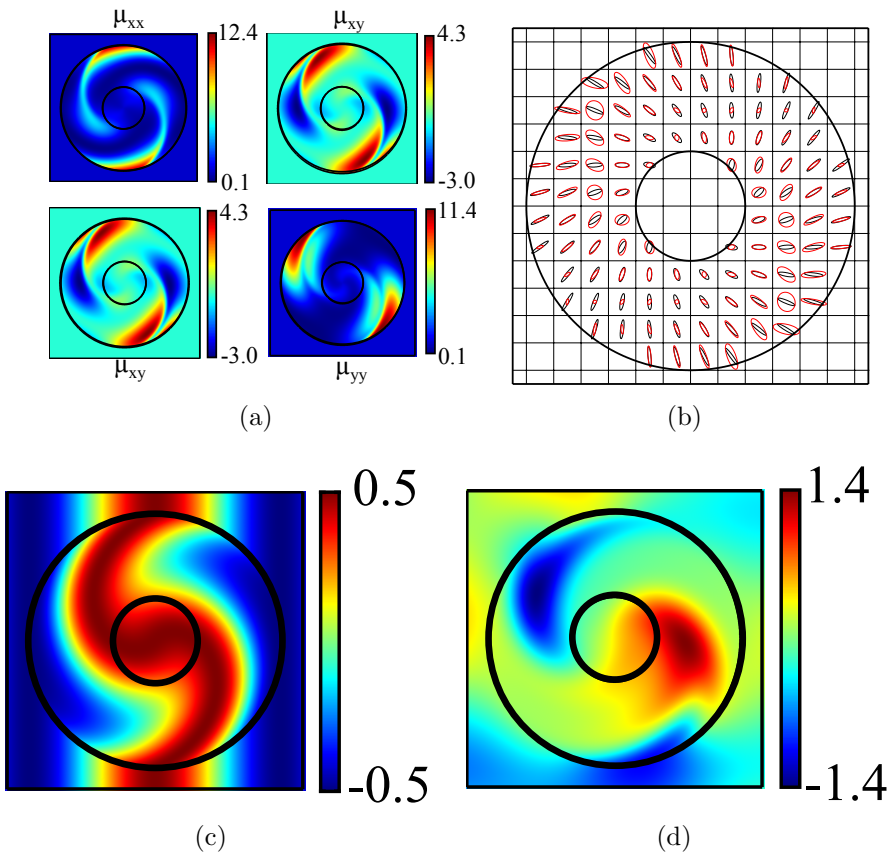

Figure 5.19: A steady-state snapshot in time of the vertical electric field within and surrounding the field rotator employing alternative material parameters that exhibit minimal anisotropy. (a) The alternative material parameter (permeability) distribution. The permittivity is equal to that of free space. (b) Dispersion curves of the transformed (black) and alternative material parameters (red) within the annulus. (c) The field distribution for a plane-wave illumination along the x direction. (d) The field distribution for a plane-wave illumination along the y direction.

permittivity value of the dual functional device is equal to that of free space and is the same for both field rotators. The simulated performance of the designed dual functional transformation electromagnetics device is depicted in Fig. 5.20(a) and Fig. 5.20(b). For a plane wave illumination along the x direction, the field rotator exhibits exactly 90 degrees of rotation and for a plane wave illumination along the y direction, the field rotator exhibits 45 degrees of rotation.

Fig. 5.21(a) and Fig. 5.21(b) show the response of the designed dual functional transformation electromagnetics device for a plane wave illumination between the

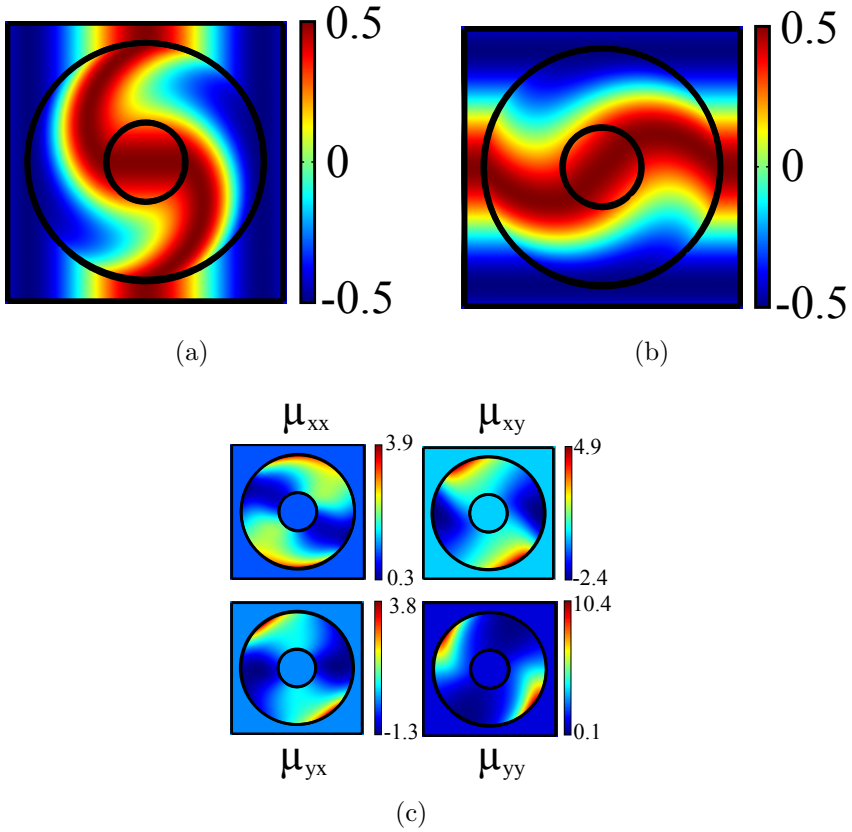

Figure 5.20: A steady-state snapshot in time of the vertical electric field and surrounding the dual functional device combining two field rotators with distinct rotational angles. (a) The field distribution for a plane wave illumination along the x direction. A field rotation of 90 degrees is observed. (b) The field distribution for a plane wave illumination along the y direction. A field rotation of 45 degrees is observed. (c) The permeability distribution. The permittivity value is equal to that of free space.

horizontal and vertical directions. In both figures, the arrows show the power flow directions within and surrounding the device. For directions in between, the designed device is not perfectly impedance-matched. To quantify the amount of mismatch, the radar cross section (RCS) of the device was simulated as a function of incidence angle, and is shown in Fig. 5.21(c). Despite the mismatches, it still performs an angular rotation of the incoming field as a function of incidence angle. In Fig. 5.21(a), the incidence angle is 30 degrees and the field undergoes a rotation of 75 degrees at the center of the device. In Fig. 5.21(b), the incidence angle is 60 degrees and the field

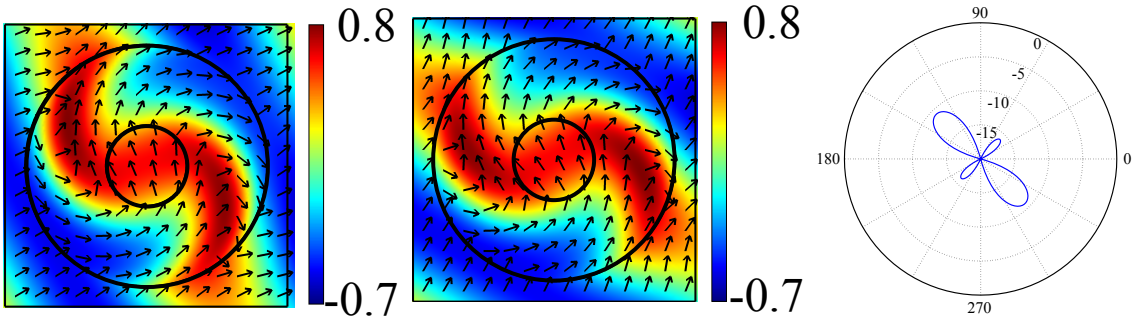

(a) (b) (c)

Figure 5.21: A steady-state snapshot in time of the vertical electric field and surrounding the dual functional device combining two field rotators with distinct rotational angles. Power flow directions are shown with vectors. (a) The field distribution for a plane wave illumination at 30 degree. A rotation of 75 degrees is observed at the center of the device. (b) The field distribution for a plane wave illumination at 60 degrees. A rotation of 30 degrees is observed at the center of the device. (c) RCS (dB) as a function of incidence angle. RCS is minimum for design angles, i.e. 0 (180) and 90 (270) degrees.

undergoes a rotation of 30 degrees at the center of the device. Based on the device's performance depicted in Fig. 5.20 and Fig. 5.21, the angle of rotation decreases linearly with incident angle:

$$\theta_{rot} = \frac{180 - \theta_{inc}}{2} \tag{5.52}$$

where θ_{rot} and θ_{inc} are the rotational and the incidence angle in degrees, respectively.

5.6.5 Dual Functional Device: Combining a Field Rotator and a Field Concentrator

In this section, we verify that two transformation electromagnetics devices with different permittivity profiles can be combined. We design a dual functional device that behaves as a field rotator (with 30 degrees of rotation) when illuminated along the x (horizontal) direction, and a field concentrator when illuminated at an angle

of -60 degrees. The inner and outer radii of two concentric circles are the same as before, $0.17\lambda_o$ and $0.51\lambda_o$, respectively.

The coordinate transformation of the field rotator is given by (5.46) with a rotation angle of $\phi_o = 30$ degrees. The transformation of the field concentrator is given by (5.49). The material parameters for such a device are calculated using (5.45). In (5.45), the angles are chosen to be $\theta_1 = 0$ degree and $\theta_2 = -60$ degrees, representing plane wave illuminations along the x axis and -60 degrees directions, respectively.

Once the index tensor was calculated, an average value for the permittivity was assumed. Over the annulus, we assumed permittivity values equal to the square root of the sum of both device's original permittivity values. Inside the inner circle, the original permittivity values of the concentrator were used (see Fig. 5.17(d)). The permittivity distribution of the dual functional device is depicted in Fig. 5.22(a). From this this permittivity profile, the permeability distribution of the dual functional device was found, and is shown in Fig. 5.22(b).

The performance of the combined dual functional device is depicted in Fig. 5.23. Fig. 5.23(a) shows the vertical (out of plane) electric field within and surrounding the dual functional device, when illuminated by a plane wave propagating in the x (horizontal) direction. Fig. 5.23(b) depicts the vertical (out of plane) electric field within and surrounding the dual functional device when illuminated by a plane wave propagating at -60 degrees. The vectors show the power flow direction. In summary, the combined device operates as a field rotator in Fig. 5.23(a) and as a field concentrator in Fig. 5.23(b) for two different directions of illumination. The dual functional device, whose performance is shown in Fig. 5.23, is not impedance-matched to the outer medium for either incident angle. To show the mismatch amount, RCS of the device was simulated as a function of incidence angle and it is shown in Fig. 5.23(c). This is the trade-off that must be made when two devices with different permittivity profiles are combined. Given that the impedance mismatch depends on

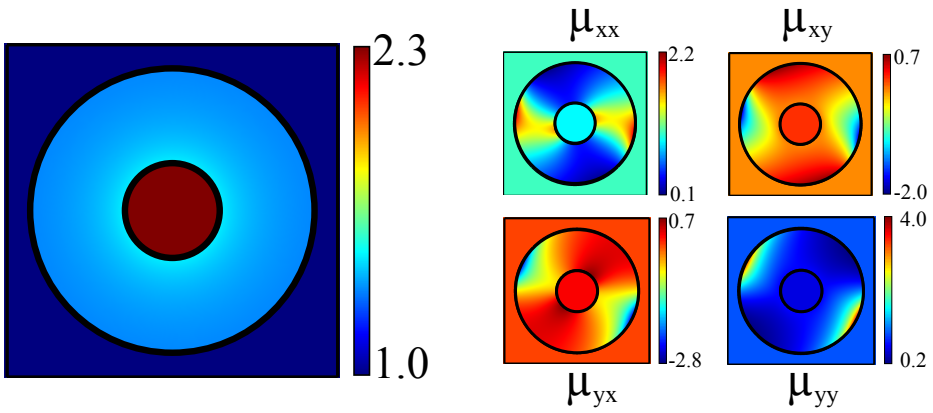

(a) (b)

Figure 5.22: Material parameters of the dual functional device combing a field rotator and a field concentrator. (a) Permittivity distribution. Over the annulus, it is the square root of the sum of both device's original permittivity values. Inside the inner circle, transformed permittivity values of the field concentrator are used. (b) The permeability distribution.

the permittivity distribution, one can optimize it to minimize reflections.

5.7 Applications

Since the proposed design approach provides independent spatial control of phase progression and power flow, it will enable scattered or impressed currents on arbitrarily contoured surfaces, such as those of buildings, aircraft, vehicles, optical circuits and other platforms, to be arbitrarily directed and controlled. Ultimately, the design approach will enable the arbitrary (within the constraints imposed by Maxwell's equations) control of fields on arbitrary surfaces.

The proposed method's ability to control power and phase flow as well as to establish arbitrary aperture distributions, immediately reveals its use in the design of beam-former and antenna designs. For example, in antenna design, one may wish to control power flow across an aperture in order to realize a given amplitude distribution (beam shape), while at the same time control phase progression to establish a certain beam-pointing direction. In the case of a beam-former, one may wish to stipulate

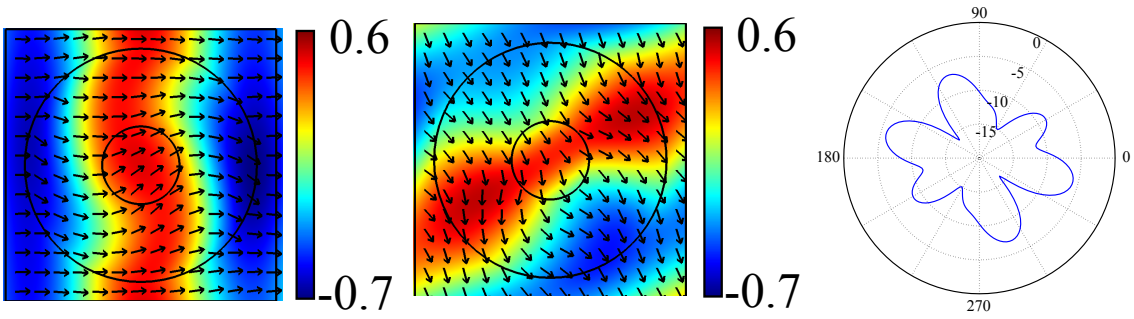

(a) (b) (c)

Figure 5.23: A steady-state snapshot in time of the vertical electric field within and surrounding the dual functional device combining a field rotator and a field concentrator. The device acts as either a field rotator and field concentrator. Power flow directions are shown with vectors. (a) The field distribution for a plane wave illumination along the x direction. A field rotation of 30 degrees is observed. (b) The field distribution for a plane wave illumination at -60 degree. Field concentration is observed. (c) RCS (dB) as a function of incidence angle.

an input field distribution (excitation) and an output field distribution (amplitude and phase distribution of the antenna elements), with a transition from one to the other. Therefore, spatial control of phase and power flow allows one to independently sculpt the phase and amplitude of a field profile, leading to antenna and beam former designs with desired characteristics. Furthermore, the proposed method can find application in holography [102, 103] and scattering control [104, 105] for controlling radar signature and electromagnetically concealing objects. In addition, the method could provide a novel approach to signal routing such as controlling electromagnetic field flow on optical circuits, the design of mode conversion devices [106] for converting a field profile from one form to another. Using the method, the generation of extreme antenna apertures can be realized. These extreme aperture fields can be used for super-directive radiation [107] with the purpose of high-resolution far field focusing and detection. The excitation of Airy [108, 109, 110, 111] and Bessel beams [112, 113, 114, 115] are also possible, and these beams can resist diffractive spreading for non-destructive evaluation, covert communication and microscopy.

5.8 Conclusion

This chapter presented a method for controlling the power flow and phase progression of electromagnetic fields in two dimensions. The method enables the design of reflectionless, inhomogeneous, anisotropic media that can support prescribed spatial distributions of the wave vector and Poynting vector direction. This spatial control of phase and power flow allows the amplitude and phase of a field profile to be tailored arbitrarily. Specific examples were reported which show how the proposed method can be used to tailor the field radiated by a cylindrical source into desired amplitude and phase profiles. The relationship between the proposed method and transformation electromagnetics was also drawn. It was shown that the proposed method can be used to find alternative material parameters for transformation electromagnetic devices, and to design dual functional transformation electromagnetic devices. Potential uses of the proposed method in the design of guiding and radiating structures were also discussed.

Metamaterials can be employed to realize the anisotropic, inhomogeneous materials required in the proposed design approach. At microwave and millimeter-wave frequencies, tensor transmission-line metamaterials are particularly well-suited for the implementation of TM_z polarized devices. At optical frequencies, plasmonic/dielectric metamaterials [116, 117, 118, 119] and the concept of nanocircuit elements [71] could be employed.

CHAPTER VI

Summary and Future Work

6.1 Summary

The aims of this thesis have been to develop electromagnetically anisotropic, inhomogeneous materials using circuit networks and devise methods to control electromagnetic fields using these materials. These anisotropic, inhomogeneous materials and synthesis methods are crucial to the development of novel electromagnetic devices for radiated and guided wave applications.

In Chapter 2, the theory of transmission-line based metamaterials was generalized to develop tensor transmission-line metamaterials. These metamaterials are 2D circuit equivalents of homogeneous, anisotropic media with a 2×2 permeability tensor and a permittivity scalar. In contrast to earlier transmission-line based metamaterials, tensor transmission-line metamaterials can synthesize full material tensors in the Cartesian bases, and thus can be used to design transformation electromagnetic devices. To aid in design, analytical methods for design and analysis of the tensor transmission-line metamaterials were proposed. Subsequently, tensor transmission-line metamaterials were used in the design of two transformation electromagnetic devices, an invisibility cloak and a field rotator, to demonstrate their ability to tailor electromagnetic waves in extreme and unprecedented ways. In order to realize the proposed metamaterials at microwave frequencies, a microstrip implementation was

proposed. The anisotropic properties of the implemented tensor transmission-line metamaterials were verified through full-wave simulation. Circuit and full-wave simulations validated the analysis of tensor transmission-line metamaterials, and showed their ability to manipulate electromagnetic waves in extreme and unprecedented ways.

In Chapter 3, a rigorous homogenization method for finding the effective material parameters (tensorial permeability and a scalar permittivity) of implemented tensor transmission-line metamaterials was presented. The method utilized a local field averaging procedure on the metamaterial's unit cell to compute its effective material parameters. The proposed homogenization method provided accurate and rapid characterization of tensor transmission-line metamaterials in terms of effective material parameters.

In Chapter 4, tensor transmission-line metamaterials were used in the design of a transformation electromagnetics device for guided waves: a beam-shifting slab. The device was fabricated and tested at microwave frequencies. This work experimentally verified the anisotropic behavior of tensor transmission-line metamaterials as well as the homogenization procedure used to extract material parameters. Further, it experimentally demonstrated the suitability of using tensor metamaterials to design transformation electromagnetics devices. The development of tensor transmission-line metamaterials has encouraged the use of these metamaterials to implement larger and more complex devices that are both anisotropic and inhomogeneous.

In Chapter 5, a distinct method for arbitrarily controlling the phase progression and power flow of electromagnetic fields within a region of space was proposed. This method involved prescribing phase and power distributions within a discretized medium. It exploited an anisotropic medium's ability to support power flow and phase progression in different directions. The proposed method has proven useful in establishing aperture field profiles with arbitrary phase and amplitude distributions, which could revolutionize beam-former and antenna design. In the considered design

examples, the field of a cylindrical source was tailored to generate apertures with arbitrary phase and amplitude distributions. Beam-formers, which can create arbitrary aperture field distributions (phase and amplitude) were reported. This method was also related to the transformation electromagnetics design strategy in order to define alternative material parameters for transformation devices, and design dual-function transformation devices.

6.2 Future Work

This research work has developed the necessary tools for designing anisotropic, inhomogeneous media for controlling electromagnetic fields. However, there are several aspects of the research that deserve further attention.

6.2.1 Realization of the Antenna Beam-former

The simulated beam-former in Chapter 5 can be developed into a practical antenna beam-former. The results in Chapter 5 demonstrate that by laterally displacing the cylindrical source of the collimator allows the emerging beam can be scanned. Due to the condition imposed on the permeability tensors (Eq. 5.8), the beam-former is in fact reflectionless for all beam scanning angles: a truly remarkable result. The beam-former can be implemented in much the same manner as the beam-shifting slab design described in Chapter 4. However, since the beam-former is not only anisotropic, but also inhomogeneous, each cell will have to be individually designed. Furthermore, the beam-former antenna will have multiple feeds (coaxial connectors) that are laterally displaced to demonstrate the devices scanning ability. The output boundary of the beam-former could be flared (as in a horn antenna) in order to launch the wave into free space. The flare will transition the guided wave supported by the tensor transmission-line unit cells to an unbounded wave in free space. This experimental beam-former would demonstrate the design approachs true technological value. The

device could be instrumental in the development of flat lenses for focal plane arrays.

Further attention can also be given to the improvement of device performance. A beam-former design can be optimized to use a minimum number of unit cells. Furthermore, an optimization process can be performed using the design parameters explained in Chapter 5 to enable its realization using only non-dispersive tensor transmission-line metamaterials presented in Chapter 3. This way, a wide-band beam-formers with scanning capabilities would be possible.

6.2.2 Controlling the Phase and Power Flow in 3D

In Chapter 5, a novel approach to controlling the phase progression and power flow of electromagnetic fields was proposed for 2D medium and TM polarized waves. Truly arbitrary control of electromagnetic fields would require a 3D formulation of the method for both TE and TM polarization. To allow this, the method could be extended to the general case of 3D propagation. This generalization will involve selecting a wave vector ($\vec{k}$) and Poynting ($\vec{S}$) in two arbitrary directions, and solving for the material parameters needed. The derivation will be more involved than the 2D case, since it will include both TM and TE polarizations. Both the constituent TE and TM wave will possess the same wave vector, but the Poynting vector and wave impedances will be a function of both polarizations. A reflectionless condition on material parameters for 2D TM waves, such as that presented in Appendix A, should also be studied for 3D, TE and TM waves. Such a formulation would allow control of electromagnetic fields in a 3D medium. The approach could then compete with or offer an alternative to the transformation electromagnetics design approach even in 3D. In order to realize practical devices using the 3D extension of the method, further attention should be devoted to the design, analysis and homogenization of 3D tensor metamaterials for both TE and TM polarizations. The 2D tensor transmission-line metamaterials presented in Chapter 2, and previous work on volumetric transmission-

line metamaterials [120, 121, 122] could serve as starting point for this.

6.3 Publications

This thesis work has resulted in 6 journal papers, 13 conference papers, 3 conference summaries and one patent. They are listed below:

Refereed Journal Publications

G. Gok and A. Grbic, "Tailoring the Phase and Power Flow of Electromagnetic Fields", *Physical Review Letters*, vol. 111, 233904, December 2013.

G. Gok and A. Grbic, "Alternative Material Parameters for Transformation Electromagnetics Designs", *IEEE Transactions on Microwave Theory and Techniques*, vol. 61, pp. 1414-1424, April 2013.

G. Gok and A. Grbic, "Printed Beam Shifting Slab Design with Tensor Transmission-line Metamaterials", *IEEE Transactions on Antennas and Propagation*, vol. 61, pp. 728-734, February 2013.

G. Gok and A. Grbic, "Homogenization of Tensor TL Metamaterials", *Metamaterials*, vol. 5, no 2-3, pp. 81-89, 2011.

G. Gok and A. Grbic, "Full-Wave Verification of Tensor Transmission-line Metamaterials", *IEEE Antennas and Wireless Propagation Letters*, vol. 9, pp. 48-51, February 2010.

G. Gok and A. Grbic, "Tensor Transmission-Line Metamaterials", *IEEE Transactions on Antennas and Propagation*, vol. 58, pp. 1559-1566, May 2010.

Refereed Conference Publications

G. Gok and A. Grbic, "A printed Antenna Beam Former Implemented Using Tensor Transmission-line Metamaterials", accepted for presentation at *IEEE International Symposium on Antennas and Propagation*, Memphis, TN, July 6-12, 2014.

A. Grbic and G. Gok, "Creating Field Profiles with Arbitrary Phase and Power Distributions", *Antennas and Propagation (EuCAP), 2014 Proceedings of the Eight*

European Conference, Hague, Netherlands, April 6-11, 2014 (invited).

G. Gok and A. Grbic, "Controlling Phase and Power Flow with Electromagnetic Metamaterials", *Fifth International Conference on Metamaterials, Photonics Crystals and Plasmonics (META 14)*, Singapore, May 20-23, 2014 (invited).

A. Grbic and G. Gok, "Transformation Electromagnetics Designs Without a Coordinate Transformation", *21st International Conference on Applied Electromagnetics and Communications*, Dubrovnik, Croatia, October 14-16, 2013.

G. Gok and A. Grbic, "Controlling the Phase and Power Flow of Electromagnetic Fields", *IEEE International Symposium on Antennas and Propagation*, Orlando, FL, July 7-13, 2013.

A. Grbic, G. Gok, M. F. Imani, A. M. Patel, C. Pfeiffer and M. Ettorre, "Metamaterial Surfaces for Near and Far-Field Applications", *Antennas and Propagation (EuCAP), 2013 Proceedings of the Seventh European Conference*, Gothenburg, Sweden, April 8-12 2013 (invited).

G. Gok and A. Grbic, "Alternative Material Parameters for Transformation Optics Designs", *6th International Conference on Advanced Electromagnetic Materials in Microwaves and Optics (Metamaterials 2012)*, St. Petersburg, Russia, Sept. 1722 2012 (invited).

G. Gok and A. Grbic, "A beam Shifting Slab Implemented with Printed, Tensor TL Metamaterials", *IEEE MTT-S International Microwave Symposium*, Montreal, Canada, June 17-22 2012.

G. Gok and A. Grbic, "Tensor Circuit Networks for Transformation Optics, *5th International Conference on Advanced Electromagnetic Materials in Microwaves and Optics (Metamaterials 2011)*, Barcelona Spain, Oct. 10-14 2011 (invited).

G. Gok and A. Grbic, "Tensor Transmission-Line Metamaterials and Their Applications," *Antennas and Propagation (EuCAP), 2011 Proceedings of the Fifth European Conference*, Rome, Italy, April 11-15 2011 (invited).

A. Grbic and G. Gok, "Transformation Circuits," *Antennas and Propagation (EuCAP), 2010 Proceedings of the Fourth European Conference*, Barcelona, Spain, April, 12-16 2010 (invited).

A. Grbic, G. Gok, S. M. Rudolph, "Advances in Planar and Volumetric Metamaterials", *2010 ICECom Conference Proceedings*, 20-23 Sept. 2010 (invited).

A. Grbic, G. Gok, "Tensor Metamaterials Based On Transmission-Line Networks", *4th International Conference on Advanced Electromagnetic Materials in Microwaves and Optics (Metamaterials 2010)*, Karlsruhe, Germany, Sept. 13-16 2010 (invited).

Conference Summaries

G. Gok and A. Grbic, "Tensor Transmission-Line Metamaterials", USNC/URSI National Radio Science Meeting, Toronto, ON, CA, July 11-17, 2010.

G. Gok and A. Grbic, "Tensor TL Metamaterials: Analysis and Design", USNC/URSI National Radio Science Meeting, Spokane, WA, July 3–8, 2011.

G. Gok and A. Grbic, "Experimental Verification of Tensor Transmission-line Metamaterials: A Printed Beam -Shifting Slab", USNC/URSI National Radio Science Meeting, Chicago, IL, July 8-13, 2012.

Patent

A. Grbic and G. Gok, "Tensor Transmission - Line Metamaterials", U.S. Patent No: US 8,490,035 B2, issued on July 2013.

APPENDICES

APPENDIX A

Matched Medium Condition

Based on the observation of transformation electromagnetics designs, a condition on the determinant of the permeability tensor was assumed in Eq. (5.8). This condition ensured that the transformed region remains impedance matched to its surrounding medium under all plane-wave illuminations [63]. Here, this condition is elaborated on. First, the condition on the permeability tensor of a transformation electromagnetic device is analyzed. Then, the same condition is derived by considering the reflectionless transmission between two homogenous, magnetically anisotropic media with a planar boundary (see Fig. A.1). In accordance with Chapter 5, a TM_z polarization is considered. So the relevant material parameters become a 2×2 permeability tensor and a permittivity scalar:

$$\bar{\bar{\mu}} = \begin{bmatrix} \mu_{xx} & \mu_{xy} \\ \mu_{yx} & \mu_{yy} \end{bmatrix} \qquad \epsilon = \epsilon_z. \tag{A.1}$$

First, let us analyze the condition on the permeability tensor of a transformation electromagnetics device. The transformed material parameters (permittivity and permeability) of a transformation electromagnetics design are given by well known formulae

[36]

$$\bar{\bar{\mu}}' = \frac{J\bar{\bar{\mu}}_o J^T}{|J|}, \qquad \bar{\bar{\epsilon}}' = \frac{J\bar{\bar{\epsilon}}_o J^T}{|J|},$$

where J is the Jacobian matrix of the coordinate transformation equation, and ($\bar{\bar{\epsilon}}_o$, $\bar{\bar{\mu}}_o$) are the permittivity and permeability of the background medium. Assuming the background medium is free space, the relevant material parameters (A.1) can be written explicitly in terms of the Jacobian matrix entries as

$$\bar{\bar{\mu}}' = \frac{1}{|J|}\begin{bmatrix} J_{xx}^2 + J_{xy}^2 & J_{xx}J_{yx} + J_{xy}J_{yy} \\ J_{xx}J_{yx} + J_{xy}J_{yy} & J_{yx}^2 + J_{yy}^2 \end{bmatrix} \tag{A.2a}$$

$$\epsilon_z = \frac{1}{|J|} \tag{A.2b}$$

where

$$|J| = J_{xx}J_{yy} - J_{xy}J_{yx}$$

is the determinant of the Jacobian matrix.

The determinant of $\bar{\bar{\mu}}$ in (A.2a) can be shown to be equal to the determinant of the background medium, $|\bar{\bar{\mu}}_o| = 1$, independent of the Jacobian matrix entries, i.e. coordinate transformation used. This condition is strictly related to the reflectionless (impedance matched) property of the transformation electromagnetic devices under all plane wave illumination as shown in [63].

To derive a similar condition, we analyze wave propagation at the interface of two magnetically anisotropic media. Fig. A.1 shows two magnetically anisotropic media that are seperated with a planar boundary normal to the x axis. The wave impedance normal to the interface, $\overline{\eta}_x$, and the wave number tangent to the interface, $\overline{k}_y$, must be common to both media in order to satisfy the impedance matching (reflectionless property) and Snell's Law.

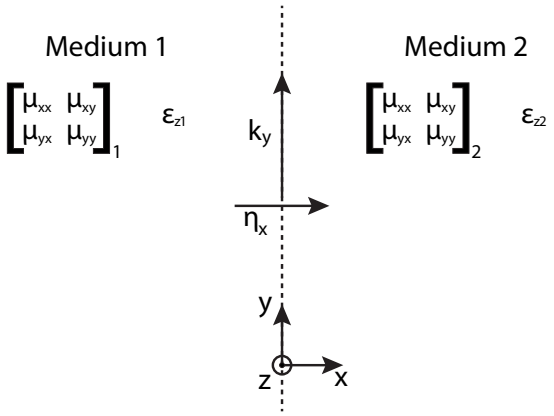

Figure A.1: Two magnetically anisotropic media are separated by a planar interface (dashed line) normal to the x axis. The plane wave propagation is restricted to $x-y$ plane and no variation of fields is assumed along the z direction.

The two quantities, $\overline{\eta}_x$ and $\overline{k}_y$, are related through the medium's material parameters. To find the relationship, we start by writing the dispersion equation of a medium with material parameters in (A.1):

$$\overline{k}_x^2 \frac{\mu_{xx}}{|\,\bar{\bar{\mu}}\,|} + 2\overline{k}_x\overline{k}_y \frac{\mu_{xy}}{|\,\bar{\bar{\mu}}\,|} + \overline{k}_y^2 \frac{\mu_{yy}}{|\,\bar{\bar{\mu}}\,|} = \epsilon_z. \tag{A.3}$$

Then, using equation (5.4), the normalized wave impedance, $\overline{\eta}_x$, can be written in terms of normalized wave numbers $(\overline{k}_x, \overline{k}_y)$ and permeability values:

$$\frac{1}{\overline{\eta}_x} = \overline{k}_x \frac{\mu_{xx}}{|\,\bar{\bar{\mu}}\,|} + \overline{k}_y \frac{\mu_{xy}}{|\,\bar{\bar{\mu}}\,|}. \tag{A.4}$$

Squaring both sides of equation (A.4) yields

$$\frac{1}{\overline{\eta}_x^2} = \overline{k}_x^2 \frac{\mu_{xx}^2}{|\,\bar{\bar{\mu}}\,|^2} + 2\overline{k}_x\overline{k}_y \frac{\mu_{xx}\mu_{xy}}{|\,\bar{\bar{\mu}}\,|^2} + \overline{k}_y^2 \frac{\mu_{xy}^2}{|\,\bar{\bar{\mu}}\,|^2}. \tag{A.5}$$

Multiplying both sides of the dispersion equation (A.3) by $\frac{\mu_{xx}}{|\bar{\bar{\mu}}|}$ yields

$$\overline{k}_x^2 \frac{\mu_{xx}^2}{|\,\bar{\bar{\mu}}\,|^2} + 2\overline{k}_x\overline{k}_y \frac{\mu_{xy}\mu_{xx}}{|\,\bar{\bar{\mu}}\,|^2} + \overline{k}_y^2 \frac{\mu_{yy}\mu_{xx}}{|\,\bar{\bar{\mu}}\,|^2} = \frac{\epsilon_z\mu_{xx}}{|\,\bar{\bar{\mu}}\,|}. \tag{A.6}$$

Equation (A.6) can be rearranged as

$$\overline{k}_x^2 \frac{\mu_{xx}^2}{|\,\bar{\bar{\mu}}\,|^2} + 2\overline{k}_x\overline{k}_y \frac{\mu_{xy}\mu_{xx}}{|\,\bar{\bar{\mu}}\,|^2} = \frac{\epsilon_z\mu_{xx}}{|\,\bar{\bar{\mu}}\,|} - \overline{k}_y^2 \frac{\mu_{yy}\mu_{xx}}{|\,\bar{\bar{\mu}}\,|^2}. \tag{A.7}$$

The left hand side of equation (A.7) can be substituted into (A.5) to obtain

$$\begin{aligned} \frac{1}{\overline{\eta}_x^2} &= \frac{\epsilon_z\mu_{xx}}{|\,\bar{\bar{\mu}}\,|} - \overline{k}_y^2 \frac{\mu_{yy}\mu_{xx}}{|\,\bar{\bar{\mu}}\,|^2} + \frac{\mu_{xy}^2\overline{k}_y^2}{|\,\bar{\bar{\mu}}\,|^2} \\ &= \frac{\epsilon_z\mu_{xx}}{|\,\bar{\bar{\mu}}\,|} - \frac{\overline{k}_y^2}{|\,\bar{\bar{\mu}}\,|}. \end{aligned} \tag{A.8}$$

Equation (A.8) can be rearranged to yield

$$\frac{(\frac{1}{\overline{\eta}_x})^2}{(\sqrt{\frac{\mu_{xx}\epsilon_z}{|\bar{\bar{\mu}}|}})^2} + \frac{(\overline{k}_y)^2}{(\sqrt{\mu_{xx}\epsilon_z})^2} = 1. \tag{A.9}$$

Equation (A.9) defines a curve for a magnetically anisotropic medium with material parameters given by (A.1). This curve can be used to find the necessary condition on medium 1 to be perfectly matched to medium 2 (see Fig. A.1). If perfect impedance matching between two media is desired, for all angle of incidence, the $\overline{k}_y$ vs. $\frac{1}{\overline{\eta}_x}$ curves for both medium must overlap. This ensures that for a given tangential wave number, $\overline{k}_y$, both media have the same wave impedance normal to the interface: $\overline{\eta}_x$. In short, the following relations must hold between the material parameters of media on either sides of the interface:

$$|\,\bar{\bar{\mu}}\,|_1 = |\,\bar{\bar{\mu}}\,|_2, \tag{A.10}$$

$$(\mu_{xx}\epsilon_z)_1 = (\mu_{xx}\epsilon_z)_2. \tag{A.11}$$

Equation (A.10) shows that the determinant of permeabilities must be same on both sides of the interface. Equation (A.11) is satisfied if the media are matched for a

single angle of incidence, while equation (A.10) ensures an impedance match for all angles.

APPENDIX B

Permittivity Optimization

The permittivity distribution in the transformation region was calculated assuming a linearly tapered wave impedance $\overline{\eta}_x$ from boundary 1 to boundary 2. The tapered impedance approach was used to impedance match the transformation region to the surrounding medium and reduce inter-cell reflections. Tapering the wave impedance $\overline{\eta}_x$ to find the permittivity profile was a suitable approach, since power flow was predominantly in the x direction for the examples considered. For cases where the direction of power flow varies substantially within the transformation region, the permittivity profile can be found by minimizing inter-cell reflections using a rigorous optimization method. In the optimization method, the wave impedances of each unit cell are written in terms of ϵ_z using Eq. (5.6). From these wave impedances, reflection coefficients Γ_x and Γ_y are defined between each unit cell and its neighbors in the x and y directions of power flow:

$$\Gamma_x = \frac{\overline{\eta}'_x - \overline{\eta}_x}{\overline{\eta}'_x + \overline{\eta}_x} \qquad\qquad \Gamma_y = \frac{\overline{\eta}'_y - \overline{\eta}_y}{\overline{\eta}'_y + \overline{\eta}_y}. \tag{B.1}$$

In (B.1), $\overline{\eta}_x$ and $\overline{\eta}_y$ are the normalized wave impedances of the unit cell under consideration, while $\overline{\eta}'_x$ and $\overline{\eta}'_y$ are those of the neighboring cells along the x and y directions

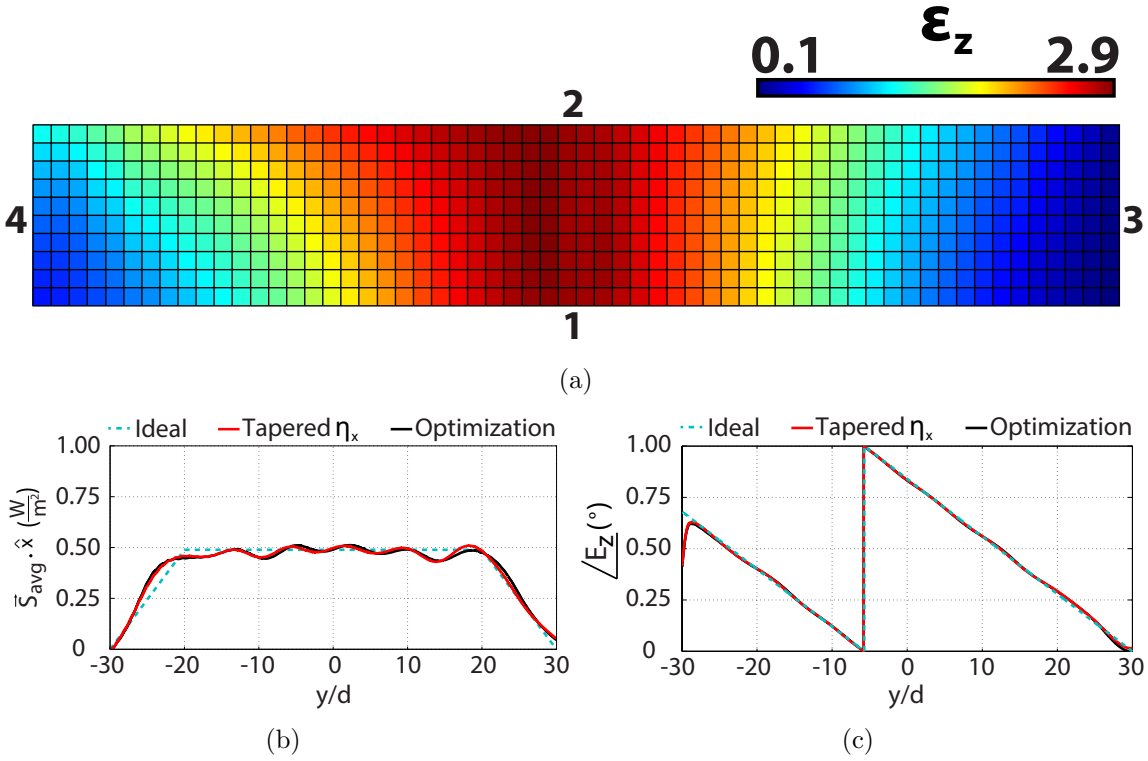

Figure B.1: (a) Optimized permittivity distribution. (b) Power density and (c) phase profiles along boundary 2 with permittivity distributions calculated through tapered wave impedance assumption and optimization method. Dashed lines denotes the ideal profiles.

of power flow. The optimum permittivity distribution is found by minimizing reflections between unit cells through an optimization process.

In the optimization, the wave impedances for each cell are calculated using Eq. (5.6) for an initial permittivity distribution. The reflection coefficients between neighboring unit cells are then found using (B.1). The reflection coefficients, Γ_x and Γ_y, are weighted by the $\cos\theta_s$ and $\sin\theta_s$ functions, respectively, to account for the direction of power flow. The squared magnitudes of all weighted reflection coefficients are then summed. Using an optimization algorithm such as a genetic algorithm (GA), the permittivity profile that minimizes this sum is found. It should be emphasized that only one parameter ϵ_z is optimized per unit cell. Therefore, the problem scales only linearly with the number of unit cells. Once the optimum permittivity of the unit

cells is found, the permeability tensor is calculated using equation (5.9).

The performance of transformation regions with permittivity profiles calculated using the tapered wave impedance approach and a GA optimization are compared. The example of the Section 5.3.2 (see Fig. 5.6) is considered. Fig. 5.5(b) and Fig. B1(a) show the permittivity profiles calculated using the tapered wave impedance approach and a GA optimization, respectively. Fig. B1(b) and Fig. B1(c) plot the power density and phase profiles at boundary 2 for the two cases. The output profiles show close agreement, verifying that the tapered wave impedance approach provides near optimal performance for the designs considered in Chapter 5.

APPENDIX C

Linear Power Density Mapping

In the first four examples of Chapter 5, linear power flow is assumed through the transformation region when mapping an input power density at boundary 1 to a desired output power density at boundary 2. The mapping allows the Poynting vector direction to be determined for each unit cell within the transformation region. Here, this mapping technique is described in detail.

First, the incident power density along boundary 1 is computed. From it, the time-averaged power (P_{ave}) through boundary 1 is found. The power P_{ave} is represented by N points/dots along boundary 1. Each point represents an amount of power equal to $P_{point} = P_{ave}/N$. These points are distributed amongst unit cells along boundary 1 according to the time-averaged power flow (P_{cell}) through the edge of each unit cell along boundary 1. Each P_{cell} is represented by $N_{cell} = P_{cell}/P_{point}$ points, where N_{cell} is rounded to closest integer value. The points corresponding to each unit cell are uniformly distributed along each cell edge. In this way, the N points are positioned along boundary 1 to represent the input power density profile. To ensure that the power through boundary 1 and 2 is the same, N points are also positioned along boundary 2. They are distributed according to the desired output power density profile. The points on boundary 1 are then paired with those on boundary 2 using

straight lines, starting with points closest to one of the side boundaries (boundaries 3 or 4). The lines connecting the paired points represent the direction of power flow within the transformation region. The direction of the Poynting vector $\vec{S}$ within each unit cell is given by the line closest to the center of each cell.

Now, the power flow for the example of Section 5.3.3 is revisited. In this example, a transformation region is designed that produces a triangular power density and uniform phase distribution along boundary 2 (see Fig. 5.8). The time-averaged power through boundary 1 is calculated to be $P_{ave} = 103.2\ mW/m$ for a $0.260\ mW/m$ cylindrical source. The power through boundary 1 is represented by $N = 7200$ points. Therefore, each point represents an amount of power equal to $P_{point} = 0.014\ mW/m$. Fig. C1(a) shows the time-averaged power through individual unit cells (P_{cell}) along boundary 1, and the representative number of points per cell (N_{cell}). 7200 points are also distributed along boundary 2 to represent the triangular output power density. Fig. C1(b) shows the time-averaged power through individual unit cells (P_{cell}) along boundary 2, and the representative number of points per cell (N_{cell}). Fig. C1(c) shows the distribution of points for a few unit cells along boundaries 1 and 2. The straight lines pairing the points on the two boundaries are also shown. The direction of the Poynting vector $\vec{S}$ within each unit cell is given by the line closest to the center of each cell.

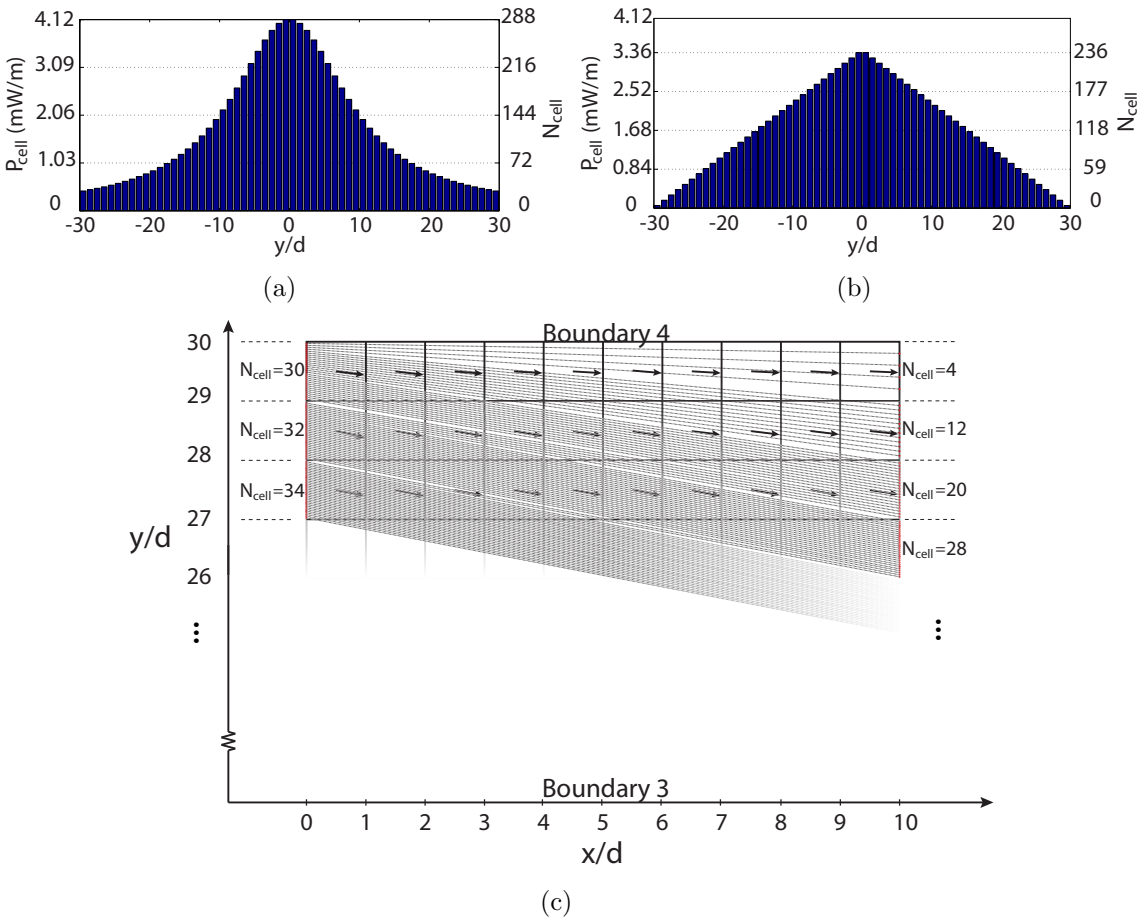

Figure C.1: (a) Time-averaged power through the unit cell edges along boundary 1, and the corresponding number of points per unit cell. (b) Time-averaged power through the unit cell edges along boundary 2 for a triangular power density, and the corresponding number of points per unit cell. (c) The distribution of points for a few cells along boundaries 1 and 2. The straight lines pairing the points on the two boundaries are also shown. The direction of the Poynting vector $\vec{S}$ within each unit cell is given by the line closest to the center of each cell..

BIBLIOGRAPHY

BIBLIOGRAPHY

[1] J. C. Maxwell, "A dynamical theory of the electromagnetic field," *Philosophical Transactions of the Royal Society of London*, vol. 155, pp. 459–512, 1865.

[2] W. E. Kock, "Metallic delay lenses," *Bell System Technical Journal*, vol. 27, pp. 58–83, January 1948.

[3] J. Brown, "Artificial dielectrics having refractive indices less than unity," *Proceedings of the IEEE*, vol. 100, no. 5, pp. 51–62, October 1953.

[4] J. B. Pendry, A. J. Holden, W. J. Stewart, and I. Youngs, "Extremely low frequency plasmons in metallic mesostructures," *Physical Review Letters*, vol. 76, no. 25, pp. 4773–4776, June 1996.

[5] J. B. Pendry, A. J. Holden, D. J. Robbins, and W. J. Stewart, "Magnetism from conductors and enhanced nonlinear phenomena," *IEEE Transactions on Microwave Theory and Techniques*, vol. 47, pp. 2075–2084, November 1999.

[6] D. R. Smith, W. J. Padilla, D. C. Vier, S. C. Nemat-Nasser, and S. Schultz, "Composite medium with simultaneously negative permeability and permittivity," *Physical Review Letters*, vol. 84, no. 18, pp. 4184–4187, May 2000.

[7] R. A. Shelby, D. R. Smith, and S. Schultz, "Experimental verification of a negative index of refraction," *Science*, vol. 292, pp. 77–79, April 2001.

[8] A. Grbic and G. V. Eleftheriades, "Overcoming the diffraction limit with a planar left-handed transmission-line lens," *Physical Review Letters*, vol. 92, pp. 117403, March 2004.

[9] N. Fang, H. Lee, S. Cheng, and X. Zhang, "Subdiffraction-limited optical imaging with a silver superlens," *Science*, vol. 308, no. 5721, pp. 534–537, 2005.

[10] A. Grbic and G. V. Eleftheriades, "Experimental verification of backward-wave radiation from a negative refractive index metamaterial," *Journal of Applied Physics*, vol. 92, no. 10, pp. 5930–5935, November 2002.

[11] S. Xi, H. Chen, T. Jiang, L. Ran, J. Huangfu, B. I. Wu, J. A. Kong, and M. Chen, "Experimental verification of reversed cherenkov radiation in left-handed metamaterial," *Physical Review Letters*, vol. 103, no. 19, pp. 194801, November 2009.

[12] J. B. Pendry, "Negative refraction makes a perfect lens," *Physical Review Letters*, vol. 85, pp. 3966–3969, October 2000.

[13] A. K. Iyer and G. V. Eleftheriades, "Negative refractive index metamaterials supporting 2-D waves," in *IEEE International Microwave Symposium*, Seattle, WA, June 2-7 2002, vol. 2, pp. 1067–1070.

[14] A. Grbic and G. V. Eleftheriades, "A backward-wave antenna based on negative refractive index L-C networks," in *IEEE Antennas and Propagation Society International Symposium*, San Antonio, TX, June 2002, vol. 4, pp. 340–343.

[15] C. Caloz and T. Itoh, "Application of the transmission line theory of left-handed (LH) materials to the realization of a microstrip LH line," in *IEEE Antennas and Propagation Society International Symposium*, San Antonio, TX, June 2002, vol. 2, pp. 412–415.

[16] A. A. Oliner, "A periodic-structure negative-refractive-index medium without resonant elements," in *USNC/URSI Radio Science Meeting*, San Antonio, TX, June 16-21 2002.

[17] G. V. Eleftheriades, A. K. Iyer, and P. C. Kremer, "Planar negative refractive index media using periodically L-C loaded transmission lines," *IEEE Transactions on Microwave Theory and Techniques*, vol. 50, no. 12, pp. 2702–2712, December 2002.

[18] A. Grbic and G. V. Eleftheriades, "Periodic analysis of a 2-D negative refractive index transmission line structure," *IEEE Transactions on Antennas and Propagation*, vol. 51, pp. 2604–2611, October 2003.

[19] A. Grbic and G. V. Eleftheriades, "Negative refraction, growing evanescent waves, and sub-diffraction imaging in loaded transmission-line metamaterials," *IEEE Transactions on Microwave Theory and Techniques*, vol. 51, pp. 2297–2305, December 2003.

[20] G. V. Eleftheriades and O. F. Siddiqui, "Negative refraction and focusing in hyperbolic transmission-line periodic grids," *IEEE Transactions on Microwave Theory and Techniques*, vol. 53, no. 1, pp. 396–403, January 2005.

[21] K. G. Balmain, A. A. E. Luttgen, and P. C. Kremer, "Power flow for resonance cone phenomena in planar anisotropic metamaterials," *IEEE Transactions on Antennas and Propagation*, vol. 51, no. 10, pp. 2612–2618, October 2003.

[22] J. K. H. Wong, K. G. Balmain, and G. V. Eleftheriades, "Fields in planar anisotropic transmission-line metamaterials," *IEEE Transactions on Antennas and Propagation*, vol. 54, no. 10, pp. 2742–2749, October 2006.

[23] C. Caloz and T. Itoh, "Positive/negative refractive index anisotropic 2-D metamaterials," *IEEE MIcrowave and Wireless Components Letters*, vol. 13, no. 12, pp. 547–549, December 2003.

[24] C. Caloz, C.-H. Ahn, and T. Itoh, "Analysis 2D finite-size metamaterials by the transmission matrix method," in *IEEE Antennas and Propagation Society International Symposium*, Washington, DC, July 2005, vol. 3B, pp. 2–5.

[25] G. V. Eleftheriades, M. A. Antoniades, and F. Qureshi, "Antenna applications of negative-refractive-index transmission-line structures," *Journal of Applied Physics*, vol. 1, no. 1, pp. 12–22, February 2007.

[26] R. W. Ziolkowski, P. Jin, and C. C. Lin, "Metamaterial-inspired engineering of antennas," *Proceedings of the IEEE*, vol. 99, no. 10, pp. 1720–1731, October 2011.

[27] C. Caloz and T. Itoh, *Electromagnetic metamaterials: transmission line theory and microwave applications*, Wiley-IEEE Press, New York, 2005.

[28] J. Ng, H. Chen, and C. T. Chan, "Metamaterial frequency-selective superabsorber," *Optics Letters*, vol. 34, no. 5, pp. 644–646, March 2009.

[29] C. M. Watts, X. Liu, and W. J. Padilla, "Metamaterial electromagnetic wave absorbers," *Advanced Materials*, vol. 24, no. 23, pp. OP98–OP120, June 2012.

[30] C. L. Holloway, E. F. Kuester, J. A. Gordon, J. O'Hara, J. Booth, and D. R. Smith, "An overview of the theory and applications of metasurfaces: the two-dimensional equivalents of metamaterials," *IEEE Antennas and Propagation Magazine*, vol. 54, no. 2, pp. 10–35, April 2012.

[31] N. Yu and F. Capasso, "Flat optics with designer metasurfaces," *Nature Materials*, vol. 13, no. 2, pp. 139150, January 2014.

[32] A. V. Kildishev, A. Boltasseva, and V. M. Shalaev, "Planar photonics with metasurfaces," *Science*, vol. 339, no. 6125, March 2013.

[33] R. V. Craster and S. Guenneau, *Acoustic metamaterials*, Springer, 2013.

[34] M. Kadic, T. Buckmann, R. Schittny, and M. Wegener, "Metamaterials beyond electromagnetism ," *Reports on Progress in Physics*, vol. 76, pp. 126501, November 2013.

[35] M. Maldovan, "Sound and heat revolutions in phononics," *Nature*, vol. 9, pp. 209–217, November 2013.

[36] J. B. Pendry, D. Schurig, and D.R. Smith, "Controlling electromagnetic fields," *Science*, vol. 312, pp. 1780–1782, June 2006.

[37] D. Schurig, J. J. Mock, B. J. Justice, S. A. Cummer, J. B. Pendry, A. F. Starr, and D. R. Smith, "Metamaterial electromagnetic cloak at microwave frequencies," *Science*, vol. 314, pp. 977–980, November 2006.

[38] M. Rahm, D. Schurig, D. A. Roberts, S. A. Cummer, and D. R. Smith adn J. B. Pendry, "Design of electromagnetic cloaks and concentrators using form-invariant coordinate transformations of Maxwell's equations," *Photonics and Nanostructures - Fundamentals and Applications*, vol. 6, no. 1, pp. 87–95, August 2007.

[39] D.-H. Kwon and D. H. Werner, "Transformation optical designs for wave collimators, flat lenses and right-angle bends," *New Journal of Physics*, vol. 10, no. 11, pp. 115023, May 2008.

[40] D.-H. Kwon and D. H. Werner, "Flat focusing lens designs having minimized reflection based on coordinatetransformation techniques," *Optics Express*, vol. 17, no. 10, pp. 7807–7817, May 2009.

[41] H. Chen and C. T. Chan, "Transformation media that rotate electromagnetic fields," *Applied Physics Letters*, vol. 90, pp. 241105, June 2007.

[42] D.-H. Kwon and D. Werner, "Polarization splitter and polarization rotator designs based on transformation optics," *Optics Express*, vol. 16, no. 23, pp. 18731–18737, November 2008.

[43] M. Rahm, D. A. Roberts, J. B. Pendry, and D. R. Smith, "Transformation-optical design of adaptive beam bends and beam expanders," *Optics Express*, vol. 16, no. 15, pp. 11555–11567, July 2008.

[44] Z. L. Mei and T. J. Cui, "Experimental realization of a broadband bend structure using gradient index metamaterials," *Optics Express*, vol. 17, no. 20, pp. 18354–18363, September 2009.

[45] P.-H. Tichit, S.N. Burokur, and A. de Lustrac, "Ultradirective antenna via transformation optics," *Journal of Applied Physics*, vol. 105, pp. 104912, May 2009.

[46] F. Kong, B.-I. Wu, J. A. Kong, J. Huangfu, S. Xi, and H. Chen, "Planar focusing antenna design by usign coordinate transformation technology," *Applied Physics Letters*, vol. 91, pp. 253509, December 2007.

[47] Y. Luo, J. Zhang, H. Chen, J. Huangfu, and R. Lixin, "High-directivity antenna with small antenna aperture," *Applied Physics Letters*, vol. 95, no. 19, pp. 193506, December 2009.

[48] A. V. Kildishev and E. E. Narimanov, "Impedance-matched hyperlens," *Optics Letters*, vol. 23, no. 23, pp. 3432–3434, December 2007.

[49] Y. Lai, J. Ng, H. Chen, D. Han, J. Xiao, Z.-Q. Zhang, and C. T. Chan, "Illusion optics: the optical transformation of an object into another object," *Physical Review Letters*, vol. 102, no. 25, pp. 253902, June 2009.

[50] U. Leonhardt, "Optical conformal mapping," *Science*, vol. 312, pp. 1777–1780, June 2006.

[51] U. Leonhardt and T. G. Philbin, "Transformation optics and geometry of light," *Progress in Optics*, vol. 53, pp. 69–152, 2009.

[52] H. Chen, C. T. Chan, and P. Sheng, "Transformation optics and metamaterials," *Nature Materials*, vol. 9, pp. 387–396, May 2010.

[53] D.-H. Kwon and D. H. Werner, "Transformation electromagnetics: an overview of the theory and applications," *IEEE Antennas and Propagation Magazine*, vol. 52, no. 1, pp. 24–46, 2010.

[54] N. B. Kundtz, D. R. Smith, and J. B. Pendry, "Electromagnetic design with transformation optics," *Proceedings of the IEEE*, vol. 99, no. 10, pp. 1622–1633, 2011.

[55] D. H. Werner and D.-H. Kwon, *Transformation electromagnetics and metamaterials*, Springer, 2014.

[56] Z. H. Jiang P. L. Werner J. P. Turpin, A. T. Massoud and D. H. Werner, "Conformal mappings to achieve simple material parameters for transformation optics devices," *Optics Express*, vol. 18, no. 1, pp. 244–252, November 2010.

[57] J. Li and J. B. Pendry, "Hiding under carpet: a new strategy for cloaking," *Physical Review Letters*, vol. 101, no. 20, pp. 203901, November 2008.

[58] G. Gok and A. Grbic, "Tensor transmission-line metamaterials," *IEEE Transactions on Antennas and Propagation*, vol. 58, pp. 1559–1566, May 2010.

[59] G. Gok and A. Grbic, "Full-wave verification of tensor tl metamaterials," *IEEE Antennas and Wireless Propagation Letters*, vol. 9, pp. 48–51, Feb. 2010.

[60] G. Gok and A. Grbic, "Homogenization of tensor tl metamaterials," *Metamaterials*, vol. 5, no. 2-3, pp. 81–89, 2011.

[61] G. Gok and A. Grbic, "A printed beam-shifting slab designed using tensor transmission-line metamaterials," *IEEE Transactions on Antennas and Propagation*, vol. 61, no. 2, pp. 728–734, February 2013.

[62] G. Gok and A. Grbic, "Tailoring the phase and power flow of electromagnetic fields ," *Physical Review Letters*, vol. 111, pp. 233904, December 2013.

[63] G. Gok and A. Grbic, "Alternative material parameters for transformation electromagnetics designs," *IEEE Transactions on Microwave Theory and Techniques*, vol. 61, no. 4, pp. 1414–1424, April 2013.

[64] A. Grbic and G. Gok, "Transformation circuits," in *Proceedings of the Fourth European Conference on Antennas and Propagation (EuCAP)*, Barcelona, Spain, April 2010, pp. 1–4.

[65] A. Grbic, "Super resolving negative-refractive-index transmission-line lenses," *PhD Thesis, The Edward S. Rogers Sr. Department of Electrical and Computer Engineering, University of Toronto*, 2005.

[66] G.V. Eleftheriades and K.G. Balmain, Eds., *Negative refraction metamaterials*, John Wiley and Sons, Toronto, 1st edition, 2005.

[67] C. R. Brewitt-Taylor and P. B. Johns, "On the construction and numerical solution of transmission-line and lumped network models of Maxwells' equations," *Intern. Journal for Numerical Methods in Engineering*, vol. 15, pp. 13–30, October 1980.

[68] C. Christopoulos, *The Transmission-line modeling method TLM*, IEEE Press, Piscataway,NJ, 1995.

[69] G. Gok and A. Grbic, "Tensor transmission-line metamaterials and their applications," in *Proceedings of Fifth European Conference on Antennas and Propagation (EuCAP)*, Rome, Italy, Apr. 2011, pp. 3313 –3315.

[70] H. Chen and C. T. Chan, "Transformation media that rotate electromagnetic fields," *Applied Physics Letters*, vol. 90, pp. 241105, June 2007.

[71] N. Engheta, A. Salandrino, and A. Alu, "Circuit elements at optical frequencies: nanoinductors, nanocapacitors, and nanoresistors," *Physical Review Letters*, vol. 95, pp. 095504, August 2005.

[72] D. M. Pozar, *Microwave Engineering*, John Wiley and Sons Inc, 3rd edition, 2005.

[73] E. Gandini, M. Ettorre, R. Sauleau, and A. Grbic, "A lumped-element unit cell for beam-forming networks and its application to a miniaturized butler matrix," *IEEE Transactions on Microwave Theory and Techniques*, vol. 61, no. 4, pp. 1477–1487, April 2013.

[74] G. Liu, C. Li, C. Chen, Z. Lu, and G. Fang, "Experimental verification of field rotating with invisibility by full tensor transmission-line metamaterials," *Applied Physics Letters*, vol. 101, no. 22, pp. 224105, November 2012.

[75] G. Liu, C. Li, C. Zhang, Z. Sun, and G. Fang, "Experimental verification of field concentrator by full tensor transmission-line metamaterials," *Physical Review B*, vol. 87, no. 15, pp. 155125, April 2013.

[76] M. Selvanayagam and G. V. Eleftheriades, "Transmission-line metamaterials on a skewed lattice for transformation electromagnetics," *IEEE Transactions on Microwave Theory and Techniques*, vol. 59, no. 12, pp. 3272–3282, December 2011.

[77] D. -H. Kwon and C. D. Emiroglu, "Non-orthogonal grids in two-dimensional transmission-line metamaterials," *IEEE Transactions on Antennas and Propagation*, vol. 60, no. 9, pp. 4210–4218, September 2012.

[78] T. Nagayama and A. Sanada, "Physical equivalent circuit model for 2d full-tensor anisotropic metamaterials," in *Microwave Symposium Digest (IMS), 2013 IEEE MTT-S International*, June 2013, pp. 1–3.

[79] B. Kuprel and A. Grbic, "Anisotropic inhomogeneous metamaterials using nonuniform transmission-line grids aligned with the principal axes," *IEEE Antennas and Wireless Propagation Letters*, vol. 11, pp. 358–361, 2012.

[80] D. R. Smith, S. Schultz, P. Markos, and C.M. Soukoulis, "Determination of effective permittivity and permeability of metamaterials from reflection and transmission coefficients," *Physical Review B*, vol. 65, no. 19, pp. 195104, April 2002.

[81] X. Chen, T. M. Grzegorzyk, B. -I. Wu, J. Pacheco, Jr., and J. A. Kong, "Robust method to retrieve the constitutive effective parameters of metamaterials," *Physical Review E*, vol. 70, no. 1, pp. 016608, July 2004.

[82] D. R. Smith, D. C. Vier, Th. Koschny, and C. M. Soukoulis, "Electromagnetic parameter retrieval from inhomogeneous metamaterials," *Physical Review E*, vol. 71, no. 3, pp. 036617, March 2005.

[83] R. Liu, T.J. Cui, D. Huang, B. Zhao, and D.R. Smith, "Description and explanation of electromagnetic behaviors in artificial metamaterials based on effective medium theory," *Physical Review E*, vol. 76, pp. 026606, August 2007.

[84] C. R. Simovski, "Analytical modeling of double-negative composites," *Metamaterials*, vol. 2, pp. 169–185, September 2008.

[85] D. R. Smith, "Analytical expressions for the constitutive parameters of magnetoelectric metamaterials," *Physical Review E*, vol. 81, pp. 036605, March 2010.

[86] S. Kim, E. F. Kuester, C. L. Holloway, A. D. Scher, and J. Baker - Jarvis, "Boundary effects on the determination of metamaterial parameters from normal incidence reflection and transmission measurements," *IEEE Transactions on Antennas and Propagation*, vol. 59, no. 6, pp. 2226–2240, June 2011.

[87] D. R. Smith and J. B. Pendry, "Homogenization of metamaterials by field averaging (invited paper)," *Journal of Optical Society of America B*, vol. 23, no. 3, pp. 391–403, March 2006.

[88] M.G. Silveirinha, "Metamaterial homogenization approach with application to the characterization of microstructured composites with negative parameters," *Physical Review B*, vol. 75, pp. 115104, March 2007.

[89] C. Fietz and G. Shvets, "Current-driven metamaterial homogenization," *Physica B: Condensed Matter*, vol. 405, no. 14, pp. 2930 – 2934, July 2010.

[90] M. Zedler and G. V. Eleftheriades, "Spatial harmonics and homogenization of negative-refractive-index transmission-line structures," *IEEE Transactions on Microwave Theory and Techniques*, vol. 58, no. 6, pp. 1521–1531, June 2010.

[91] A. B. Yakovlev, M. G. Silveirinha, O. Luukkonen, C. R. Simovski, I. S. Nefedov, and S. A. Tretyakov, "Characterization of surface-wave and leaky-wave propagation on wire-medium slabs and mushroom structures based on local and nonlocal homogenization models," *IEEE Transactions on Microwave Theory and Techniques*, vol. 57, no. 11, pp. 2700–2714, November 2009.

[92] M. Y. Wang, J. J. Zhang, H. Chen, Y. Luo, S. Xi, L.X. Ran, and J. A. Kong, "Design and application of a beam shifter by transformation media," *Progress in Electromagnetics Research*, vol. PIER 83, pp. 147–155, 2008.

[93] M. Rahm, S. A. Cummer, D. Schurig, J. B. Pendry, and D. R. Smith, "Optical design of reflectionless complex media by finite embedded coordinate transformations," *Physical Review Letters*, vol. 100, pp. 063903, February 2008.

[94] I. Gallina, G. Castaldi, V. Galdi, A. Alu, and N. Engheta, "General class of metamaterial transformation slabs," *Physical Review B*, vol. 81, pp. 125124, March 2010.

[95] C. D. Emiroglu and D.-H. Kwon, "Transmission-line metamaterial design of an embedded-recessed line source," in *"Proceedings of IEEE Antennas and Propagation Society International Symposium"*, Spokane, WA, July 2011, pp. 2882 –2885.

[96] H. Chen, "Transformation optics in orthogonal coordinates," *Journal of Optics A: Pure and applied optics*, vol. 11, pp. 075102, April 2009.

[97] G. X. Yu, W. X. Jiang, and T. J. Cui, "Invisible slab cloaks via embedded optical transformation," *Applied Physics Letters*, vol. 94, no. 4, pp. 041904, 2009.

[98] A. Yariv and P. Yeh, *Optical Waves in Crystals*, John Wiley and Sons, 1984.

[99] J. A. Kong, *Electromagnetic wave theory*, EMW Publishing, Cambridge, MA, 1998.

[100] M. Yan, Z. Ruan, and M. Qiu, "Scattering characteristics of simplified cylindrical invisibility cloaks," *Optics Express*, vol. 15, no. 26, pp. 17772–17782, December 2007.

[101] D. A. Roberts S. A. Cummer D. R. Smith J. B. Pendry M. Rahm, D. Schurig, "Design of electromagnetic cloaks and concentrators using form-invariant coordinate transformations of Maxwells equations," *Photonics and Nanostructures*, vol. 6, pp. 87–95, April 2008.

[102] P. Hariharan, *Optical holography: principles, techniques and applications*, Cambridge University Press, 1996.

[103] P. Checcacci, V. Russo, and A. Scheggi, "Holographic antennas," *IEEE Transactions on Antennas and Propagation*, vol. 18, no. 6, pp. 811–813, November 1970.

[104] D. Sievenpiper, J. Colburn, B. Fong, J. Ottusch, and J. Visher, "Holographic artificial impedance surfaces for conformal antennas," in *Proceedings of IEEE Antennas and Propagation Society International Symposium (APSURSI)*, Washington, DC, July 2005, pp. 256–259.

[105] B. H. Fong, J. S. Colburn, J. J. Ottusch, J. L. Visher, and D. F. Sievenpiper, "Scalar and tensor holographic artificial impedance surfaces," *IEEE Trans. Antennas Propag.*, vol. 58, no. 10, pp. 3212–3221, October 2010.

[106] M. Yang, J. Li, and K. J. Webb, "Functional waveguide mode transformers," *IEEE Trans. Microwave Theory Tech.*, vol. 52, no. 1, pp. 161–169, January 2004.

[107] S. A. Schelkunoff, "A mathematical theory of linear arrays," *Bell System Technical Journal*, vol. 22, pp. 80–107, January 1943.

[108] M. V. Berry and N. L. Balazs, "Nonspreading wave packets," *American Journal of Physics*, vol. 47, no. 3, pp. 264–267, March 1979.

[109] G. A. Siviloglou and D. N. Christodoulides, "Accelerating finite energy Airy Beams," *Optics letters*, vol. 32, no. 8, pp. 979–981, April 2007.

[110] G. A. Siviloglou, J. Broky, A. Dogariu, and D. N. Christodoulides, "Observation of accelerating airy beams," *Physical Review Letters*, vol. 99, pp. 213901, November 2007.

[111] Y. Hu, G. A. Siviloglou, P. Zhang, N. K. Efremidis, D. N. Christodoulides, and Z. Chen, "Self-accelerating airy beams: generation, control, and applications," in *Nonlinear Photonics and Novel Optical Phenomena*, Z. Chen and R. Morandotti, Eds. Springer, New York, 2012.

[112] J. Durnin, "Exact solutions for nondiffracting beams. I. The scalar theory," *Journal of Optical Society America A*, vol. 4, no. 4, pp. 651–654, April 1987.

[113] J. Durnin, J. J. Miceli, and J. H. Eberly, "Diffraction-free beams," *Physical Review Letters*, vol. 58, pp. 1499–1501, April 1987.

[114] D. McGloin and K. Dholakia, "Bessel beams: diffraction in a new light," *Contemporary Physics*, vol. 46, no. 15, pp. 15–28, April 2005.

[115] M. Ettore, S. M. Rudolph, and A. Grbic, "Generation of propagating bessel beams using leaky-wave modes: experimental validation," *IEEE Transactions on Antennas and Propagation*, vol. 60, no. 6, pp. 2645–2653, June 2012.

[116] E. Ozbay, "Plasmonics: merging photonics and electronics at nanoscale dimensions," *Science*, vol. 311, no. 5758, pp. 189–193, January 2006.

[117] D. K. Gramotnev and S. I. Bozhevolnyi, "Plasmonics beyond the diffraction limit," *Nature Photonics*, vol. 4, pp. 83–91, January 2010.

[118] T. Zentgraf, Y . Liu, M. H. Mikkelsen, J. Valentine, and X. Zhang, "Plasmonic luneburg and eaton lenses," *Nature Nanotechnology*, vol. 6, pp. 151155, January 2011.

[119] P. Moitra, Y. Yang, Z. Anderson, I. I. Kravchenko, D. P. Briggs, and J. Valentine, "Realization of an all-dielectric zero-index optical metamaterial," *Nature Photonics*, vol. 7, pp. 1749–4885, August 2013.

[120] A. Grbic and G. V. Eleftheriades, "An isotropic three-dimensional negative-refractive-index transmission-line metamaterial," *Journal of Applied Physics*, vol. 98, no. 4, pp. 043106, August 2005.

[121] A. K. Iyer and G. V. Eleftheriades, "Volumetric layered transmission-line metamaterial exhibiting a negative refractive index," *Journal of Optical Society America B*, vol. 23, no. 3, pp. 553–570, March 2006.

[122] S. M. Rudolph and A. Grbic, "The Design of Broadband, Volumetric NRI Media Using Multiconductor Transmission-Line Analysis," *IEEE Transactions on Antennas and Propagation*, vol. 58, no. 4, pp. 1144–1154, April 2010.